Study of Nanoscale Phonon Dynamics using Ultrafast Coherent Extreme Ultraviolet Beams

by

Qing Li

B.S., University of Science and Technology of China, 2005

M.S., University of Colorado at Boulder, 2009

A thesis submitted to the

Faculty of the Graduate School of the

University of Colorado in partial fulfillment

of the requirements for the degree of

Doctor of Philosophy

Department of Physics

2011

This thesis entitled:
Study of Nanoscale Phonon Dynamics using Ultrafast Coherent Extreme Ultraviolet Beams
written by Qing Li
has been approved for the Department of Physics

Prof. Margaret M. Murnane

Prof. Henry C. Kapteyn

Date

The final copy of this thesis has been examined by the signatories, and we find that both the content and the form meet acceptable presentation standards of scholarly work in the above mentioned discipline.

Li, Qing (Ph.D., Physics)

Study of Nanoscale Phonon Dynamics using Ultrafast Coherent Extreme Ultraviolet Beams

Thesis directed by Prof. Henry C. Kapteyn and Prof. Margaret M. Murnane

Phonon transport is essential in both understanding and characterizing materials, particularly in nanoscale systems. In this thesis, I use coherent ultrafast extreme ultraviolet (EUV) beams from high-order harmonic generation, to study the dynamics of photoacoustics and energy-carrying phonons at the nanoscale.

I first generate and detect short-wavelength photoacoustic waves by impulsively heating sub-optical phononic crystals with an infrared laser. By monitoring the diffraction dynamics of EUV beams I observe the shortest-wavelength surface acoustic waves to date at 35 nm, corresponding to an interface layer sensitivity of sub-10 nm. I also achieve coherent control of SAW generation and preferentially enhance higher-order SAWs which allows us to reduce the generated SAW wavelength by a factor of two for a defined nanostructure period. I apply this photoacoustic technique to thin film metrology metrology: by generating nanoscale longitudinal and surface acoustic waves simultaneously, I am able to characterize the mechanical properties of ultrathin film samples.

Secondly, I study thermal transport dynamics in nano-to-bulk systems where phonons are heat carriers. I first observed quasi-ballistic thermal transport in 1D nano-to-bulk systems, and detect a stronger ballistic effect in 2D nanostructured materials. Temperature- and polarization-dependent experiments are also reported in this thesis. Furthermore, I was able to make a first attempt in dynamic thermal imaging using coherent diffraction of EUV beams.

Dedication

To Quan.

Acknowledgements

There are many extraordinary friends and colleagues helped me during my PhD time. I would like to recognize them here briefly.

I appreciate the great research and communication environment in JILA and CU, and want to thank many people relates directly and indirectly in my research works. Part of the list is here: Margaret Murnane and Henry Kapteyn, my gorgeous advisors, from whom I learned not only how to do physics research but also many other valuable experiences; Dr. Mark Siemens, who is the senior student I worked with when I first joined the group, is an excellent mentor; Kathy Hoogeboom-Pot, who is a young but prudent girl, helped me a lot in experiment, data analysis and in particular, edit my poor write-ups; Dr. Damiano Nardi, joined our group recently, but help me a lot on editing and also in inspiring discussions; and also Dr. Ronggui Yang, our collaborating professor of nano-thermal project, Professor Keith Nelson, and Chan La-O-Vorakiat, Adra Tory Carr, Ra'anan Tobey, Xiaobo Li, Matt Seaberg, Tenio Popmintchev, Dan Adams, Piotr Matyba, Craig Hogle, Luis Miaja-Avila, Jing Yin, Daisy Raymondson, Richard Sandberg, Ethan Townsend, Paul Arpin, Emrah Turgut, Xibin Zhou, Xiaoshi Zhang, Stefan Mathias, Ariel Paul, Amy Lytle and many more!

I also would like to thank my family. My parents hardly read English and probably can not understand much of this thesis, but their love and support are essential for me to pursuing my PhD degree and study abroad. Finally I want to thank my husband Quan Zhang for his love, understanding and support throughout the last 10 years.

Contents

Chapter

Tables

Table

Figures

Figure

Chapter 1

Introduction

The last few decades have witnessed enormous developments in nanofabrication technology and nano science, driven by the great demands of nano materials. For example, following continued Moore's law scaling down 30% in the characteristic size of electronics every two years, commercial integrated circuits are currently available with transistors of smallest lateral feature size $\sim$ 22nm. Thus knowledge of the electrical, optical, thermal and mechanical properties of silicon and other materials at this scale is essential to the semiconductor industry. Similarly, micron and sub-micron thin films are important due to their ability to enhance resistance to corrosion, modify optical properties, and prevent thermal breakdown; also periodic nano-patterned structures build the foundation of the next generation data storage technology. Many breakthroughs in fundamental science and technology are reported on nanoscale materials including observation of discrepancies in material properties as the size shrinks from bulk to nanoscale [11, 12], making the study of nano systems more urgent.

On the other hand, the rapid development of nano science allows for novel materials that do not exist in nature and have outstanding properties in all aspects. For example, nanometer multilayer structures are used in many optics to improve reflectivity; carbon nanotubes have high thermal conductivity and high stiffness; quantum dots and graphene exhibit brand new characteristics, and so on.

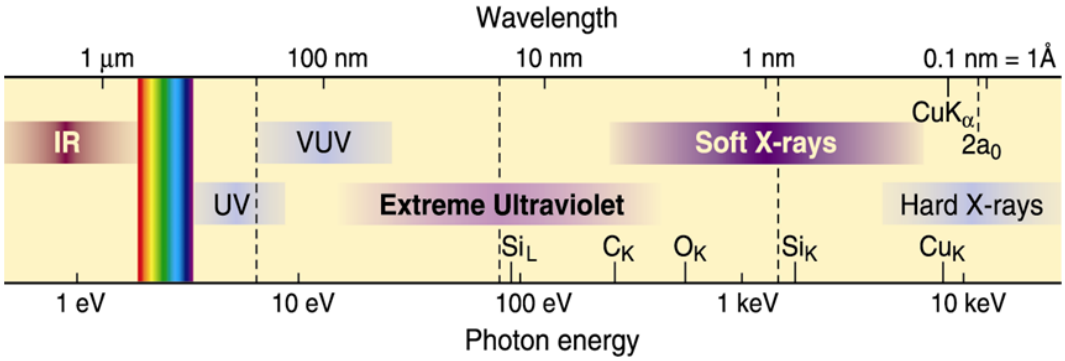

Figure 1.1: Electromagnetic spectrum covers from microwave to hard x-rays. High harmonic generation can generate coherent extreme ultraviolet and soft x-ray beams[1, 2]. Figure from ref [3].

1.1 Ultrafast Dynamics in Nanosystems

In nanoscience, dynamic measurements in the time domain with great time resolution become very important for two reasons. First, as the size shrinks to the nanoscale, the response time of many dynamic processes also decreases; for example, microelectronic devices are pushing to clock frequency of tens of gigahertz, and mesoscopic thermal transport in nanosystems occurs on picosecond time scales. Second, many ultrafast dynamics become more significant for nano materials than macroscopic systems, such as molecular vibration, phonon-electron interaction, and ballistic phonon transport.

Many fundamental research projects have been launched to understand the behavior of nano materials in ultrashort time scale. However, the requirement of both high spatial and temporal resolution becomes a significant challenge for many approaches.

Pioneering work from our group in high harmonic generation (HHG) promises to provide a unique tool to probe nanometer size scale with femtosecond time resolution. It accomplishes this by generating coherent ultrafast extreme ultraviolet (EUV) and soft x-ray beams, with wavelengths down to a few nanometers [13, 2] (see Fig. 1.1).

1.2 Phonon Transport Dynamics

With HHG, we are able to study ultrafast nanoscale dynamics. Among the vast range of interests of this field, in this thesis I focus on acoustic propagation and thermal transport at nanosystems in short time scales.

Many phenomena in nanostructures are mediated by the dynamics of lattice vibration (phonons) with wavelengths in the nanometer scale and frequencies in GHz-THz range. Lattice vibration can be induced by mechanical, electrical and optical stimulation. In the case of ultrafast time scales, mode-locked lasers are often used to excite electrons and induce photoacoustic waves through electron-phonon interactions. Monitoring the propagation of these photoacoustic dynamics can be a powerful tool for studying the mechanical properties of materials. In particular, photo-excited surface acoustic waves (SAWs) has a very shallow surface penetration depth proportional to the acoustic wavelength, thus their propagation is extremely sensitive to the surface structure and composition. Generating and controlling surface acoustic waves with nanometer wavelengths can be used to study the surface and interface properties of layered nano-systems, such as ultrathin films. On the other hand, benefiting from the same field which it is contributing to, the generation and propagation of photoacoustic waves can be designed and controlled using special designed nanosystems also called phononic crystals (i.e. periodic elastic composites of two or more vibrating materials[14]).

Phonons are also essential in energy transport because in many systems, such as semiconductors, the phonon is the primary energy carrier. As electronics seek to meet Moore's law expectations, thermal management in these nanoelectronic systems becomes a very challenging issue. Electrical heating can cause temperature rises to levels that will prevent reliable operation if not appropriately cooled. Heat transfer in nanoscale devices challenge the diffusive equation when the feature size of the device is smaller than or comparable to the mean free path (Λ) of energy carriers as no thermal equilibrium can be achieved without sufficient scattering between heat carriers. The mean free path of phonons varies a lot in different materials and can be a few hundreds of nanometers in

crystalline materials at room temperature. For a nanoscale heat source, severe temperature rises are reported from both modeling [15] and experiments [16] that suggest the Fourier diffusive law overestimates the heat dissipation from the nano heating source. Thus better models are needed for thermal design and management in nanoelectronics. As another example, reduced thermal conductivity is also reported in other nanostructures, such as in nanowires [12], multilayer structures [9], and carbon nanotubes[11]. These discrepancies are due to ballistic thermal transport at the nanoscales, which may further complicate the performance and design of nano-electronics.

1.3 Outline

This thesis is focused on two subjects: propagation of photoacoustic waves to study the mechanical properties of materials, and heat-carrying phonon transport for heat dissipation at the nanoscale.

In Chapter 2, I briefly introduce lattice vibrations, the definition of phonon, and different phonon branches. I also discusses basics of thermal transport. Then I review the key techniques which enable all the experiments presented in this thesis: high harmonic generation.

Chapter 3 presents several experiments in generating and detecting ultrashort-wavelength surface acoustic waves. I first use a sample patterned with a nano-grating to generate SAWs beyond the limit set by standard techniques. Then I extend it to more complicated systems, and generate the shortest wavelength SAW to date at 35 μm. I also demonstrate coherent control of SAWs generation which can selectively enhance higher-order acoustics while suppressing the fundamental order. In this way the SAW wavelength can easily be shortened by a factor of two.

In Chapter 4, I apply our techniques of nano-SAW generation to demonstrate a new photoacoustic metrology approach and use it to characterize mechanical properties of thin film samples. With nano-gratings patterned onto thin film samples, nanometer-wavelength surface and longitudinal acoustic waves can be generated simultaneously. By monitoring the surface oscillating modulation and measuring the velocities of both acoustic waves, we are able to derive the elastic properties of the thin film, such as Young's modulus and Poisson's ratio.

Chapter 5 studies phonon transport in terms of thermal dissipation. It starts with a theoretical model on how we can measure thermal transport using EUV beams, and reports our first observation of the quasi-ballistic effect when heat dissipates from a nanoscale heat source into a bulk heat sink. We prove that Fourier law overestimate the thermal transport rate, and apply a modified Fourier's law to analyze the heat dissipation process. We also build a model to relate the mechanical (thermal expansion), thermal (thermal transport) and optical response together in order to interpret our results.

Follow-up works of thermal transport at nano-interfaces are discussed in Chapter 6. We extend the study into 2D nanosystems, and observe stronger ballistic effect on the same feature size. We also measured the material and polarization dependence of the thermal transport. We also change the temperature of the sample to control the mean free path, and by this method, we are able to observe the quasi-ballistic effect without varying the nano-interface size. Finally we report the first attempt on dynamic thermal imaging.

The thesis is concluded in Chapter 7 with a summary of both photoacoustic waves and heat-carrying phonon transport probed by coherent EUV beams. Future directions for this field and other possible applications of HHG as a tool to study ultrafast dynamics in nano-systems are presented.

Chapter 2

Background

Crystal lattice vibrations, quantized as phonons, are discussed in great detail in many solid state physics textbooks [17, 18] and this topic has been an active research field for many decades. Here we give a brief introduction to the concepts that are close to our research, including phonons, photoacoustic waves and thermal transport when phonons work as heat carriers. After that, we also describe the experimental techniques used in this thesis. Instead of the standard optical pump-and-probe technique, we use an infrared pump and EUV probe to study photoacoustic and thermal dynamics in nanoscales. The key technique to generate the EUV probe beam, high harmonic generation, is also included in this chapter.

2.1 Phonon

Atoms in a lattice are connected via chemical bonds to their neighboring atoms. The lattice vibration is a collective oscillating displacement of the atoms from their equilibrium positions. Consider N atoms in a lattice, with their equilibrium positions R_n (in which n ranges from 1 to $3N$); a displacement vector $\mu_n(t)$ from the equilibrium position results in a new atom position $R'_n(t) = R_n + \mu_n(t)$. If the displacements are small, the potential energy of all the N atoms can be expanded in Taylor series around R_n as:

$$V(\mu_n) = V(0) + \sum_{i=1}^{3N} (\frac{\partial V}{\partial \mu_i})_0 \mu_i + \frac{1}{2} \sum_{i,j=1}^{3N} (\frac{\partial^2 V}{\partial \mu_i \partial \mu_j})_0 \mu_i \mu_j + \cdots . \tag{2.1}$$

The partial derivative is taken around the equilibrium positions. For small displacements, the linear term vanishes and third or higher order terms are negligible, thus the second order term dominates.

This is known as the harmonic approximation. The atomic potential of two atoms and its local harmonic approximation is shown in Fig. 2.1.

While quantum mechanics is required to obtain the concept of phonons, this harmonic approximation matches the classical mechanical model that atoms in lattice can be treated as masses connected by springs, as shown in Fig. 2.2. Therefore atomic motion equations will then be similar to the motion equation of a mass-spring system: $m\ddot{x} = -kx$. Consequently eigenmodes can be derived to explain the crystal lattice vibration.

This approximation yields a wave solution to the atomic equation of motion, with the energy of the harmonic oscillator given by $E_n = h\nu(n + 1/2)$, in which $n \geq 0$ is integer, and ν is the fundamental frequency of vibration. These wave solutions are also named lattice waves, or phonons.

A typical dispersion of these phonons as a function of wavenumber k is shown in Fig. 2.3 (top). It has a high-frequency branch (optical phonons) originating from out-of-phase oscillations of different atoms in a crystal cell, and a low-frequency branch (acoustic phonons) corresponding to in-phase oscillations. The phase velocity is given by $v_p = w/k$, while group velocity is $v_g = dw/dk$. Therefore optical phonons have slow phase velocity at small k, their high frequency make it possible to couple with photons, while acoustic phonons have fast phase velocity at small k contributing to energy transport and fast dynamics.

Phonon modes can also be divided into transverse and longitudinal waves by the relation of the propagation direction to the direction of vibration. Fig. 2.3(a) also shows transverse and longitudinal modes of both optical and acoustic phonon branches.

Although this classical mechanics model simplified the lattice vibration process, it still gives good approximation in terms of phonon modes. Fig. 2.3(bottom) demonstrates the measured phonon modes from silicon[4, 5], which also shows longitudinal and transverse phonon modes of both optical and acoustic branches.

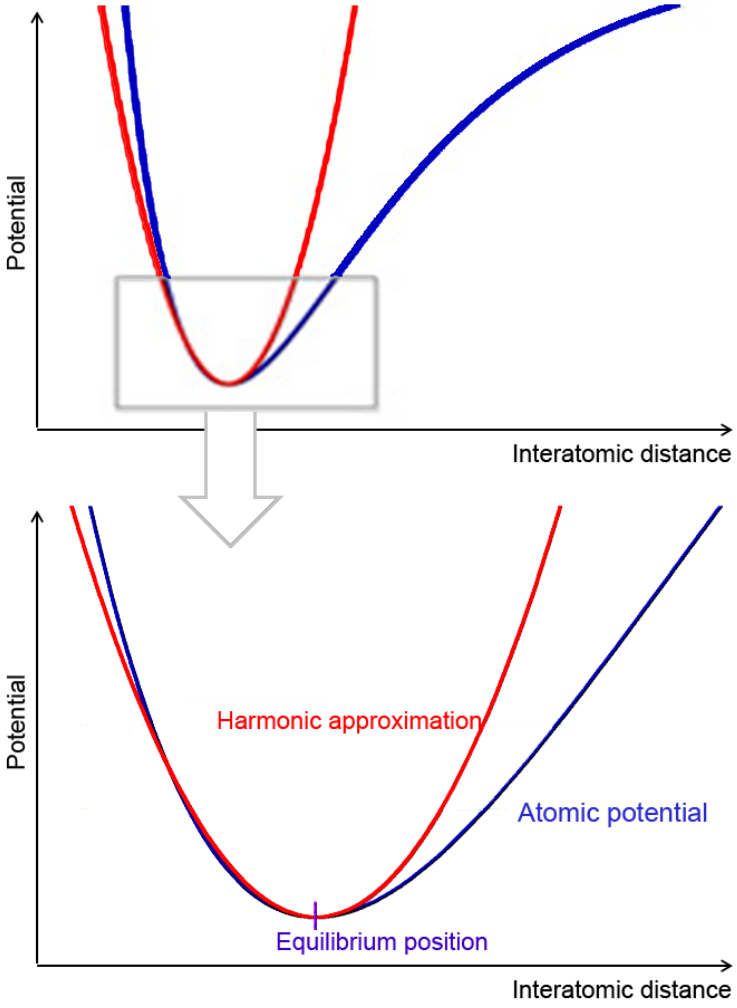

Figure 2.1: Top shows atomic potential in a lattice, which can be expanded as Taylor series around the equilibrium position (zoom in at bottom) when there is a small vibration. It allows a local harmonic approximation at the equilibrium position.

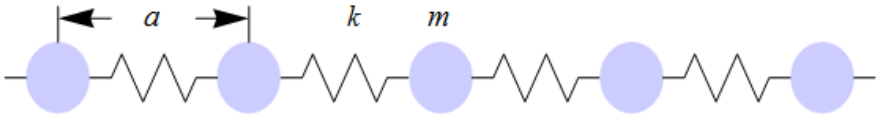

Figure 2.2: Classic mechanics uses a mass-spring model to describe atomic interaction and lattice vibration.

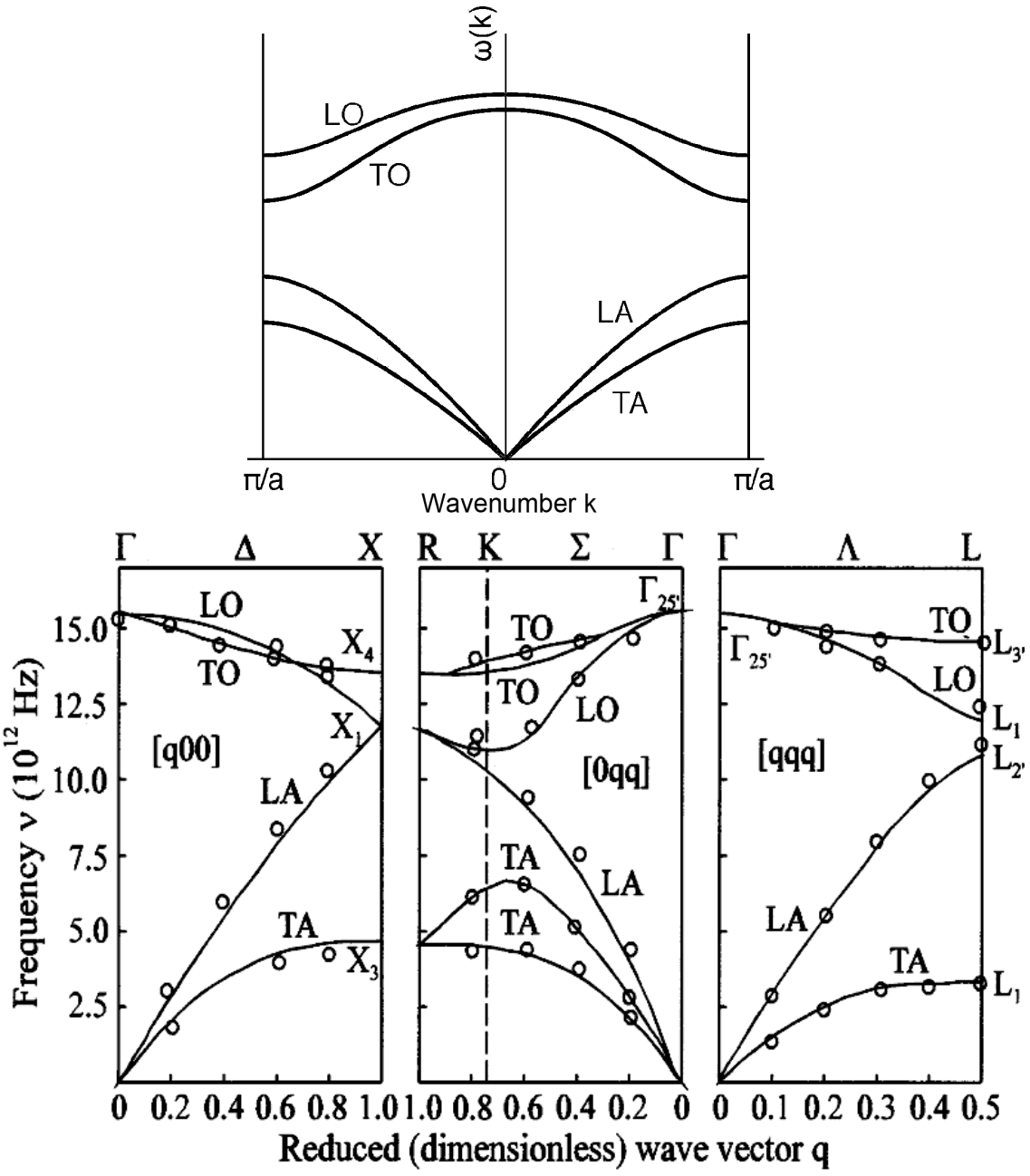

Figure 2.3: (Top) Calculated phonon dispersion map for 3D crystal using harmonic approximation: optical phonons have higher frequency but slower speed, while acoustic phonons have lower energy but higher speed. Longitudinal and transverse modes are shown separately as LO as longitudinal optical (LO) mode, transverse optical (TO) mode, longitudinal acoustic (LA) mode and transverse acoustic (TA) mode.(Bottom) Measured dispersion curves of acoustic and optical phonons of Si. Data from reference [4, 5]

2.2 Thermal Transport Through Phonons

Phonons carry energy as they propagate. In another words, like electrons in metals or atoms in a gas, phonons are the heat carriers in dielectric materials and semiconductors. Study of phonon transport is essential in understanding thermal transport and management in these materials.

In the macroscopic regime, phonons dissipate heat by conduction, which is driven by temperature difference. This conduction process usually can be described by the Fourier law (Joseph Fourier, 1768-1830) which relates the local heat flux to the local temperature gradient:

$$q = -k\nabla T, \tag{2.2}$$

where k is the thermal conductivity. In 1D case, this equation becomes

$$q_x = -k\frac{\partial T}{\partial x} = -\frac{k\Delta T}{\Delta x}. \tag{2.3}$$

Now bring the heat carriers in: if heat carriers fill in a space with a temperature gradient, move at a speed of v, and can move a average distance $\Lambda = v\tau$ (τ is the average travel time) before scattering, the net heat flux at one surface is given by

$$q_x = \frac{1}{2}(nEv_x)|_{x-v_x\tau} - \frac{1}{2}(nEv_x)|_{x+v_x\tau}, \tag{2.4}$$

where n is the number of heat carriers per unit volume and E the energy of each carrier. The factor $1/2$ is due to random vibration of carrier: only half go through this surface. At small distance(time), this equation is similar to the definition of derivative, so we can rewrite it as:

$$q_x = -v_X\tau\frac{d(Env_x)}{dx}. \tag{2.5}$$

Now introduce the thermodynamics relation of $U = nE$, where U is the local energy density per unit volume, and specific heat $C = dU/dT$. If we assume v_x is independent of x, this equation becomes

$$q_x = -v_x^2\tau\frac{dU}{dT}\frac{dT}{dx}. \tag{2.6}$$

In an isotropic system, $v_x^2 = v^2/3$, where v is the average root mean square velocity of the heat carriers. Combining this equation with the Fourier law

$$q_x = -(Cv^2\tau/3)dT/dx = -kdT/dx. \tag{2.7}$$

It is clear that $k = Cv^2\tau/3$, Since $\Lambda = v\tau$, $k = Cv\Lambda/3$. Λ is the average distance a heat carrier travels before it scatters with another one, which is also named mean free path. In a dielectric system, specific heat is a macroscopic parameter but phonon velocity is determined by the phonon spectrum, which is sensitive to temperature. Usually at room temperature, an averaged value, sound velocity, is used to describe an effective velocity of all phonons. Therefore the mean free path depends on phonon excitation spectra and temperature, and often refer to an average value.

Although the above model is over-simplified, the expression for the thermal conductivity is a good approximation[19] for most macroscopic systems.

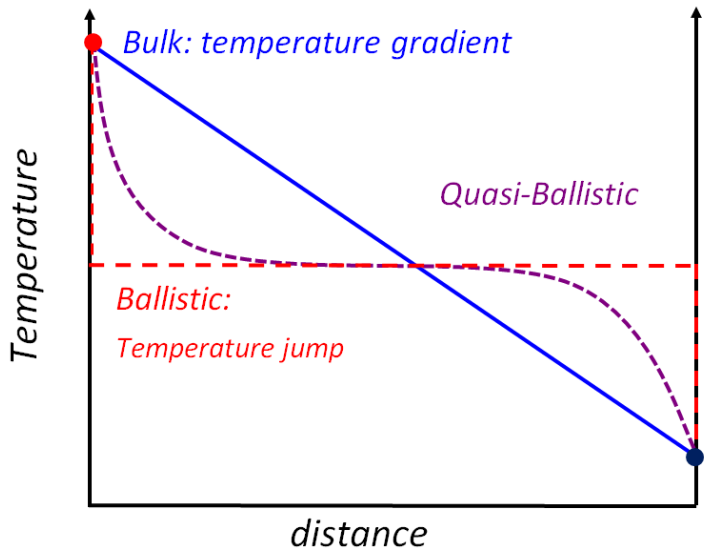

Figure 2.4: Schematic illustration of temperature distribution in three different heat transfer regimes: when mean free path Λ is much bigger than the distance d, temperature gradient in diffusive regime (blue solid line), sudden temperature jump in ballistic regime (no thermal equilibrium for temperature definition, red dashed line), and quasi-ballistic in between (purple dotted line).

The Fourier law is applied to most engineering situations and is the foundation of classical heat transfer analysis. However, the Fourier law is based on a local thermal equilibrium where

temperature can be defined, and Eq.(2.4) will break down when the feature size Δx is smaller than the mean free path of heat carrier. According to this criterion, thermal transfer across a temperature difference can be divided in three different regimes:(a) traditional regime of $\Delta x \gg \Lambda$ is the diffusive regime, where the Fourier law describes temperature distribution; (b) when $\Delta x \ll \Lambda$, there is no sufficient internal scattering and no thermal equilibrium to define a temperature in between, it is the ballistic regime; (c) between these two regimes, effects of both diffusive and ballistic contribute to a quasi-ballistic regime. Fig. 2.4 shows illustration of three thermal regimes.

To give an example of different regimes, the mean free path of the electrons in metal is typically around 1nm, but for phonons, Λ can vary in a big range, up to a few hundred nanometers in some materials. Thus it is easier to observe ballistic effects in some dielectric and semiconductor materials where phonons are heat carriers.

Ballistic thermal transport is becoming significant with the progress of nanotechnology, and many experiments have been attempted to observe the ballistic effect, especially in dielectric materials and semiconductors. The Boltzmann transport equation (BTE) can be used to fully describe the ballistic transport:

$$\frac{\partial f}{\partial t} + \frac{dr}{dt} \cdot \nabla_r f + \frac{dp}{dt} \cdot \nabla_p f = (\frac{\partial f}{\partial t})_c, \tag{2.8}$$

where f is the distribution function, t is time, r is spatial coordinate and p momentum coordinate. However, BTE solves differential equation, and can be very complicate to interpret. Computational simulations is often used, rather than any analytical solution, to model these systems and solve the Boltzmann equation.

In this thesis, I am interested in both thermal transport at nano-interfaces, and photoacoustic wave propagation from nanostructures to bulk material. I apply pump-and-probe technique throughout this thesis to obtain the time-resolved dynamics on both fields.

2.3 Pump-and-probe Techniques

Pump-and-probe techniques are common approaches that used in laser science. It generates an excitation in a system with a laser beam and measures the consequent changes with another laser beam. Laser-induced change often creates a modulation of an optical property, which in turn can be detected by the probe laser pulse as a function of time. Pump-and-probe techniques can be used in many different areas; for example, transient absorption, which is often used in chemistry and material science, measures the absorption change at a particular or a range of wavelengths as a function of pump-probe delay time after excitation by a pump light. Another example is transient thermoreflectance (TTR), which is a typical optical method to measure dynamic reflection changes due to thermal effect.

The advantage of using pump-and-probe techniques is to study fast dynamics, continuous-wave laser with a fast responding detector can be used in pump-and-probe technique, but more often a pulsed laser is used to monitor fast dynamic process signal. The excitation from an ultrafast laser pulse can generate a broad range of phenomena in materials similar to that from electronic or mechanic methods, including injecting heat, exciting photoelectrons, causing lattice expansion or vibration inducing nonlinear effect and so on. Furthermore, with an ultrashort pulse duration, it is possible to control the impulsive stimulation at a much shorter time scale than other methods of applying current or mechanical force. Meanwhile, many changes can be observed in an optical property change; for example, a surface modulation introduces additional phases in the optical path, some variation of the electron density yield changes in the refraction index, absorption at a band edge dramatically changes the optical absorption and transmission. Consequently, monitoring the changes of these optical properties with a laser pulse, especially ultrafast pulses, reveals the physical dynamics in a precise way on an ultrashort time scale.

On the other hand, since the probe can only detect an optical property change, in some circumstances it may reach a physical limit. For example, absorption changes dramatically when the laser has a wavelength corresponding to an energy bandgap; lasers have a diffraction limit

proportional to their wavelengths, so optical lasers usually detect systems with critical length around micron scale, and photon energy is limited by the band gap of the conduction and valence band of many natural materials. To overcome this limit and reach the nanometer regime, laser beams with higher energy and shorter wavelength are needed.

2.4 High Harmonic Generation

In our experiment, a unique tool using high harmonic generation provides us a coherent ultrafast EUV probe beam so that we can detect nanoscale dynamics induced by the fundamental infrared laser beam coming from the same laser source. With this improved infrared-pump and EUV -probe technique, we are able to study photoacoustic propagation and thermal transport in nano systems.

High harmonic generation (HHG) is an extreme nonlinear process that up-converts the energy. To achieve this nonlinear effect, very high peak intensity laser pulses are needed - which are usually obtained from an ultrafast (femtosecond) laser light. This conversion generates integer multiples of the fundamental frequencies from the incoming beam source.

Second harmonic generation (SHG) was first observed in 1961[20], one year after the invention of the laser. The famous story about second harmonic generation is that Peter Franken's first paper on SHG showed such small second harmonic signal from a ruby laser into a quartz crystal that the editor treated it as a dust spot and kindly removed it. This reveals the first studies of harmonic generation, where photons interact with nonlinear materials and generate new photons with twice the energy. For the next few decades, people successfully achieved phase matching between harmonics and fundamental laser beams, found higher-efficiency SHG materials, and also observed higher-order nonlinear process. This extended the accessible electromagnetic spectrum range of laser sources and enabled a broad range of applications from beam sources in research laboratories, imaging system in hospitals, to hand-held laser pointers.

In the late 1980s, HHG was observed and attracted great attention because instead of a low efficiency with low order harmonic generations, a broad region of high order harmonics of almost

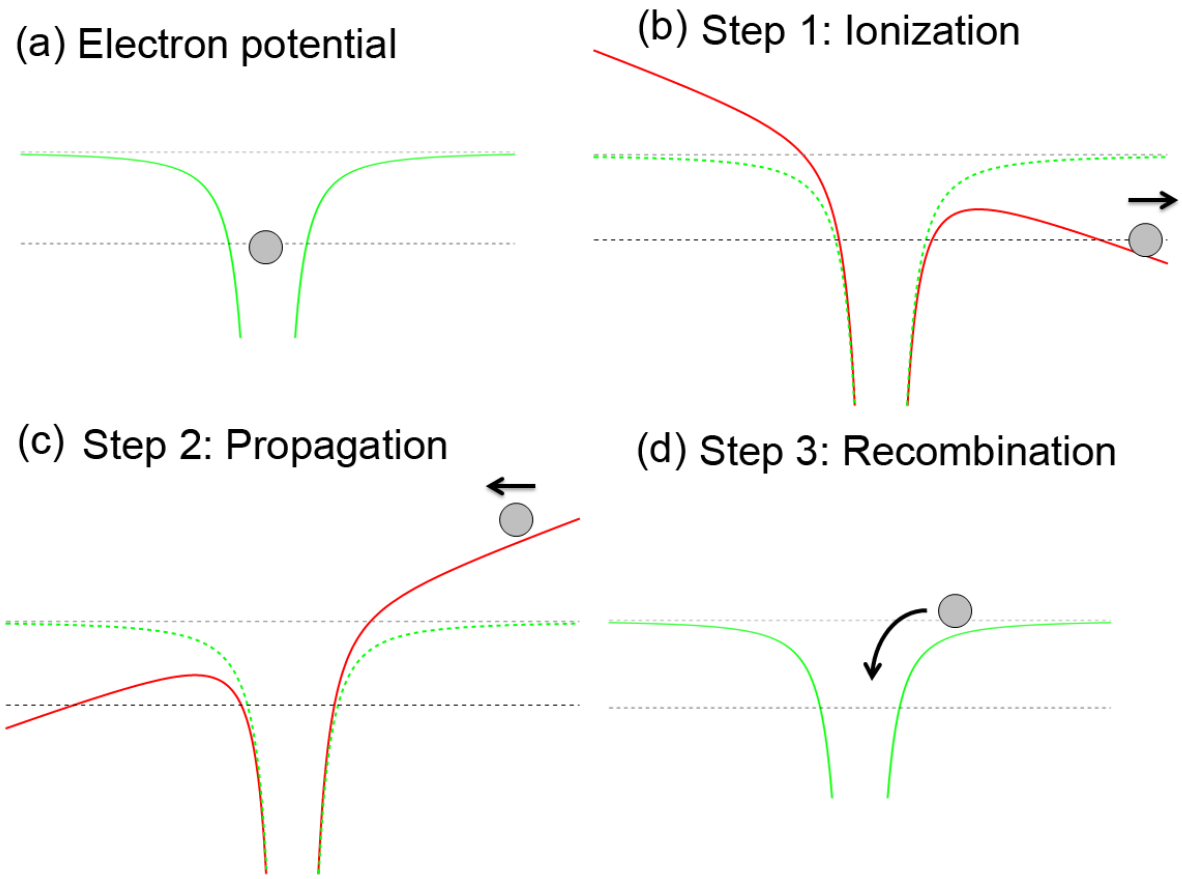

Figure 2.5: Semi-classical three-step model to explain high-order harmonic generation: an atomic potential (a) at rest is exposed in an intense laser pulse, tilting the potential, and resulting in the first step of HHG: tunneling ionization (b). The second step is free electrons propagating in oscillating electric field of the laser (c), and third step is when the electric field switches direction, and the electron recombines to the potential (d)

equal intensity was observed (later called the plateau region), before it hits a cutoff region. Great efforts have been made in both understanding this plateau behavior and pushing the conversion efficiency and cut-off energy to a higher level. Big steps in understanding these phenomena have been made with quantum mechanics by Kulander[21], and later with semi-classical analytical theory by Corkum[22]. The latter model also provides a visual description of the physical process for HHG and summarizes it as three basic steps:

(1) Tunneling ionization of an electron when its potential is modified by an intense laser field;

(2) The electron (now a free electron) is driven by the electrical field of the laser;

(3) The electron may recombine with the ion to its ground state, emitting a high-energy photon converted from kinetic energy of the electron.

High-order harmonic generation is distinguished from low-order harmonic generation mainly by the first step, the process of optical ionization. HHG requires an ultrashort intense pulse with peak intensities of $10^{14}W/cm^2$ or higher so that the electric field from the laser is comparable to the electron's Coulomb field making the tunneling ionization possible, as shown in Fig. 2.5 (b). After the atom is ionized, the electron becomes a "free" electron starting with zero velocity and accelerated by the oscillating electric field of the laser. When the laser field changes direction, there is a small probability that an electron will recombine with the ion into its ground state. In this case, the system will emit a photon with the energy equal to the sum of ionization potential of the atom and the average kinetic energy of an electron driven by the oscillating electric field of a laser wavepacket(i.e.ponderomotive energy). The cut-off energy of photon can be written as

$$h\nu_{cut-off} = I_p + 3.2U_p, \tag{2.9}$$

where I_p is the ionization potential of the gas atom and U_p is the ponderomotive energy depending on the field of a laser of intensity I_L and wavelength λ_L as $U_p \approx I_L\lambda_L^2$, as shown in Fig. 2.6. Noble gases are usually used in HHG because they have a higher ionization potential; for example I_p is around $45eV$ in argon and $100eV$ in helium. High laser intensity and longer wavelength tends to extend this harmonic cut-off.

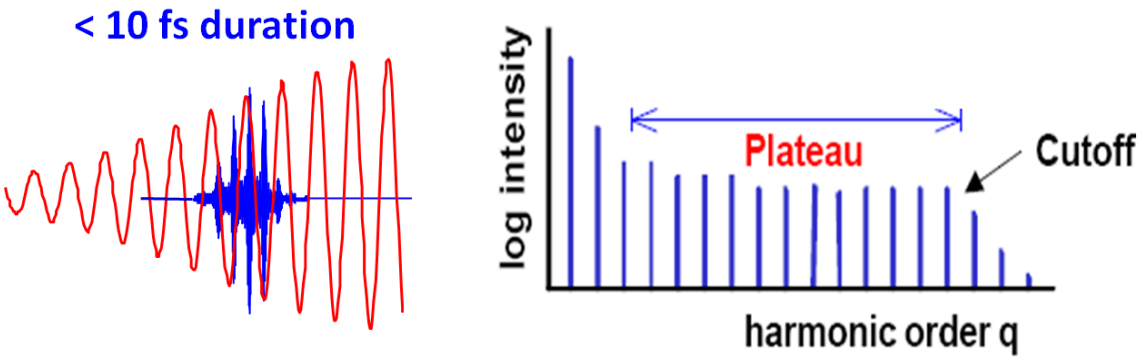

Figure 2.6: Illustration of (left) pulse burst of high harmonic generation from incoming IR beam sources, and (right) odd numbers of harmonic orders is generated from HHG. Peak intensity decreases rapidly for the first few harmonic orders, then levels out for several orders in a plateau region, then sharply drops at specific cutoff photon energy depending on the driven laser intensity and wavelength.

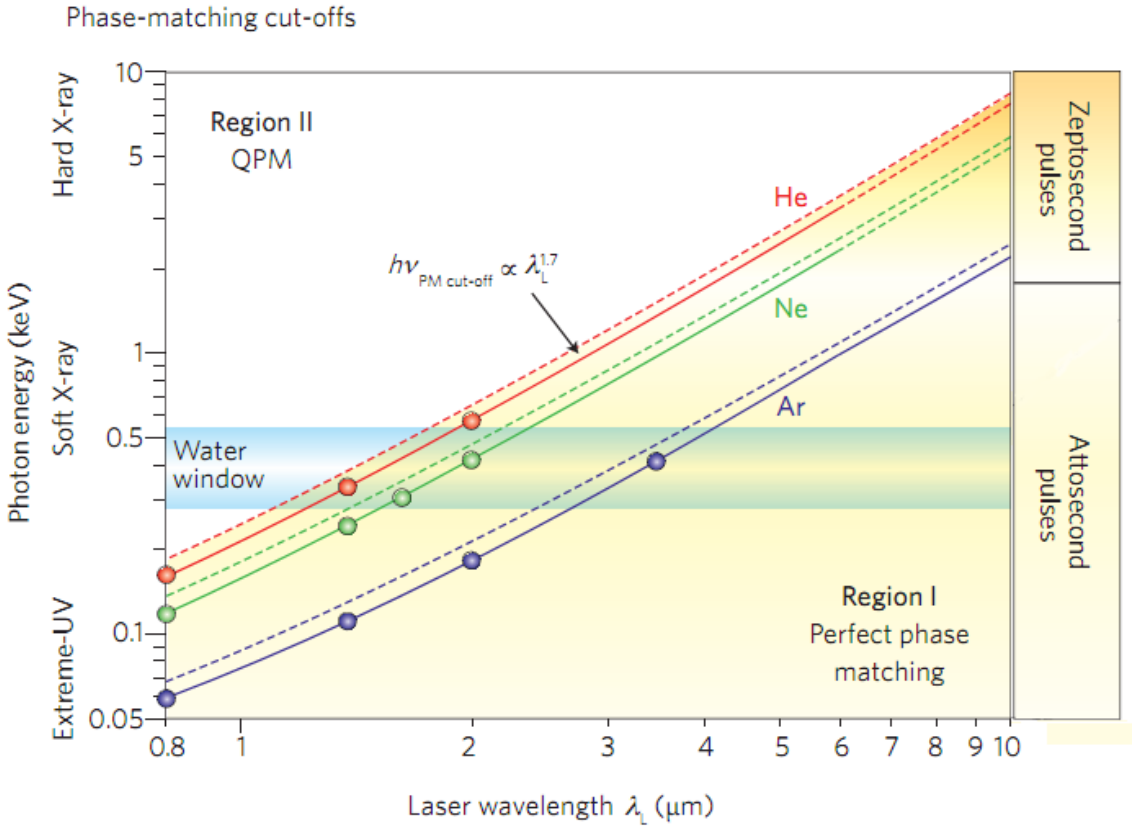

Figure 2.7: HHG phase matching cut-off energy as a function of driving laser wavelength from theory (lines) and experimental results (circles) on three different noble gases (He, Ne and Ar). The cut-off energy from experiments reaches soft x-ray range and in principle can achieve hard x-rays range. Figure from ref [2].

This model was subsequently expanded into a full semi-analytical, quantum mechanical model by Lewenstein et al in 1994[23]. This model quite accurately describes the characteristics of HHG seen experimentally, as well as providing a rigorous description of the picture of the semi-classical theory. In this theory, the emission of harmonic radiation from an oscillating dipole is given as a product of three probability amplitudes, corresponding to the three steps described above.

In experiment, HHG light can be generated by focusing an intense laser into a collection of gas atoms (usually the noble gas). To extend the interaction region, previous work in our group shows a hollow waveguide can be used to hold the gas and guide the laser beams, and more importantly, is helpful in phase matching. The phase mismatch between the driving laser and EUV beams arises from a combination of vacuum, neutral gas dispersion, non-linear refractive index plasma dispersion and waveguide dispersion. Hollow waveguide provides a freedom in adjusting the dispersion to achieve phase matching.[24] By extending the wavelength of the driving laser into near-IR range, perfect phase matching has been achieved in different noble gases (Helium, Neon, and Argon) and cut-off energies have been extended dramatically.[25, 26, 13, 21]

In this thesis, I use argon gas and 800nm input beam from 30fs Ti:sapphire amplifier to achieve a cut-off energy about 45eV with an EUV pulse duration less than 30fs. Aluminum filters with a few hundred nanometer thickness are used to block the fundamental and lower harmonic orders so that the typical HHG spectrum observed is centered at the $27th$ harmonic order, i.e. 42eV in energy ($\sim$ 30nm), as shown in Fig. 2.8. The full spatial coherence of this EUV beams (proved by double pinhole interference experiment[1]) together with short wavelength makes the EUV beams very sensitive to small phase shifts in interferometric measurement than that from optical lasers, and therefore very suitable in detecting surface modulation of nanosystems.

2.5 Conclusions

This chapter introduces the basic physics of lattice vibration, different phonon modes and heat conduction. In experiments, we apply a pump-and-probe technique to measure acoustic wave propagation and thermal transport induced by ultrafast infrared laser beams. For the probe, an

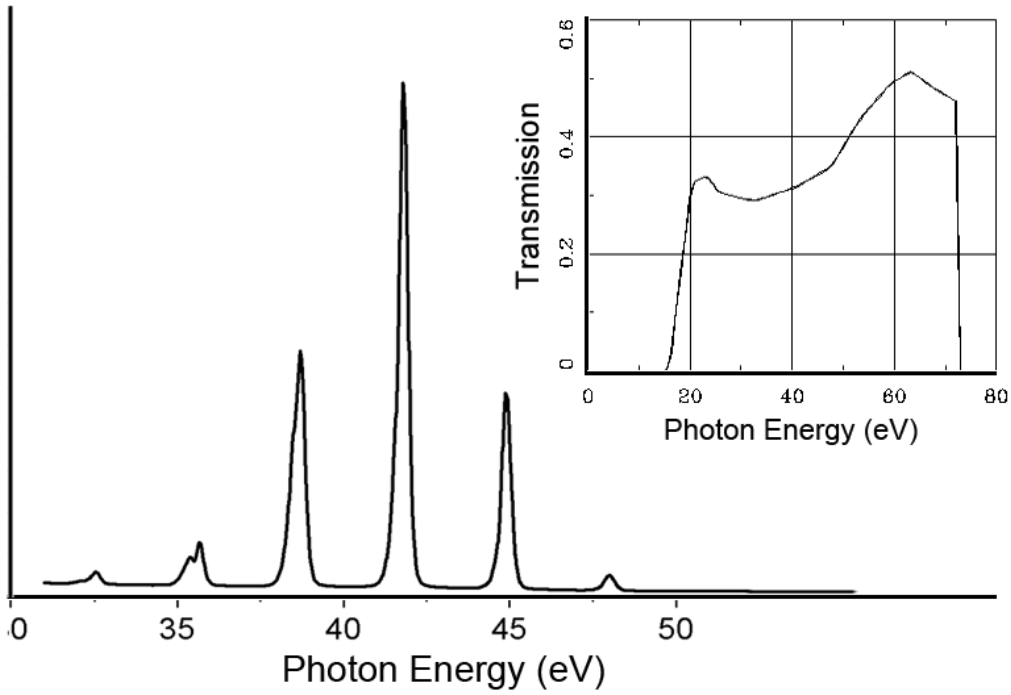

Figure 2.8: Typical harmonic spectrum from Argon gas after passing through aluminum filters. The left drop of signal is due to aluminum absorption, and right drop is because of HHG cutoff. Inset shows the aluminum transmission rate as a function of energy at normal incidence, with data extracted from ref [6].

intense beam from the same laser amplifier, is focused into an argon-filled waveguide to generate coherent EUV beams. With an ultrashort pulse duration, 30nm wavelength, and full spatial coherence, this EUV beam is excellent in probing nanosystems.

Chapter 3

Generation of Surface Acoustic Waves

3.1 Introduction

As discussed in Chap. 2, acoustic phonons have fast group velocity at small wavenumbers. The study of acoustics is usually related to time-resolved dynamics. As the first sentence of his famous "Acoustic Fields and Waves in Solids" book, Bertram Auld described the field of acoustics as: "Acoustics is the study of time-varying deformations, or vibrations, in material media"[27]. This covers the three most important parts of acoustics: dynamics, material dependence, and vibrational property.

This chapter focuses on study of acoustics and in particular, surface acoustic waves (SAWs). SAWs are acoustic modes that propagate while confined within a very shallow surface penetration depth, enabling a broad range of applications in signal processing and nondestructive material characterization. With a penetration depth corresponding to a fraction of the acoustic wavelength, SAWs are very sensitive to the mechanical properties of thin films, surfaces and interfaces[27]. SAWs with nanometer-scale wavelength are in great needs to precisely characterize the mechanical properties of nanostructured materials and systems such as multilayer and thin films, used in nanoelectronics and nano-bit patterned data storage devices.

Various approaches have been used to generate short-wavelength SAWs. A traditional mechanical transducer generates SAWs with a frequency limited by the electronic response time[28, 29]. Ultrafast laser pulses can also be used to impulsively heat a sample, inducing lattice expansion and thereby stress so that SAWs are launched. By focusing a laser beam onto a small spot, broadband

SAWs can be excited[30]. Alternatively, the interference between two overlapping laser beams can create a transient grating excitation and launch narrowband SAWs[31, 32]. However, the SAW wavelength excited by these techniques is limited by the wavelength of the pump laser beam, i.e. barely sub-micron scale for visible light. To overcome this limitation, nano-patterned gratings can be optically excited to create shorter wavelength SAWs[33, 34, 35, 36]. The wavelength of the SAW excited with nano-patterned structures is then only limited by the spatial period of the nano-pattern.

Several approaches for detecting short-wavelength SAWs have been demonstrated, including monitoring the strain-induced transient reflectivity change[35, 33, 34] and using interferometric techniques to observe the refractive-index modulation or optical phase changes induced by the surface displacement[37]. However, results from these detection methods can be complicated to interpret.

In this chapter, we use coherent extreme ultraviolet (EUV) beams, with wavelengths shorter than the SAW wavelength, to directly probe the SAW-induced surface displacement. This results in an extremely sensitive probe because the induced phase change on the EUV beam is significant comparing with optical beams. By exciting a pre-patterned nanostructures, SAWs at ultrashort wavelength can be measured.

3.2 Generation and Detection Surface Acoustic Waves using Sub-optical Phononic Crystals

In the first experiment, we use a 1D sub-optical phononic crystal that is impulsively heated by laser pulses to generate nanometer-wavelength SAWs. We designed two sets of 1D nano-patterned phononic crystals to generate short-wavelength surface acoustic waves (shown in Fig. 3.1). Sapphire is selected as the substrate first because it has a high elastic modulus and thus a high SAW velocity around $6300 m/s$. Also it is transparent for the laser 800nm pulses so that we can heat the nickel lines right at the interface of nickel and sapphire first using a geometry pumping from backside.

Nickel lines are prepared using electron beam lithography and lift-off technique in $120\mu m \times$

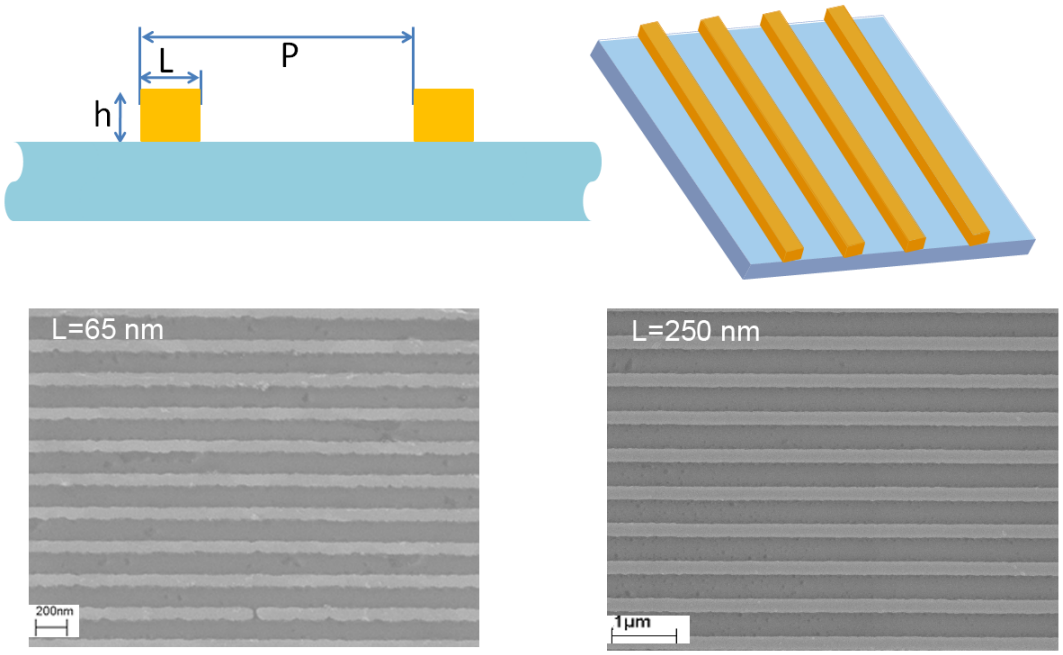

Figure 3.1: Illustration of 1D nickel patterned sapphire samples at side view (top left) and top view (top right), with the height, nano-pattern feature size and periodicity indicated by h, L and P respectively. The SEM images of these samples are shown at the bottom at L = 65nm and L =250nm gratings.

$120\mu m$ square regions. In each region, the gratings are fabricated 120μm long, and with a varied width and period and different height. The first set of samples have nickel stripes of height $h =$ 20nm, and width L varies between 65nm and 1μm, with a fixed duty cycle of 25%, so that the grating period $P = 4L$. The second set of samples have height of 10nm, line width L also from 65nm to 1μm, but a fixed duty cycle of 50% ($P = 2L$).

In this experiment, we use a Ti:Sapphire amplifier system with 2kHz repetition rate, $1.8mJ$ energy, 30fs pulse duration, and wavelength centered at 780nm. The output of the laser is split into pump and probe beams with a 80/20 beam splitter, as shown in Fig. 3.2. The 80% of the laser beam is focused into an argon-filled hollow waveguide to generate extreme ultraviolet probe beams through HHG as discussed in previous chapter. The probe beam spans a range of wavelengths centered at 30nm. This extreme nonlinear frequency upconversion process maintains (and even shortens) the femtosecond pulse duration and full spatial coherence of the driving laser.[13] The HHG probe beams pass through two thin Al filters, which block IR laser light and low order harmonics, the beam is refocused to a diameter of about 100μm on the sample by a toroidal mirror with an effective focal length 50cm. The pump beam is sent through a computer-controlled translation stage with two retro-reflection mirrors that can introduce a varied pump-probe time delay up to 8ns. Pump beam is finally focused onto the sample with a large spot size (about 600 $\sim$ 700μm diameter) in order to ensure a 5% uniformly heating region, i.e., a range that power drops 5% from the peak, according to the spot size of probe beam. The fluence is set at $3mJ/cm^2$, much lower than the damage threshold of the sample.

We use backside illumination on our samples to impulsively heat the nanostructure rapidly at the interface. This energy is first absorbed by electrons, then transferred to phonons causing sudden expansion of the metal lattice, which induces stress at the nanostructure/substrate interface, and launches acoustic vibrations in different directions: surface acoustic waves are localized along the interface of the nanostructure/substrate system perpendicular to the orientation of the nickel lines, while longitudinal acoustic waves travel into the substrate. In this experiment, we focus on the SAW mode, and will briefly discuss the longitudinal mode at the end of this chapter. The resulting

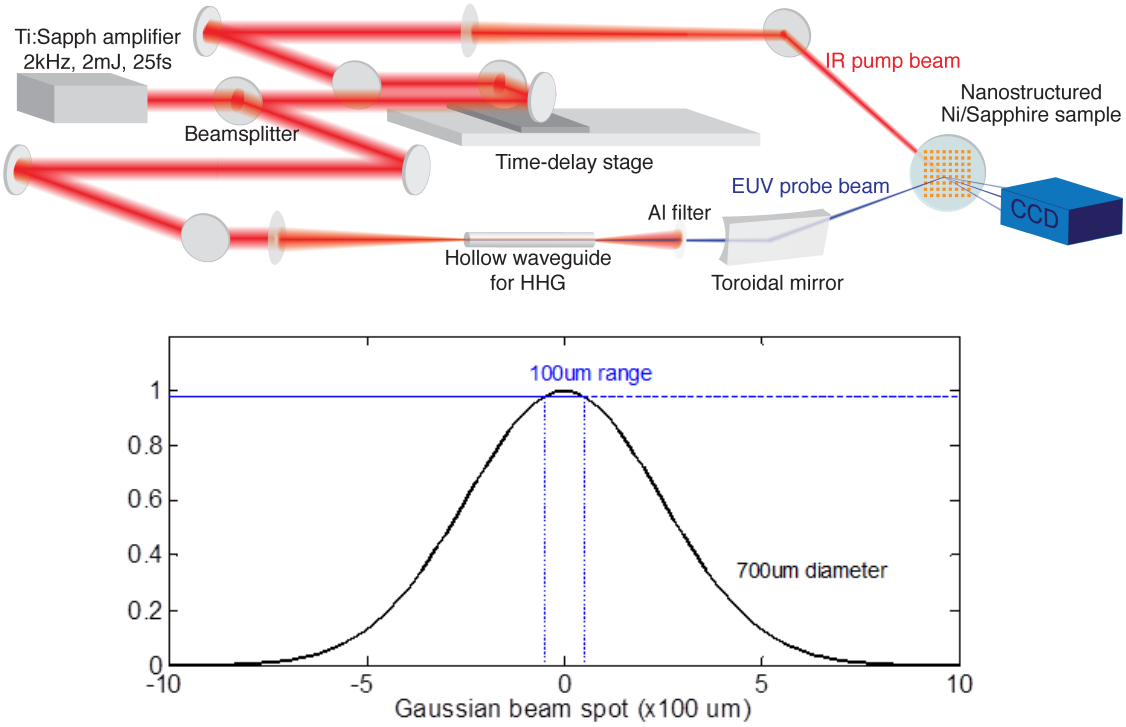

Figure 3.2: Schematic diagram of the experimental setup: (top) a femtosecond IR pump beam (800nm) is loosely focused onto the sample to generate SAWs; and a coherent HHG beam (30nm) then probes the time-dependent surface displacement as a function of time delay between the pump and probe beams. (bottom) Gaussian beam spot demonstrate how the pump beam size is selected to ensure a 5% uniformity for EUV probe beams.

displacement causes transient changes of the diffraction efficiency of the EUV probe beams, which can be monitored by an X-ray sensitive CCD camera as a function of pump-probe delay time.

A mechanical shutter has been used and synchronized with the CCD shutter. Diffraction signal at a fixed pump-and-probe delay time is recorded by subtracting shutter off (no pump) from the shutter on (with pump) signal in order to minimize temporal noise and improve the signal to noise ratio. For the 1D grating, diffraction signal as a function of pixel numbers is shown as Fig. 3.3: red curve is signal from pump off and blue curve from pump on. Main peaks are from grating diffraction with $d \sin\theta = n\lambda$, where n is the diffraction order. The strongest peak at about 340 pixel is the 0^{th} order, peaks at about 280 and 390 pixels are $\pm 1^{st}$ orders, and peaks at around 220 and 450 pixels are second diffraction orders. For each non-zero diffraction order, three or four weaker peaks can be observed, which origin from different HHG orders. Bottom of Fig. 3.3 shows the zoomed pure signal after subtraction on a $P = 2000$nm grating. Since the 0^{th} order signal changing in an opposite direction to that from other diffraction orders, the total signal at a fixed delay time is a sum of the absolute changes at all diffraction orders. By measuring this total signal changes as a function of pump-probe delay time, we can observe the dynamic propagation of the SAW.

We measure pump-on minus pump-off diffraction signal at different pump-and-probe delay times on all grating sizes of two sets of sample. Fig. 3.4 shows typical signal at four dynamic scans with period $L = 800$nm and $L = 80$ from both nickel-on-sapphire samples. The fast rise and long decay signal components are caused by the thermal expansion induced by the pump beam, followed by subsequent heat dissipation from the nanostructure into the substrate[38]. The fast oscillation signal is due to the surface acoustic waves. Fast Fourier transform (FFT) was used to extract the frequency from the oscillation and shown in Fig. 3.3. The relative change in EUV diffraction signal in this experiment is about 2%, which is $5-10\times$ higher than that demonstrated using optical probe techniques[33, 34]. As explained latter in this chapter, this makes it possible to observe, study, and even control higher-order SAW dynamics.

From frequency spectra of Fig. 3.4, for $L = 800$nm, SAWs in $P = 4L$ sample have a dominant

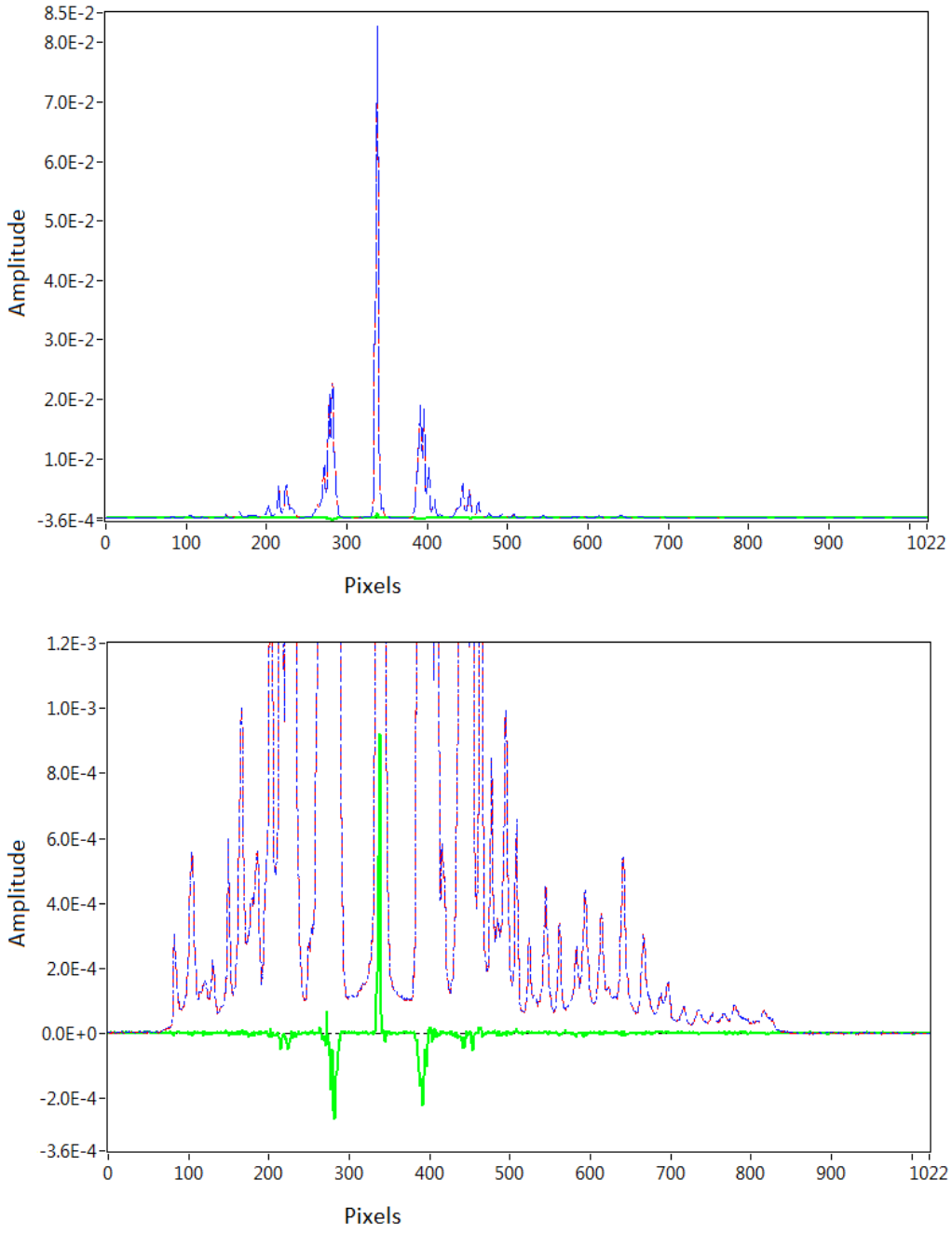

Figure 3.3: EUV diffraction on CCD with pump pulse on and off after zero delay time on $P =$ 2000nm nickel-on-sapphire sample. The subtraction of pump off from pump on provides the "real" signal from pump beam. Top is in large scale to show pump on (blue dashed line) and pump off (red dotted line) overlapping with each other with small difference. Major peaks correspond to $0th$, $\pm 1st$ and $\pm 2nd$ order of grating diffraction while weaker peaks on top of them (visible in $\pm 2nd$ order) are from different HHG orders. Bottom shows the subtraction after zoom in scale.

fundamental order frequency of 2 GHz, while frequency on $P = 2L$ sample is 4 GHz. And for $L = 80$nm, $P = 4L$ yield 20GHz while $P = 2L$ obtain 40GHz. These results indicate that SAW frequency is set only by the period of nano-gratings and prove the acoustic dynamics is dominated by propagation in the substrate rather than the normal mode resonances of individual wires[33, 35, 34]. Therefore the periodic modulation from the nano-gratings actually narrow the excitation spectrum of SAWs into narrow bands with SAW wavelength $\Lambda = P/N$, where P is nickel grating period, and N is integer; at $N = 1$, $\Lambda = P$ is the fundamental order. In this experiment, the shortest wavelength generated is from the $P = 2L$ sample, at $\Lambda = 125$nm.

This experiment also provides us an approach to systematically study SAWs with nanoscale wavelengths, which is of great interest in understanding the physics and also has great importance in future applications. As the grating period and thus the SAW wavelength shrinks, the penetration depth of SAWs decreases. Thus the propagation of SAWs changes as it becomes more sensitive to the nickel, which has a slower velocity ($4840m/s$) for SAWs. This effect can be revealed in SAW dispersion map, i.e. acoustic frequencies as a function of fundamental wavenumber k ($k = 2\pi/P$), as shown in Fig. 3.5.

The phase velocity of the SAW is given by $v = \omega/k$, the SAW velocity can be calculated from the coordinate of each point on the fundamental order in the dispersion map. For long acoustic wavelengths (large P and small k), the penetration depth is long, so the SAWs propagate in the substrate and the effect from the nanostructure can be ignored. The SAW velocity is close to the Rayleigh velocity in the sapphire substrate at $6200m/s$. The black dashed line in Fig. 3.5 represents a fit to the velocity corresponding to the first few data points i.e. the longest SAW wavelengths and penetration depths.

The higher wavenumber k (shorter wavelength) data plotted in Fig. 3.5 clearly deviates from the constant Rayleigh velocity, indicating that the speed of the SAWs decrease with wavelength, i.e. the periodicity of the nanostructure. To further explore this trend, we plot the SAW velocity as a function of wavenumber as shown in Fig. 3.6, and in order to makea direct comparison between the two sample measurements, the horizontal axis is selected as $kh\eta$ (η is the duty cycle, i.e., 50%

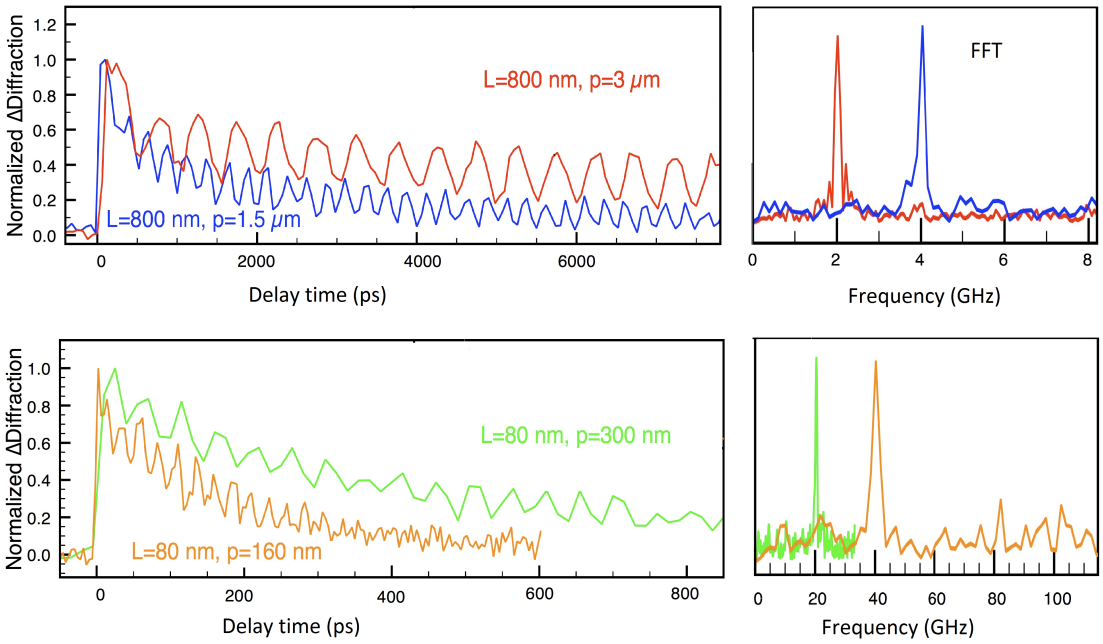

Figure 3.4: Dynamic EUV diraction from surface acoustic waves on samples of 1D nano-patterned nickel lines on top of sapphire substrate. Nickel lines of $L = 800$nm and $L = 80$nm are shown here. Impulsive heating and rapid thermal expansion launch surface acoustic waves with the bandwidth narrowed down by periodic modulation of gratings. The SAW oscillation frequency is take with a fast Fourier transform and shown on right. From the frequency spectra, we verified that the SAW period is set by the period of nanostructure.

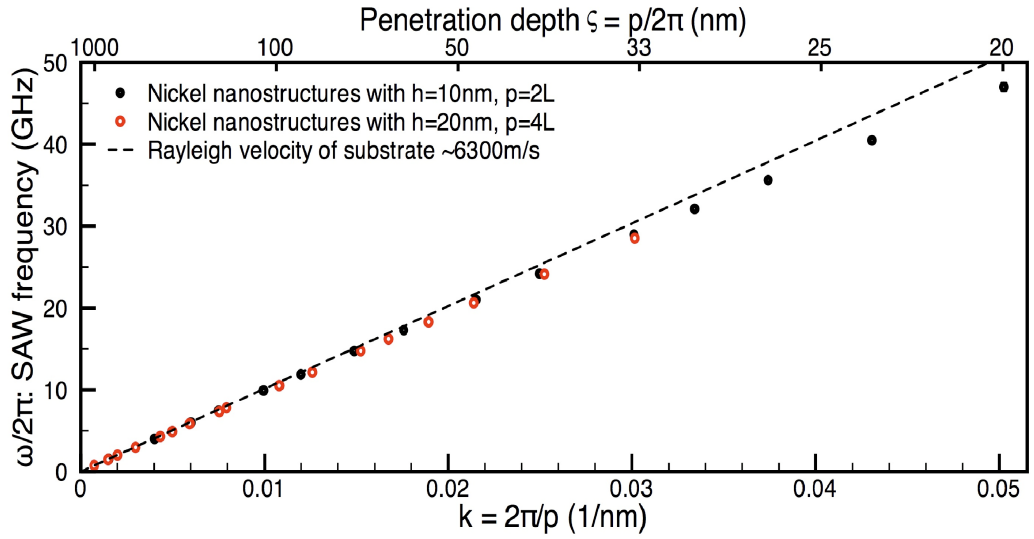

Figure 3.5: Dispersion map to show surface acoustic wave frequency as a function of wavenumber ($k = 2\pi/P$) for propagation in two sets of samples with nanopatterned nickel on sapphire. As the wavenumber increases (period decreases), the penetration depth of SAWs decrease. The frequency of SAWs and velocity measured from 1D gratings deviate from the Rayleigh velocity of sapphire substrate, indicating the increasingly effect from the nickel nanostructures.

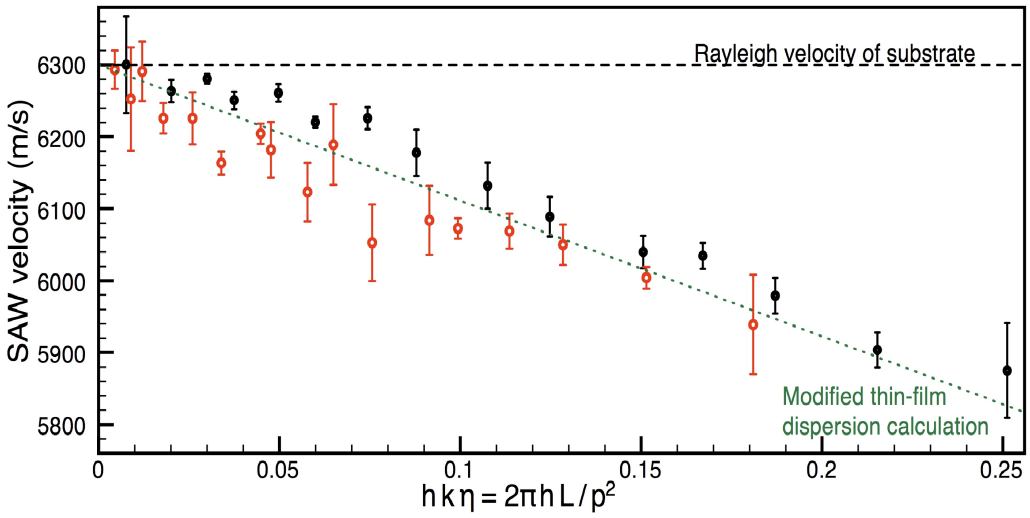

Figure 3.6: Velocity as a function of $hk\eta$. Black dashed line corresponds to Rayleigh velocity of sapphire substrate, red circles and black dots are measurements from $P = 4L$ and $P = 2L$ sample respectively. The measured velocity dispersion agrees with a modified thin-film dispersion calculation from effective mass-loading model (green dotted line).

and 25% for two sets of samples). It is clear that there is significant deviation from the Rayleigh velocity of sapphire (horizontal constant line) at large wavenumber k.

To explain this phenomena, an effective mass-loading model is applied. Because the SAW velocity is slower in the metal nanostructure than that in the substrate, the nanostructure will slow the SAW propagation. As the period of the nanostructure, and thus SAW wavelength, gets smaller, the SAW penetration depth decreases, so that it is more affected by the nanostructure that that from larger SAW wavelength case. This contributes to the deviation from the Rayleigh velocity of the sapphire substrate. Also as the period of the nanostructure shrinks while the height remains constant, the effective mass of the nanostructure increases, resulting in a decreasing SAW speed. A simple effective mass-loading model, Datta and Hunsinger approximation[39] introducing a duty cycle factor $\eta = L/P$ from thin film theory by which the dispersion effect is multiplied, matches our measurement well as shown as a dotted purple line in Fig. 3.6.

In conclusion, in this first experiment we generate nanoscale wavelength SAWs by heating sub-optical 1D gratings using ultrafast IR pulses and detect it EUV beams. The shortest SAW wavelength achieved is 125nm, with a SAW frequency as high as $47GHz$. This technique can be extended to even shorter wavelength by using smaller nano-gratings.

3.3 Generating Surface Acoustic Waves in 2D Nanostructures

Given the success of the first experiment, we extend our measurement from 1D to 2D phononic crystal samples, to study the effect from dimensionality and also to generate even shorter wavelength SAWs with a smaller grating period.

The samples in this experiment consisted of two sets of 2D nano-patterned gratings, as shown in Fig. 3.7. Both samples were prepared using electron beam lithography and lift-off techniques, covering multiple $150\mu m \times 150\mu m$ regions. To relate directly to previous experiment, the first sample set in this experiment is a 2D version of the nickel-on-sapphire sample that was used in the previous experiment, consisting of 2D nano-arrays of 15nm high nickel pillars on sapphire substrate, with pillar widths L ranging from 25nm to $1\mu m$, also at a fixed 25% duty cycle ($P = 4L$).

This set of samples could be compared with the 1D Ni/Sa sample to demonstrate the influence of dimensionality. Our sample II had a geometry similar to sample I, but with perpendicular anisotropy Co/Pd multilayer pillars, which are of great interest since they are commonly used as a model system for bit patterned media (BPM)[40, 41]. This grating consisted of 15 nm high multilayer pillars of width L ranging from 20nm to 1μm patterned on a silicon substrate, with grating periodicities ranging from from 35nm to 1.2μm.

Because silicon is opaque to the 800nm pump pulse, in order to adopt the experimental setup for both samples, we modified the pumping illumination geometry from back side to front side as shown in Fig. 3.8. The absorption depth of silicon for 800nm is a few microns, thus the pump laser pulse is absorbed mainly by the nanostructures and rapidly heats them up. Therefore when the pump pulses hit the substrate from the front surface, laser energy is first absorbed by electrons, while fast electron-electron and electron-phonon scattering rates rapidly establish thermal equilibrium within the metallic nanostructures on the sub-ps time scale.

We measured the time-resolved dynamics on varied grating sizes for both sets of samples. A typical signal is shown in Fig. 3.9: signal for 2D Ni nano-pillars of period of 1400nm (a) and 240nm (b) on top of sapphire substrate; and for 2D layered Co/Pd nano-pillars of period 300nm (c) and 45nm (d) patterned on silicon substrate. As discussed in previous section, the fast rise and decay components are from thermal absorption and relaxation. In the previous case, 1D nano-phononic crystal generates narrow band SAWs which have a dominate wavelength equal to grating period. However, 2D nano-structures give more complex boundary conditions in generating SAWs so that the frequency is more complicate to interpret, and noise from thermal background is more likely to disturb the oscillation frequency spectrum. Therefore instead of doing a direct fast Fourier transform in previous experiment, here we remove the thermal decay signal by using a simplified exponential fitting before taking a FFT of the oscillation signal. In the rest of this thesis, if not indicated, FFT for acoustics refers to Fourier transform after removing the thermal background.

By comparing the spectra of 2D and 1D result from previous section, it is very clear that more SAW frequencies are generated for the 2D phononic crystal sample than in the 1D case. The

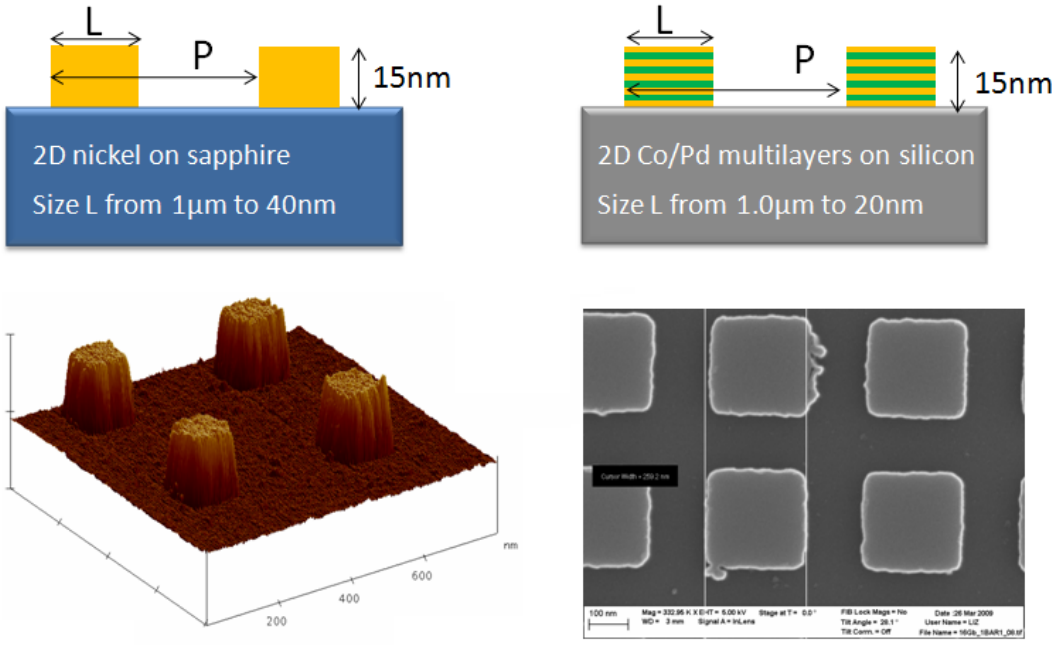

Figure 3.7: Geometry for two sets of samples used in this experiment: (left) side view and AFM images of 2D arrays of nickel on top of sapphire substrate; (right) side view and SEM images of 2D Cobalt/Paladium multilayers on top of silicon substrate.

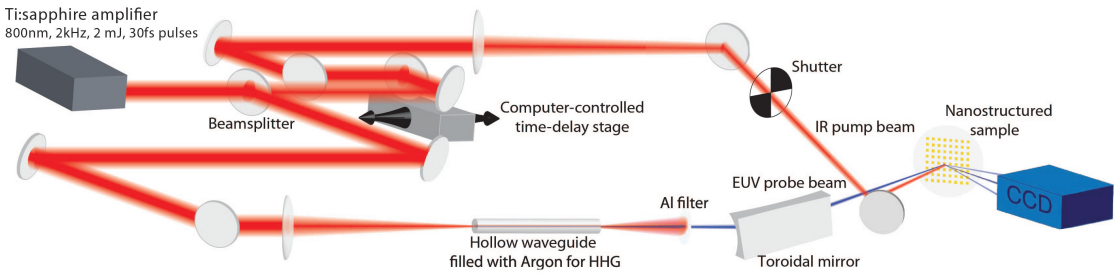

Figure 3.8: Modified geometry to adapt for front side pumping of both nickel-on-sapphire and Co/Pd multilayer patterned silicon 2D samples.

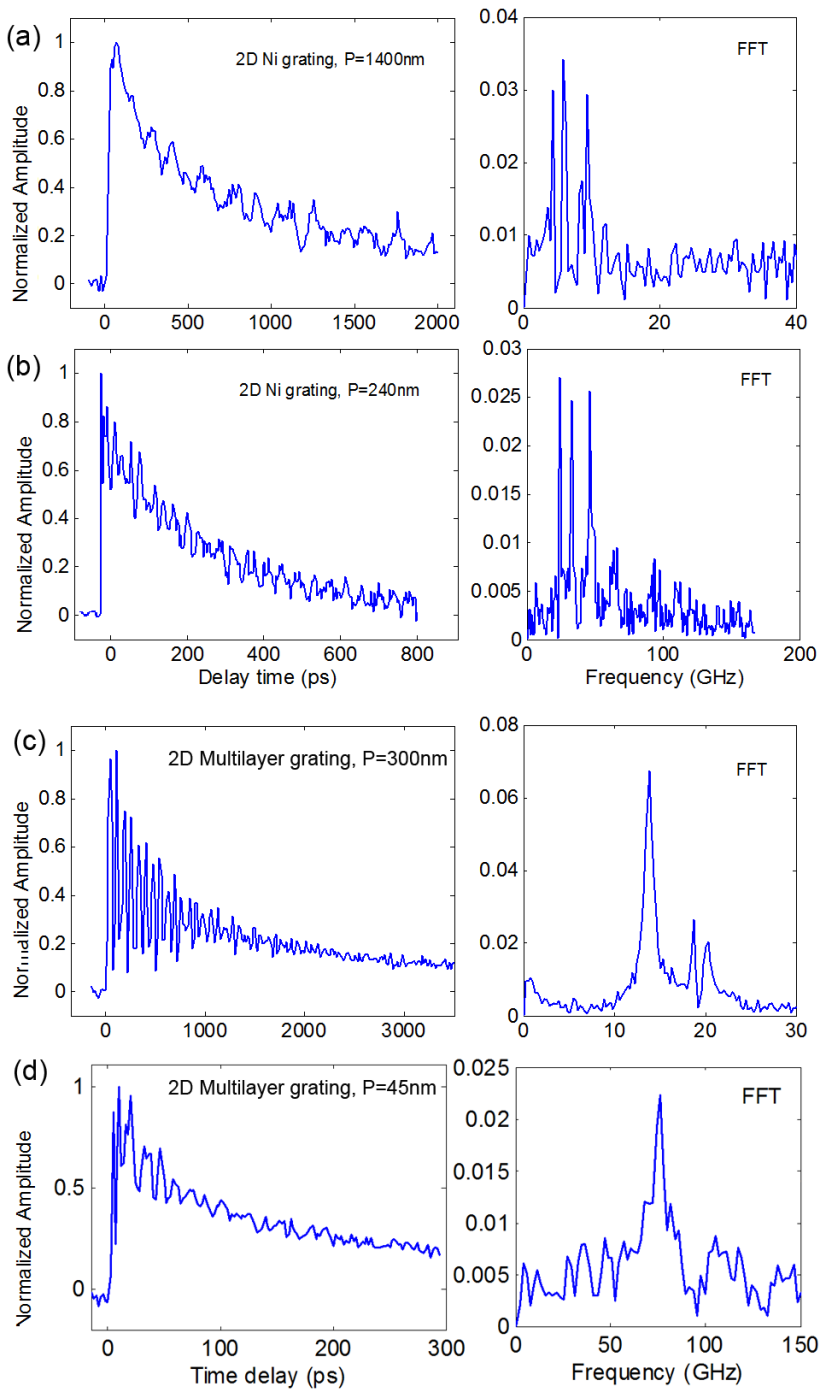

Figure 3.9: SAW oscillation signal as a function of pump-probe delay and Fourier transform for 2D nickel nano-arrays of (a) period P=1400 nm (b) P=240nm on sapphire substrate and for Co/Pd multilayer pillars of (c) $P = 300$nm and (d) $P = 45$nm coated on silicon substrate. The surface acoustic signal is extracted by removing the slowly decaying thermal signal (which transforms the blue curve to the green curve in top left). A Fourier transform is applied to obtain the frequency spectrum.

lowest acoustic frequency corresponds to the fundamental SAW frequency f_0, that is $\Lambda = P$; while the second peak corresponds to SAWs with a frequency equal to the diagonal periodicity, which is $\sqrt{2}f_0$. The third peak corresponds to the second-order SAW frequency, which is approximately $2f_0$. The shorter wavelengths correspond to stronger surface confinement and the propagation of higher-order SAWs in the multilayer pillar sample is weaker than in the nickel-on-sapphire sample, possibly due to stronger scattering at the multilayer's multiple interfaces. However, due to the small pillar widths (20 nm) and periodicity (35 nm) in this sample, the fundamental SAW wavelength of 35 nm corresponds to the shortest wavelength SAW observed to date.

Measuring the SAW dispersion is important for characterizing interfaces and thin films. For the complex 2D phononic crystals studied here, SAW frequencies as a function of wavenumber for samples I and II are plotted in Fig. 3.10. In the case of the 2D nickel-on-sapphire sample, three SAW frequencies are selected. To better distinguish these orders in the figure, all frequencies are plotted as a function of the fundamental wavenumber k_0 ($k_0 = 2\pi/P$). The phase velocity of the SAW is given by $v = \omega/k$, thus v can be extracted directly from the measurement. Compared with the fundamental k_0, higher order SAWs have shorter wavelengths and larger wavenumbers by a factor of $\sqrt{2}$ for diagonal and by 2 for second order. Their velocity can be calculated accordingly. The solid line represents a fit to the velocity corresponding to the first few data points, i.e. the lowest values of k or longest SAW wavelengths and penetration depths. The slope extracted from the fundamental SAW is $6090m/s$ - consistent with the Rayleigh velocity in the sapphire substrate. The velocities extracted from the diagonal and 2nd order SAWs are $6020m/s$ and $6150m/s$ respectively. In sample II (Co/Pd multilayer phononic nanocrystal sample), only the fundamental SAW dispersion relation is plotted, and the solid line is in agreement with the Rayleigh velocity of the silicon substrate, $4840m/s$.

The higher wavenumber k (shorter wavelength) data plotted in Fig. 3.10 clearly deviates from the constant Rayleigh velocity, indicating that the speed of the SAWs decreases with wavelength (as the periodicity of the nanostructure decreases). To further explore this trend, we plot the SAW velocity as a function of wave number for the fundamental, diagonal and second orders, as shown

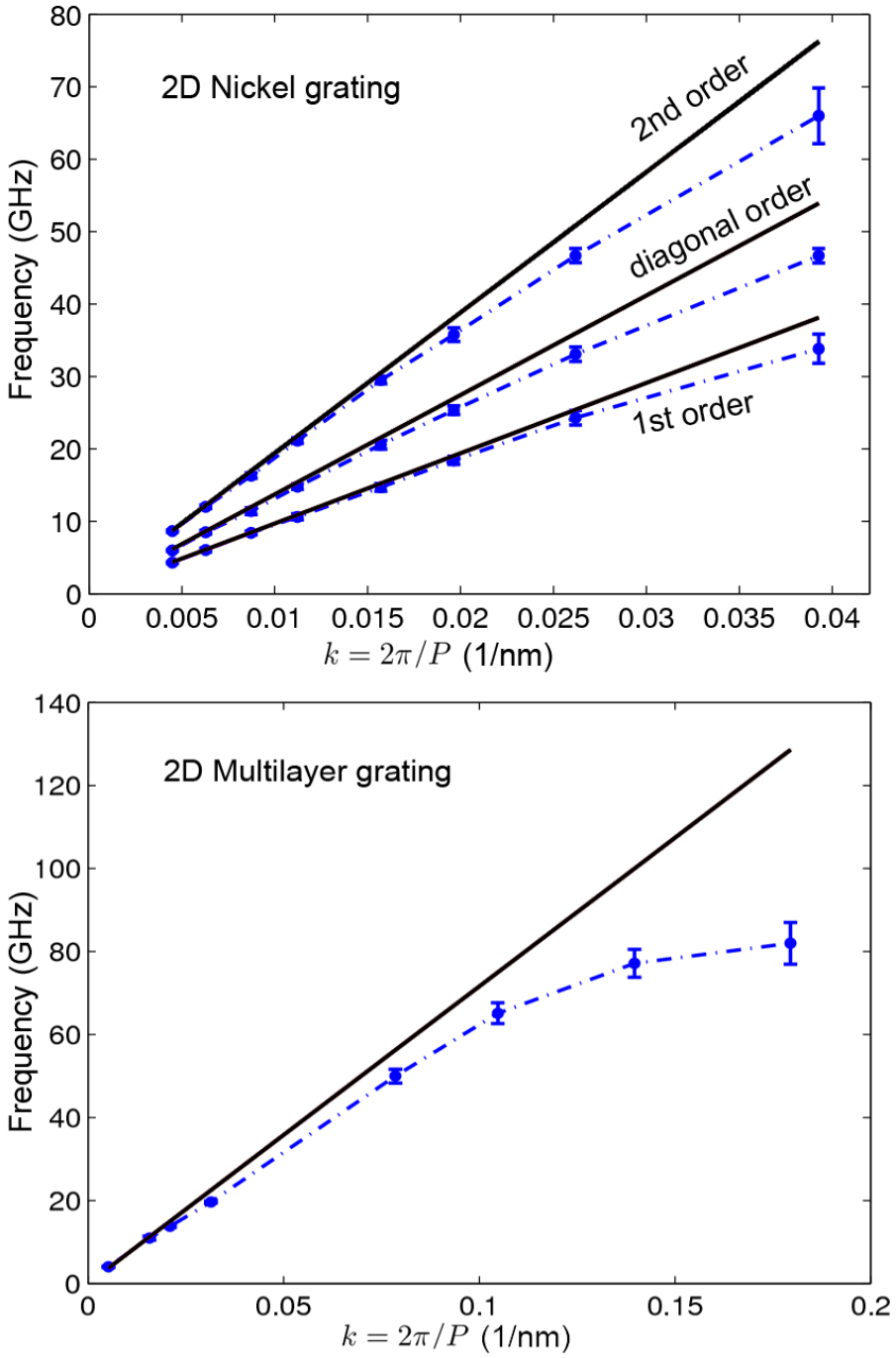

Figure 3.10: Dispersion relations: frequency as a function of fundamental-order wavenumber $k = 2\pi/P$. (top) Fundamental, diagonal and second order SAWs on the 2D nickel-on-sapphire sample (sample II). (bottom) Fundamental SAW on Co/Pd multilayer-on-silicon sample (sample III). Solid lines show the Rayleigh velocity of the substrate multiplied by the SAW order.

in Fig. 3.11 for sample I. It is clear that there is significant deviation from the Rayleigh velocity of sapphire (horizontal constant line). In order to explain this behavior, two approaches were explored. First, as in 1D case, we considered an effective mass-loading approximation. Because the SAW velocity is slower in the metal nanostructure than that in the substrate for all of the samples, the nanostructure will slow the SAW propagation. As the period of the nanostructures, and thus SAW wavelength, gets smaller, the SAW penetration depth decreases so that it is more confined in the nanostructure. This contributes to the deviation from the Rayleigh velocity of the sapphire substrate. Decreasing the period of the nanostructures at a fixed duty cycle, the height of the nanostructure does not scale down accordingly but remains constant. The mass of the nanostructure is thus not proportionally decreasing and the surface mass density is higher for the smaller gratings, resulting in a decreasing SAW speed. A simple effective mass-loading model, derived from thin film theory using the Datta and Hunsinger approximation[39], is shown as a dotted purple line in Fig. 3.11. This approximation worked well in previous experiments with 1D nano-structures, which are reasonably comparable to thin films, suggesting that this a valid approach. However, the surface coverage is much lower in 2D nanostructured gratings, and this model underpredicts the SAW dispersion by one order of magnitude.

A more accurate method to reproduce the dispersion of 2D phononic nanostrutures is based on first-principles modeling of the thermomechanics of the impulsively excited samples using finite element simulations[42, 43]. We calculate the spatially modulated heat-driven initial expansion of the nano-grating. The resulting displacement field is projected over the set of eigenmodes of the nanostructured sample, solutions of the acoustic eigenvalue problem. This technique unambiguously resolves which eigenmodes are impulsively excited. The main contribution to the sample dynamics is thus revealed as a symmetric SAW and we can directly determine its frequency. This is the first time this technique has been applied for nanostructures less than 200nm in size in a 2D geometry. The fundamental SAW-velocity result of this finite element analysis is shown as a blue solid line in Fig. 11, and demonstrates excellent agreement with the data.

While we can explain the deviation from the Rayleigh velocity by considering the properties

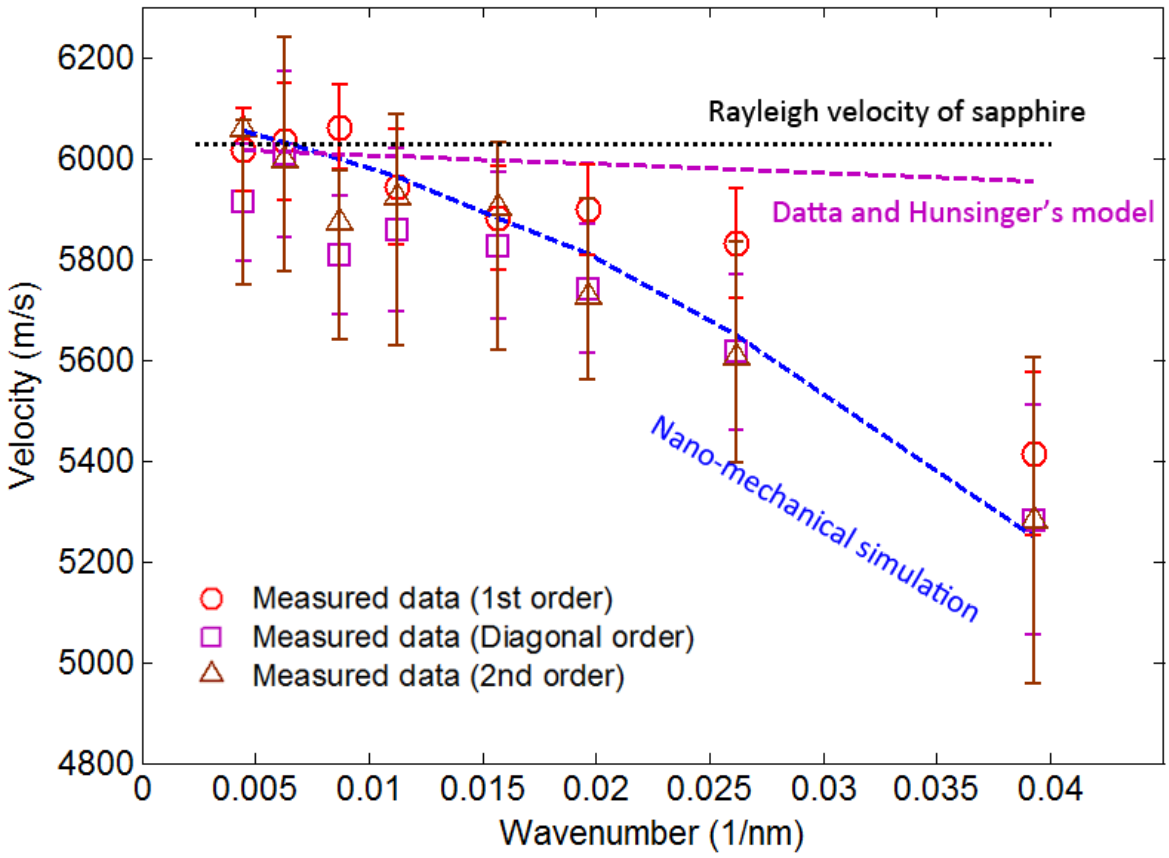

Figure 3.11: Velocity dispersion for the 2D nickel-on-sapphire sample II from fundamental, diagonal and second order SAW oscillations. The black dotted line shows the Rayleigh velocity of the sapphire substrate. The velocities extracted from the fundamental, diagonal and second order measurement are shown as circles, squares and triangles, respectively. The purple dotted line is based on the Datta and Hunsinger approximation, while the blue dashed line is from a finite element simulation.

of both the nanostructure and substrate, we can also learn about those properties from the dispersion relation. By measuring the frequency changes as a function of SAW wavelength using this phononic crystal, information about the mechanical properties of the nanostructure and substrate can be extracted and related to each other. This offers a new method for surface metrology using picosecond SAWs at ultrashort wavelengths.

3.4 Generating and Selectively Enhancing Higher-frequency SAWs using Pulse Sequences

Besides using a smaller nano-patterned phononic crystal, an attractive approach for generating shorter wavelength SAWs is to modify the impulse that generates the photoacoustic response so that higher order SAWs (shorter wavelength) can be enhanced while the lower orders are suppressed[44]. To control the SAW generation we apply a two-pulse sequence to the sample, matched to the SAW we are trying to generate, as shown in Fig. 3.12. The pump beam is sent into a Michelson interferometer, which uses a 50% beam splitter to generate two pump pulses with a relative delay that can be adjusted by simply moving a translation stage on one arm of the interferometer. To validate this technique, we used the simplest 1D nickel-on-sapphire sample. In this configuration, the second pump pulse induces an additional stress on the Ni-sapphire interface, and a second surface acoustic wave is generated, that will reinforce or reduce the first wave depending on the relative phase. Varying the time delay between the two pump pulses introduces a relative phase shift in the SAW sequences generated.

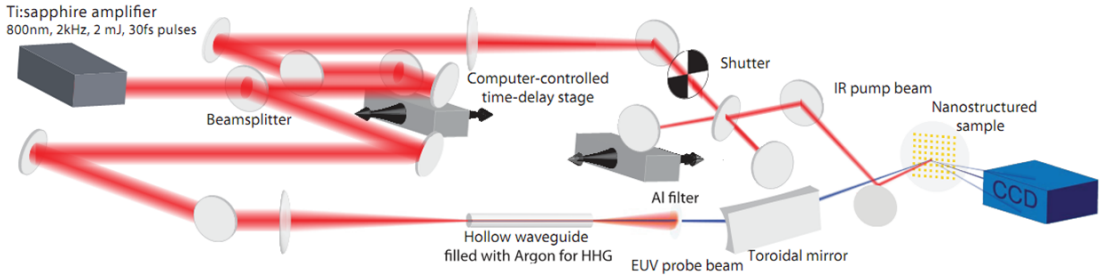

Figure 3.12: Michelson interferometer modification in the experimental setup.

A typical time-resolved SAW signal is shown in the top three curves in Fig. 3.13, where the sample used was a 1D Ni-on-sapphire grating of linewidth $L = 200$nm and $P = 800$nm. The bottom curve in Fig. 3.13 plots the pure acoustic signal after removing the thermal relaxation dynamics.

Fig. 3.14 plots the photoacoustic response from the same grating as in Fig. 3.13, (with the thermal background removed) at different relative delay times Δt between pump pulses. The dynamic signal and the Fourier transform spectrum demonstrates the coherent interference from two SAWs, which can be simply controlled by adjusting the time delay between pulses.

Note that the delay Δt corresponds to a phase shift of $\Delta t/T_1$ for the fundamental SAW, where T_1 is its oscillation period for the fundamental order. For the second order SAW, the phase shift is $\Delta t/T_2$ where T_2 is the period for second order. From the photoacoustic frequency spectrum, the second order SAW period is about half of the fundamental value i.e. $T_2 \approx T_1/2$. From the spectrum of Fig. 3.14, when both pump pulses arrive at the same time, the excited SAWs correspond to the fundamental frequency at $8.12GHz$ (with a period of $T_1 = 123ps$). Higher order frequencies are relatively weaker. For arbitrary relative time delay Δt between the two pump pulses, the total signal S can be described quantitatively as follows:

$$\begin{aligned} S_\omega &= \theta(t) \times [A_1 \exp(-\frac{t}{\tau_1}) \cos(\omega_1 t + \Phi_1) \\ &\quad + A_2 \exp(-\frac{t}{\tau_2}) \cos(\omega_2 t + \Phi_2)] \\ &\quad + \theta(t - \Delta t) \times [A_1 \exp(-\frac{t - \Delta t}{\tau_1}) \cos(\omega_1 (t - \Delta t) + \Phi_1) \\ &\quad + A_2 \exp(-\frac{t - \Delta t}{\tau_2}) \cos(\omega_2 (t - \Delta t) + \Phi_2)] \end{aligned} \tag{3.1}$$

where SAWs are described by a sinusoidal function, $\theta(t)$ is a unit step function, $A_{1,2}$ are the SAW amplitudes for the fundamental and second order, $\tau_{1,2}$ are the damping rates for both frequencies which depend only on the materials, Φ is the initial phase for SAWs, and $\omega_{1,2}$ are the frequencies for both waves. For the case considered here, where Eq. 3.1 can be rearranged after the

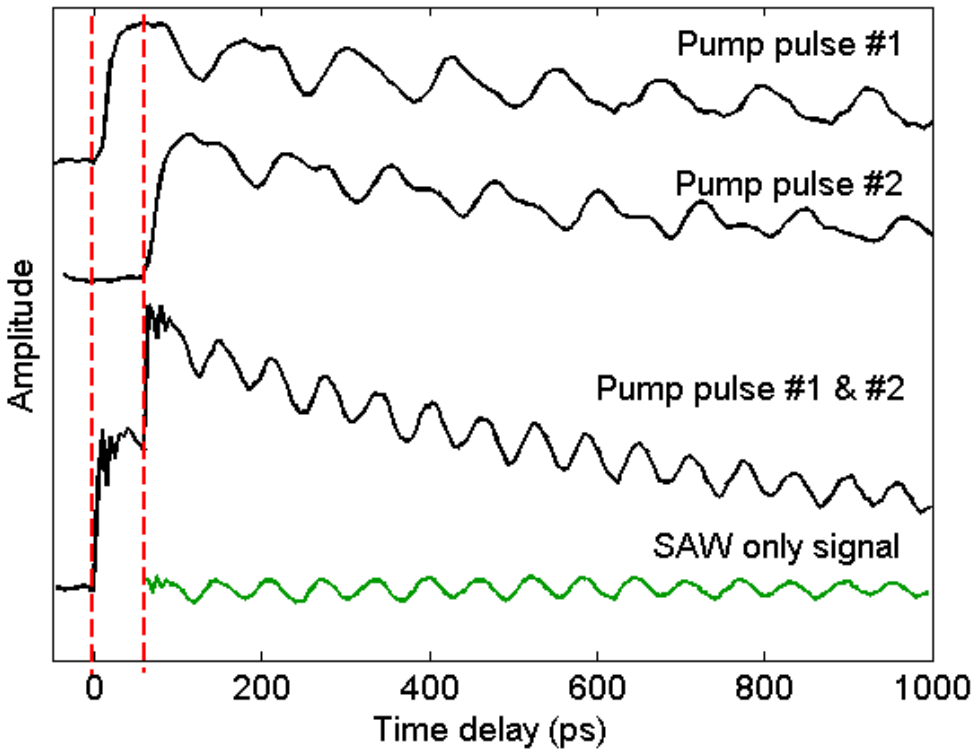

Figure 3.13: Time-resolved SAW signal with a Michelson interferometer on $P = 800$nm 1D Ni-on-sapphire sample (amplitudes of top three curves are normalized and shifted for presentation). Curves from top to bottom are signal with pump pulse 1 only, pump pulse 2 only, and the two-pulse SAW signal before and after removing thermal relaxation dynamics. Delay zero of pump pulse 1 is synchronized with the probe beam and pump pulse 2 is set at a $62ps$ time delay, as indicated by the vertical dashed lines.

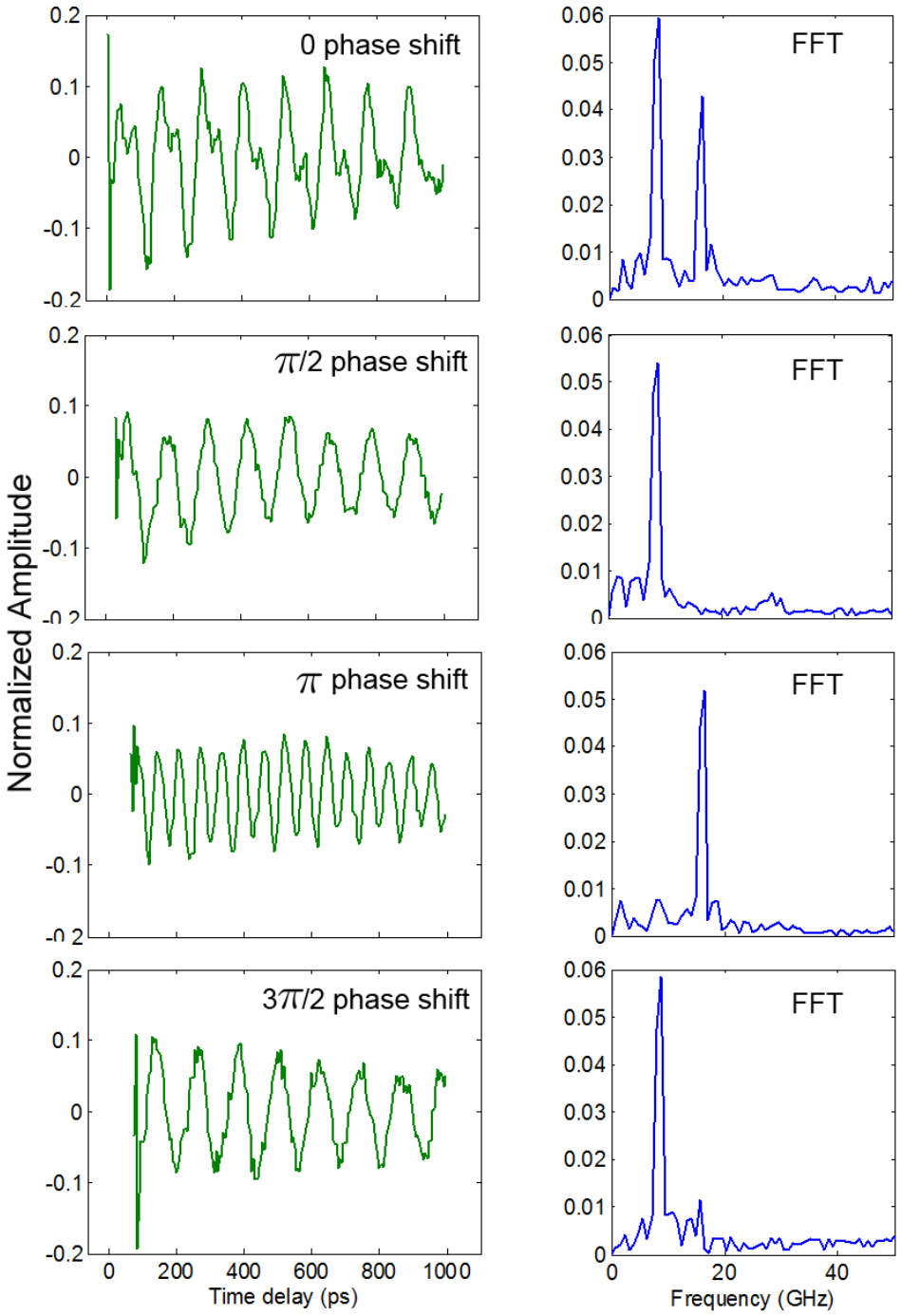

Figure 3.14: Fundamental and second order SAWs generated by two pump beams separated by varied time delays for a 1D nano-grating of 800nm period. Top to bottom: extracted SAWs and frequency spectrum for relative time delays between the pump pulses of 0, $31ps$, $62ps$, $93ps$, corresponding to phase shifts between the fundamental SAWs of 0, $\pi/2$, π, $3\pi/2$. Selective control of SAW generation is demonstrated.

second pump pulse arrives as:

$$\begin{aligned} S_\omega &= A_1 \exp(-\tfrac{t}{\tau_1})[\cos(\omega t + \Phi_1) \\ &+ \exp(\tfrac{\Delta t}{\tau_1}) \cos(\omega(t-\Delta t) + \Phi_1)] \\ &+ A_2 \exp(-\tfrac{t}{\tau_2})[\cos(2\omega t + \Phi_2) \\ &+ \exp(\tfrac{\Delta t}{\tau_2}) \cos(2\omega(t-\Delta t) + \Phi_2)] \end{aligned} \tag{3.2}$$

For a relative delay between the two pump pulses of $\Delta t = T_1/2 = \pi/\omega$, a π phase shift in the fundamental order is introduced by the second acoustic waves, resulting in destructive interference (see Fig. 3.14). Since $T_1/2 \sim T_2$, this delay time corresponds to a 2π phase shift for the second order SAW, resulting in constructive interference. From Eq. 3.2, it is clear that for this delay time the SAW signal can be simplified as:

$$S_{\frac{T}{2}} = A_1 \exp\,(-\frac{t}{\tau_1})[1 - \exp(\frac{\pi}{\omega \times \tau_1})] \cos(\omega t + \Phi_1) + A_2 \exp\,(-\frac{t}{\tau_2})[1 + \exp(\frac{\pi}{\omega \times \tau_2})] \cos(2\omega t + \Phi_2) \tag{3.3}$$

The damping rates τ_1 and τ_2 are relatively long, and thus the exponential decay $\exp(\Delta t/\tau_1) = \exp(\frac{\pi}{\omega\tau_1})$ term is close to 1. The amplitude of the first term in Eq. 3.3, (the fundamental SAW), is close to zero, while the second term (the second-order SAW) is strongly reinforced. For the 800nm period grating, the required relative delay between the two pump pulses to enhance the second order is around $62ps$. However, for time delays of 31 and $93ps$, the fundamental frequency is enhanced while the second order SAWs interfere destructively.

The same approach also works for smaller 1D nano-gratings (sample I). Fig. 3.15 shows similar control on $P = 400$nm grating, with delay time 0, 15, 30 and $45ps$ represents phase shifts of 0, $\pi/2$, π, and $3\pi/2$. In the frequency spectrum, clear enhancement of second order frequency is in the third line curves while totally depressed the second order at second and fourth from top curves.

And for the smallest 1D nickel-on-sapphire sample, at $P = 260$nm grating, the response as a function of pump-probe delay time for phase shifts of 0 and π between the two pump pulses are shown in Fig. 3.16. Comparing the results from 0 and π phase shifts between the two pump pulses,

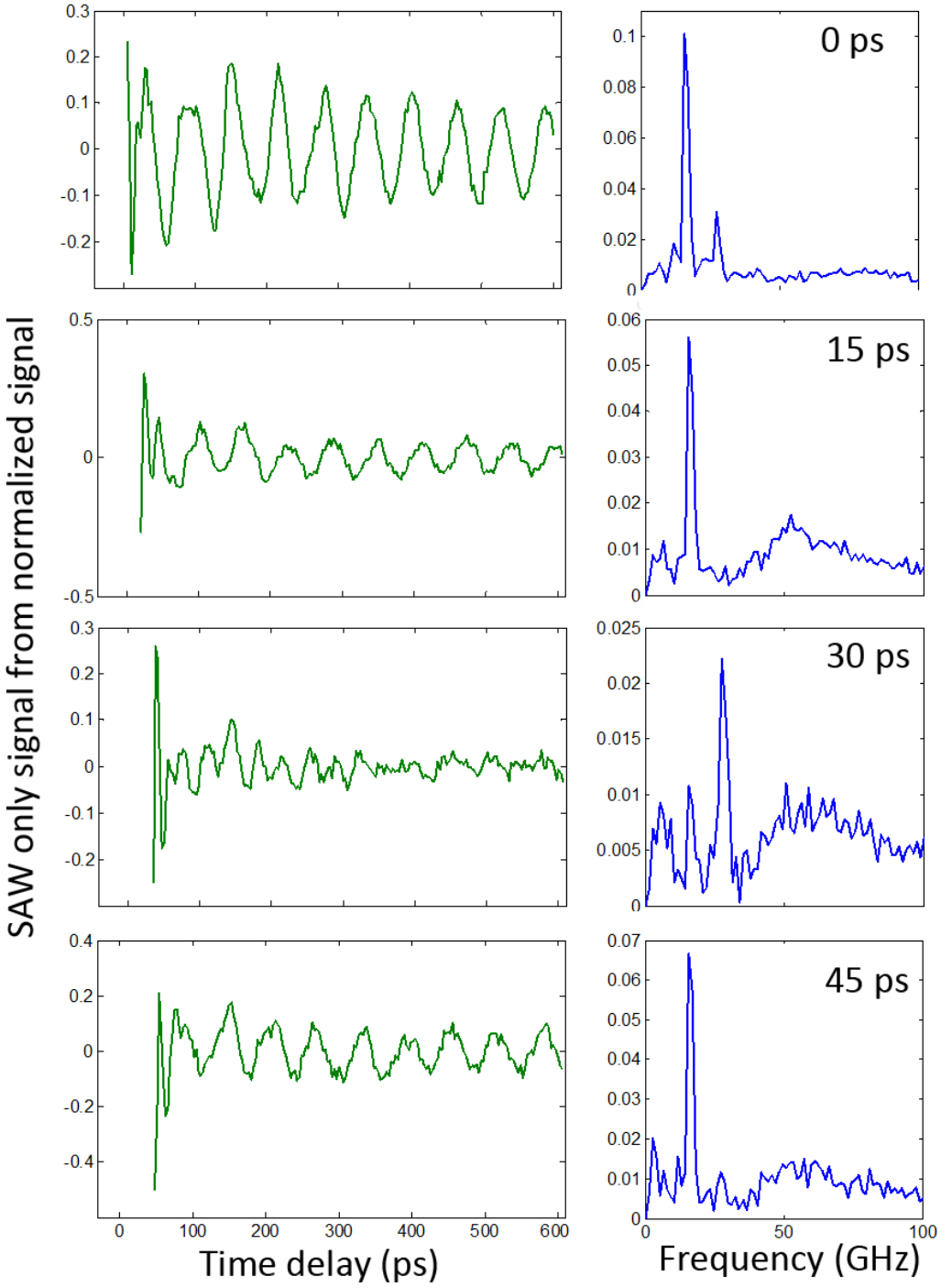

Figure 3.15: Left are the time-resolved SAW-only signal at $L = 100$nm, $P = 400$nm gratings at different pump-pump delay times, while right shows the FFT spectrum, indicating the enhancement of second order SAWs at $30ps$ relative delay time, corresponding to a pi phase delay.

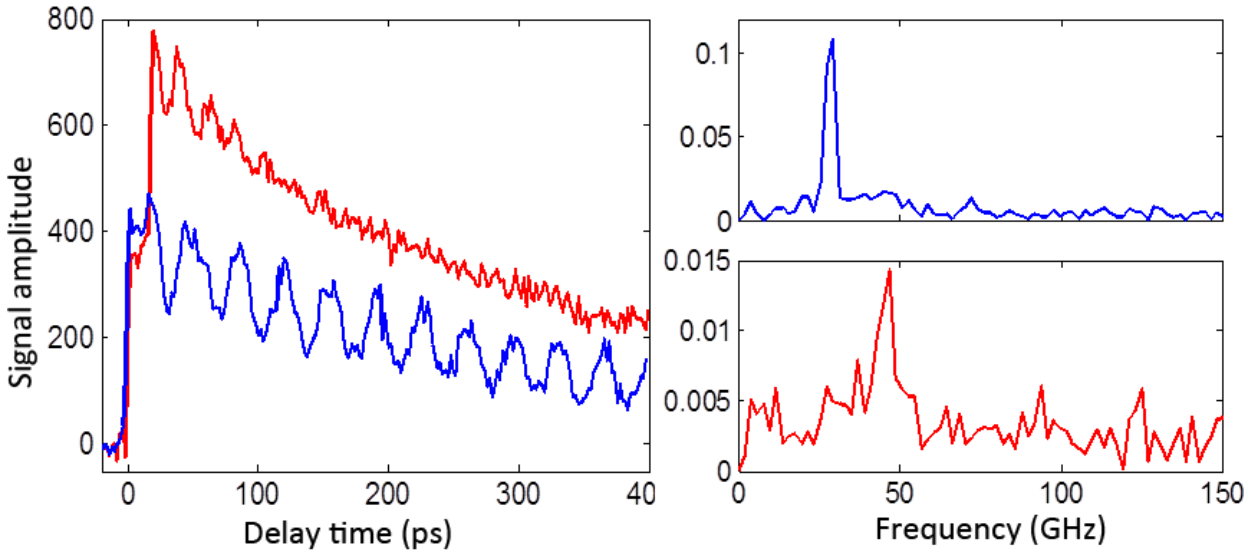

Figure 3.16: An alternative way to demonstrate the double pump pulses - controlling SAW generation in a $P = 260$nm nano-grating for one pump only (left blue curve) and two pump pulses together at π (left red curve) phase differences between the two pump pulses. Frequency spectra on the right side is FFT of two curves from the left side with color matched. Comparing these two spectrum, it is clear that the enhancement of second order with suppression of fundamental order SAWs at two pumps with π phase difference.

the Fourier transforms clearly demonstrate that the fundamental order dominates in Fig. 3.16 middle left with no visible second order frequency in the spectrum, while the second order is enhanced in Fig. 3.16 middle right.

Eq.3.2 can also be used to implement curve fitting to the SAW signal for these two cases to provide more information about the frequency and the damping rate of SAWs at different excitation orders. At 0 phase shift, the curve fitting results in oscillation frequencies of $\omega_1 = 28.44 \pm 0.04$ GHz and $\omega_2 = 47.92 \pm 0.58$ GHz, with damping times of $\tau_1 = 756.27 \pm 141$ ps and $\tau_2 = 59.43 \pm 13.6$ ps. For the π phase shift case, $\omega_2 = 45.55 \pm 0.52$ GHz and $\tau_2 = 58.34 \pm 11$ ps. Comparing these numbers, the consistent values of ω_2 and τ_2 shows in a quantitative way that the same second-order SAW is preserved and reinforced even as the fundamental order is suppressed.

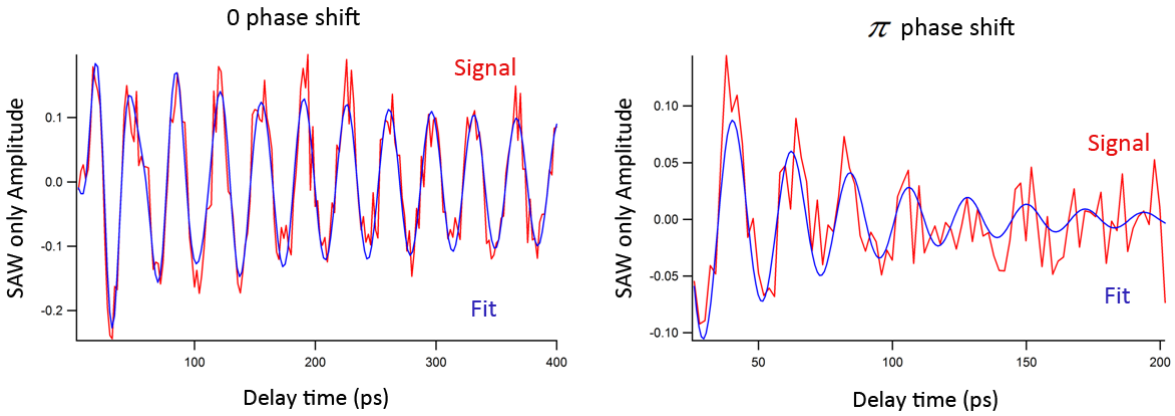

Figure 3.17: Curve fitting for SAW only signal (after thermal background removed) to obtain the frequency for 1st and 2nd order, as well as damping rate for both excitation orders. In this case, we obtain the fundamental frequency is 28.44GHz, and second order at 47.92GHz, while the damping rate is 756 ps for first order and 59ps for second order.

Although a similar Michelson interferometer setup has been used in previous photoacoustic experiments which used visible light to pump and probe the SAWs, due to the lower signal-to-noise ratio of the transient optical signal, it has not been possible to observe the selective enhancement of the second order SAW until now[44]. The sensitivity of the short wavelength EUV probe allows us to observe this control for the first time, allowing the wavelength and penetration depth of the SAW to be reduced by a factor of two for a fixed nano-patterned phononic crystal. The same approach

can be extended in 2D phononic crystals and higher SAW frequencies. Rather than two pump pulses, a pulse train can also be designed to allow even more precise control over the generation and propagation of SAWs.

Thus in this experiment, we use pulse sequences of pump beams together with the 1D nanopatterned gratings to control the generation of nano-SAWs. This allows us to preferentially enhance higher-order SAWs while suppressing lower frequency waves, and to reduce the generated SAW wavelength by a factor of two for a defined nanostructure period.

3.5 Additional Experiments

3.5.1 Non-contact Approach in Generating Shorter Wavelength SAWs

Sub-optical phononic crystals are essential in generating SAWs with wavelength shorter than the illumination laser wavelength. It is not difficult to use it in research laboratories in order to study the fundamental physics. Also due to the high sensitivity in nano-system and surfaces, it is possible to use this nano-patterned technique in photoacoutic metrology - we will discuss one of the applications in next chapter. However, in order to extend this approach to more general application situations, it is important to bare the non-contact and non-destructive properties from photoacoustic wave itself, and develop approaches that do not require patterning for a broad range of applications, such as in industrial-level thin film metrology, surface inspection and so on.

One important approach is to improve the transient grating technique to generate shorter wavelength SAWs. As shown in Fig. 3.18 shows the geometry of transient grating experiment, where SAW generated from transient grating experiment has the wavelength given by $\Lambda = \lambda/NA$, where λ is the wavelength of incoming laser pulse, and NA is the numerical aperture of the two laser beams ($NA = n \cdot \sin\theta$). Thermally exciting the film using a visible light interference pattern in a transient grating geometry is limited to SAW wavelengths in the range of optical wavelengths. As a result, our group previously achieved the shortest acoustic wavelength generated using the transient grating method corresponding to 750nm using 400nm laser beams (second harmonic from

800nm laser amplifier).

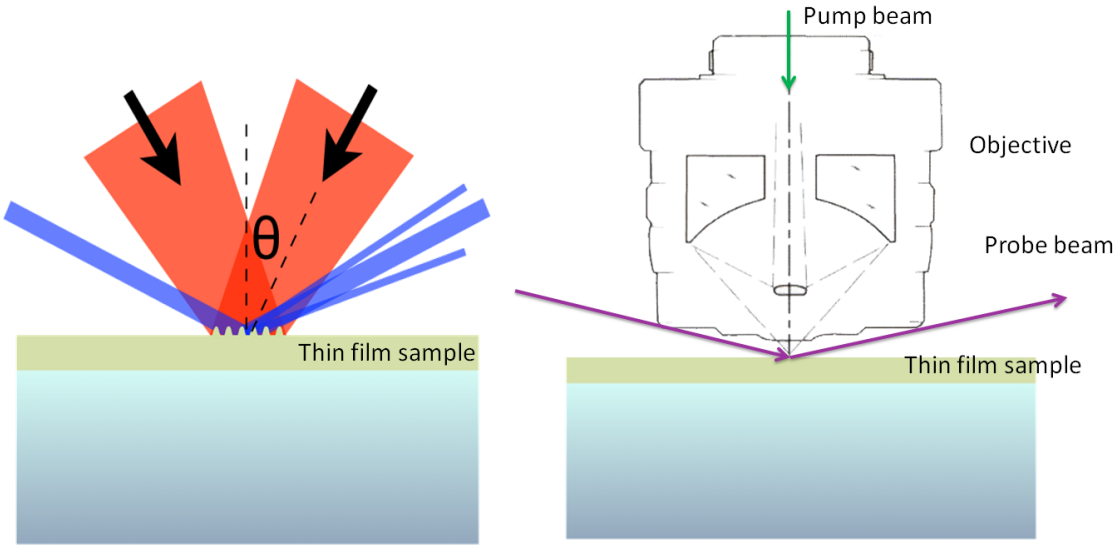

Figure 3.18: Geometry for transient grating experiment. (Left) Normal lens and transmission amplitude mask are normally used in generating interference pattern on thin films, using a high-NA lens and shorter wavelength illumination laser beams can decrease the wavelength of generated SAWs. However, high-NA objective (right) has very small depth of focus which make the detection extremely difficult.

I have made a few more attempts to improve the SAW wavelength generated from transient grating including (1) decrease the illumination wavelength and increase the numerical aperture. In previous experiment from our group, a normal convex-convex lens is used, which limit the NA to less than 0.3. In order to improve from this aspect, we bought a high-NA reflective objective lens, which gives a NA up to 0.65 instead of normal lens set to focusing two pump pulses, as shown in Fig. 3.18(left). It is expected to generate SAWs wavelength below 500nm. However, I failed to detect the photoacoustic waves because the depth of focus is so tight while the objective is too big for reflection detection of photoacoustic dynamics, as shown in Fig. 3.18(right). One possible solution is to design a ultra thin film with the substrate transparent to the illumination wavelength, thus we can generate transient grating at the interfaces and detect it from the back side of the thin film. Also, at this wavelength, low flux high harmonic generation beams are not suitable for detection, because the wavelength is still in visible range, while EUV needs to operate

in vacuum environment, making the experiment more complicate.

We also tried to focus fourth harmonic beams from IR light on the thin film sample to decrease the wavelength of incoming beams, but after two harmonic crystal, the power drops to a level makes it difficult to generate strong enough signals. With the upgrade of our amplifier system (upgrade from 2kHz, 1.8mJ to 3kHz, 2.3mJ), it could be easier to achieve fourth harmonic now.

In addition, we can also use pulse sequences to generate SAWs without physical contact. Focusing a laser beam on a material can generate broadband SAWs which propagate in all different directions along surface. In our section 4, two pulse sequences together with the nanoscale phononic crystal are used to control and enhance the different band of SAW excitation with the present of nano-gratings.

An alternative method is to remove the nano-structure but apply multiple sequences of pulses to generate narrowband SAWs[31]. This will allow no additional pattern on samples to generate short SAWs, but a precise control of pulse generation and separation are needed to narrow the bandwidth, and ensure the propagation without significant damping of SAWs along surface.

3.5.2 Short Delay Time Signal: Longitudinal Acoustic Waves

Both surface acoustic waves, and longitudinal photoacoustic waves are of great importance for both understanding of fundamental physics and practical applications. The previous three sections are focused on the excitation and observation of surface acoustic waves mainly because it is still difficult to generate SAWs in short wavelength, despite great demand on it. On the other hand, longitudinal waves have attracted significant attention for several decades, and have been successfully generated and detected at high frequency in both research laboratory and industrial applications[45]. Pushing the wavelength of longitudinal waves at extremely short wavelength and applying these nano-LAWs to study nano-system together with SAWs is important direction for photoacoustic metrology, which will be discussed in detail in next chapter.

Nano-SAWs are generated when our phononic crystal sample is impulsively heated by a pump pulse. During this excitation, a longitudinal acoustic wave is generated with wavelength down to a

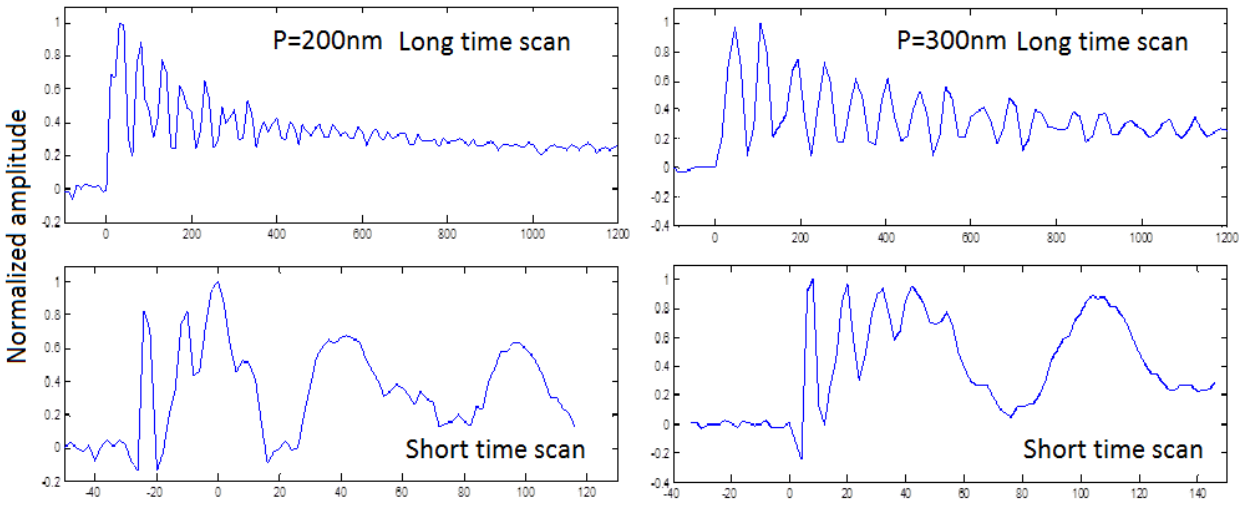

Figure 3.19: Two sets of dynamic scans at P=200 and P=300 nm sample of Co/Pd multilayers on silicon substrate. Long time scans shows different frequency, corresponding to the period of 2D arrays, while the short-time scan frequencies are consistent because they are induced within the nanostructures.

few nanometers. Fig. 3.19 shows the long and short pump-probe delay time signal for a sample of Co/Pd multilayer array patterned the top of the silicon substrate at $L = 80$nm, $P = 200$nm (top) and $L = 180$nm and $P = 300$nm (bottom) samples. Clearly, the longer delay time shows a different oscillation frequency, which depends on the period of the arrays, while the short time oscillation is very close together because this narrow band longitudinal wave is generated as a result of the reflection at the interface of multilayer stack with the substrate. This frequency corresponds to twice the thickness of the multilayer structure. Thus from the measurement of longitudinal wave frequency, it is possible to determine the longitudinal velocity of an unknown sample.

3.6 Conclusions

Another future direction for improving this photoacoustic metrology is to improve the signal-to-noise ratio for small gratings, where measurements usually noisier because the diffraction angle is too big for the CCD camera to capture the diffracted beams. This can be improved by switching the noble gas from Argon to Helium to generate even shorter wavelength EUV beams. Another way is to redesign the setup to make it capable of varying the angle of incidence of the light, which would require also the ability to move the CCD detector.

A shorter grating period can be generated by using EUV transient grating technique. The recent development of high-energy HHG in our group make it possible to generate EUV at short wavelength and high flux, which can be used to generate short wavelength SAWs from transient grating experiment. Then it can combine the advantage of non-contact, non-destructive of transient grating with short wavelength SAW generation to measure ultra thin film properties.

In conclusion, we demonstrated two approaches for generating shorter wavelength surface acoustic waves in nano-patterned phononic crystals. First, using smaller 2D nano-patterned features with periodicity as short as 35 nm, we generated and probed the shortest wavelength SAWs to date using EUV photoacoustic metrology. These correspond to SAWs with penetration depths of only ~ 10nm, leading to large deviations in the acoustic dispersion from that of the substrate. In the 2D sample geometry, diagonal and second order waves were also observed. Second, we used two-pulse

sequences to selectively enhance either the fundamental or second order SAWs by controlling the relative delay between pump pulses. This allows us to generate even shorter-wavelength SAWs in an existing nano-patterned phononic crystal sample. Combining these two techniques would result in even shorter SAW wavelength generation and control, and therefore a smaller penetration depth enabling sensitive nano-characterization of ultrathin films and nanostructured interfaces.

Chapter 4

Photoacoustic Metrology of Thin Films

4.1 Introduction

Thin film technology is widely employed in a variety of fields, from biotechnology to aerospace, to realize, for example, conducting and dielectric elements in microelectronic devices, or reflecting elements in optics. It has developed extremely quickly in the past few decades with the developments of nanotechnology. Many approaches have been implemented to characterize thin film performances. Conventional spectroscopic and scanning techniques usually measure the chemical and electrical properties of thin films, but are unable to measure their mechanical properties. Brillouin scattering was used to measure both longitudinal and transverse acoustic waves, but the interpretation remains indirect and rather complex, and the intensity of scattered light is very weak and strongly depends on the accuracy of the attenuation measurement[46]. In this scenario, photoacoustics provides an effective alternative way to measure the elastic modulus of thin films since it directly probes the system's elastic properties.

As introduced in Chap. 2, acoustic waves provide essential information about density, elastic properties, and thin film thickness if we monitor the dynamics of acoustic propagation. A number of metrology methods based on photoacoustic generation have been performed to measure thin films. Longitudinal waves can be launched in transparent dielectric[45] with absorption layer or opaque metal films[47] with a pulsed laser in order to measure their Young's modulus. However this method only measures the longitudinal acoustic velocity and calculates the modulus based on an assumption of Poisson's ratio, which may vary as the material changes to nanoscale[48]. A

mechanical approach using an AFM tip to generate nanoscale acoustic waves is used to measure elastic properties[46], but the delicate procedure and strong influence from the substrate make it difficult to repeat.

In this chapter, we use the same technique discussed in Chap. 3 to launch nano- SAWs and LAWs simultaneously. By measuring their frequencies and velocities, both the thin film's Young's modulus and and Poisson's ratio can be obtained.

4.2 Theoretical Calculation of the Elastic Tensor

The last two chapters give an introduction of photoacoustic waves as low-frequency mode of lattice vibration, and focus mainly on the experimental achievement of generating and detecting short-wavelength SAWs, and only discuss the macroscopic relations, the dispersion, the propagation velocity and the frequency. However, in order to build a metrology technique, it is necessary to understand the theoretical relation between photoacoustic waves and the mechanical properties in a microscopic view.

Let's consider the material deformation as displacements from the equilibrium positions of all the atoms. In a rigid rotation and translation situation, when an atom has a displacement $\vec{u}$ that moves it from position $\vec{L}$ to $\vec{L}'$, the deformation Δ can be expressed as

$$\Delta(\vec{L},t) = dL' - dL = 2S_{ij}(\vec{L},t)dL_i dL_j, \tag{4.1}$$

with

$$S_{ij}(\vec{L},t) = \frac{1}{2}\left(\frac{\partial u_i}{\partial L_j} + \frac{\partial u_j}{\partial L_i} + \frac{\partial u_k}{\partial L_i}\frac{\partial u_k}{\partial L_j}\right) \tag{4.2}$$

$$= \begin{bmatrix} S_{xx} & S_{xy} & S_{xz} \\ S_{yx} & S_{yy} & S_{yz} \\ S_{zx} & S_{zy} & S_{zz} \end{bmatrix}, \tag{4.3}$$

where $i,j,k = x,y,z$. This S matrix is the strain field that describes the deformation in terms of particle displacement. With small displacements, the quadratic term $\frac{\partial u_k}{\partial L_i}\frac{\partial u_k}{\partial L_j}$ in Eq. 4.2 is negligible

and this matrix will only have linear terms in $\partial u/\partial L$. Therefore, the different directions of lattice vibration can be expressed in the strain matrix (Eq. 4.3). In the case of shear strains, S matrix corresponds to $S_{ij} = constant$ while $S_{ii} = 0$.

When a crystal lattice vibrates, the elastic restoring force (or stress) develops between neighboring atoms. When the distortion is small, Hooke's law states that the strain is linearly proportional to the stress, which can be rewritten in terms of strain (S) and stress tensor (T) as

$$T_{ij} = c_{ijkl} S_{kl}, \tag{4.4}$$

where $i, j, k, l = x, y, z$. Since both stress and strain are 3×3 tensor, this $3 \times 3 \times 3 \times 3$ "microscopic spring constant" tensor c_{ijkl} represents the elastic stiffness constant, also called the elastic tensor.

Fortunately, symmetry of crystal lattice and transform invariance may reduce the 81 elements of elastic stiffness constant to a smaller matrix as

$$c = \begin{bmatrix} c_{11} & c_{12} & c_{13} & c_{14} & c_{15} & c_{16} \\ c_{21} & c_{22} & c_{23} & c_{24} & c_{25} & c_{26} \\ c_{31} & c_{32} & c_{33} & c_{34} & c_{35} & c_{36} \\ c_{41} & c_{42} & c_{43} & c_{44} & c_{45} & c_{46} \\ c_{51} & c_{52} & c_{53} & c_{54} & c_{55} & c_{56} \\ c_{61} & c_{62} & c_{63} & c_{64} & c_{65} & c_{66} \end{bmatrix} \tag{4.5}$$

where $1 = xx$, $2 = yy$, $3 = zz$, $4 = yz, zy$, $5 = xz, zx$, $6 = xy, yx$. Thus $c_{pq} = c_{ijkl}$, where $p, q = 1, 2, 3$, $i, j, k, l = x, y, z$. Similarly $T_p = T_{ij}$ and $S_q = T_{kl}$. With some additional symmetry, for example in cubic crystals, this elastic tensor can be further reduced with $c_{11} = c_{22} = c_{33}$ referring to the bulk response, and $c_{44} = c_{55} = c_{66}$ corresponding to the shear effect.

If combining this elastic tensor with a lossless acoustic field equation[27]

$$\nabla \cdot T = \rho \frac{\partial v}{\partial t} - \vec{F} \tag{4.6}$$

where ρ is the density, and F is external force, so $\vec{F} = 0$ when there is no external force.

With the isotropic condition and a cubic crystal lattice, $c_{12} = c_{11} - 2c_{44}$. Thus the wave equation becomes

$$k^2 \begin{bmatrix} c_{44} & 0 & 0 \\ 0 & c_{44} & 0 \\ 0 & 0 & c_{11} \end{bmatrix} \begin{bmatrix} v_x \\ v_y \\ v_z \end{bmatrix} = \rho\omega^2 \begin{bmatrix} v_x \\ v_y \\ v_z \end{bmatrix} \tag{4.7}$$

Thus the shear wave solution gives $k^2 c_{44} = \rho\omega^2$. Combining with the definition of shear (transverse) velocity $v_s = w/k$, we have

$$c_{44} = \rho v_T^2, \tag{4.8}$$

Similarly, for the longitudinal direction, we have

$$c_{11} = \rho v_L^2. \tag{4.9}$$

where v_L is the longitudinal wave velocity. Similarly, transverse velocity can be derived from elastic tensor.

In macroscopic view, the elastic properties of materials are usually indicated by Young's modulus and Poisson's ratio. Young's modulus E describes the stiffness of a material and is defined by

$$E = \frac{T_3}{S_3} = c_{44}(\frac{3c_{11} - 4c_{44}}{c_{11} - c44}). \tag{4.10}$$

where relation of T and S come from Eq. 4.4. While Poisson's ratio ν describes the ratio of the size change in the direction perpendicular to the applied force versus the expanded length in the direction of the force. In an isotropic solid case,

$$\nu = -\frac{S_1}{S_3} = -\frac{S_2}{S_3} = \frac{c_{11} - 2c_{44}}{2(c_{11} - c_{44})}. \tag{4.11}$$

Experiments can measure the velocity of acoustic waves in different directions inside the film, which gives the relation of the stress and strain, i.e. the elastic tensor. Consequently, we can derive the Young's modulus and Poisson's ratio.

4.3 Sample and Dynamic Scans

4.3.1 Sample Design

For this experiment, we use thin film samples provided by our industrial collaborator. They are 100nm-thick amorphous hydrogenated silicon carbide (α-SiC:H) film with different doping ratios, and thus different mechanical properties and densities. In order to not only characterize 100nm thick films for now, but also build a metrology technique that can be extended to sub-10nm thicknesses, we adopted the technique from Chap. 3. A sub-optical metal grating is patterned on top of our thin film sample to launch photoacoustic waves. We patterned two film samples with 1D nickel stripes of 10 nm high, and for each film sample we fabricated five different grating sizes at 50, 100, 200, 350 and 500nm, with a fixed duty cycle so that the grating period $P = 3L$. We also include a reference set of samples of 20nm-high 1D nickel grating on bare silicon substrates, and linewidth L ranging from 60 to 1000nm, and $P = 4L$. This sample is very similar to the sample used in the previous SAW experiment. Schematic picture of the three samples is shown in Fig. 4.1.

The feature sizes of the samples have been confirmed using AFM (picture not shown here) for height and SEM for lateral size, as shown on right side of Fig. 4.1. The lateral period of these samples are measured at $P_{measured} = 1527$nm, 1090nm, 600nm, 305nm, 156nm, but I will still refer to the nominal value in this chapter since the error is very small. The calculation and analysis will use the measured values.

Thickness for these films is measured using ellipsometry by our collaborator, and with a commercial tool, the Young's modulus is measured roughly at 30GPa for the first nano-patterned sample (referred as sample I) and 200GPa for the second thin film sample (sample II).

4.3.2 Experimental Setup

The experimental setup is similar to the one outlined in the previous chapter: an ultrafast 800nm laser pulse is used to impulsively heat nano gratings and launch photoacoustic waves, while

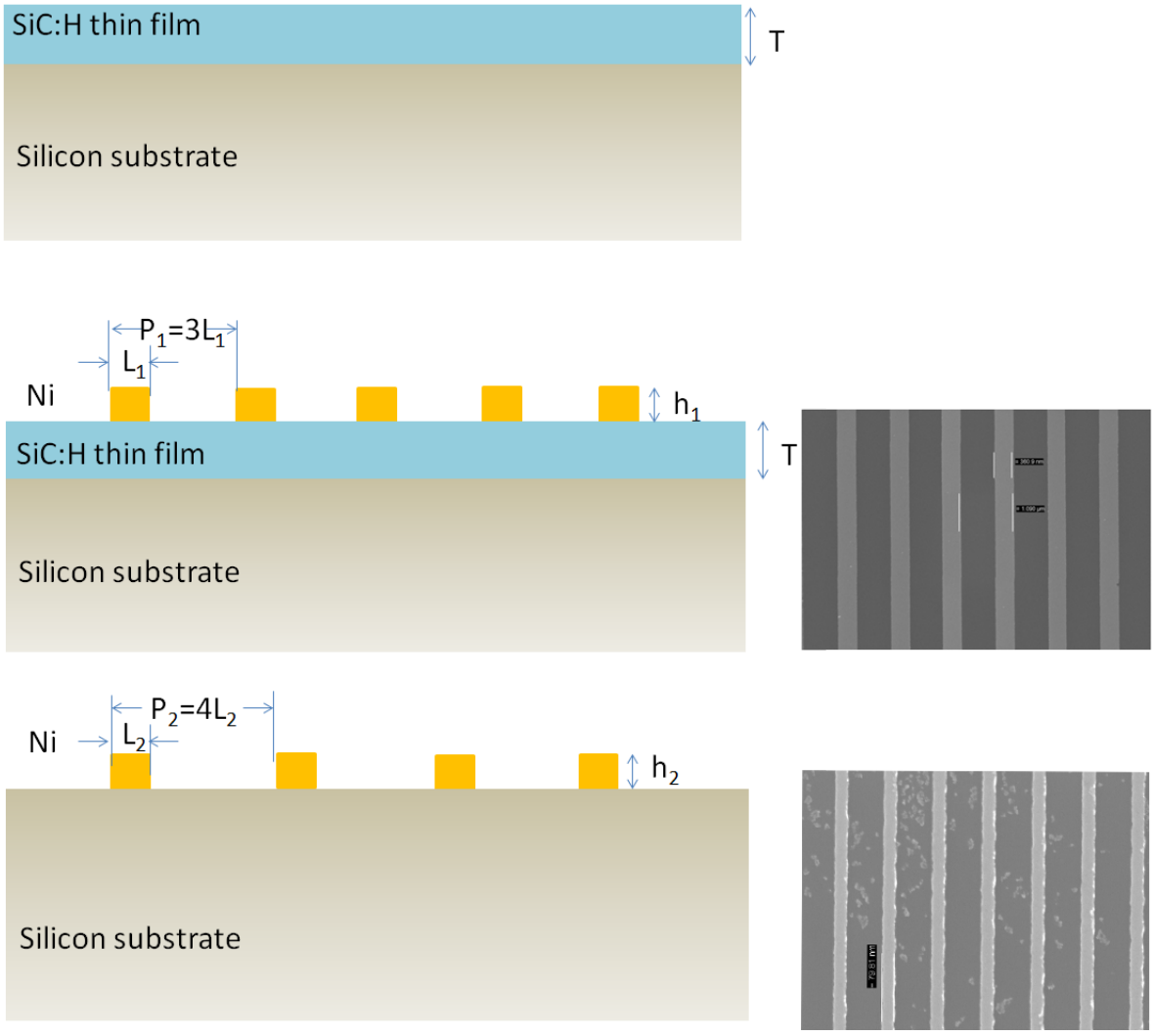

Figure 4.1: Schematic illustration of sample geometries: (top) original thin film sample: 100nm-thick α-SiC:H thin film on top of silicon substrate provided by our industry collaborator; (middle left) nanopatterned thin film sample: 1D nanoscale nickel stripes patterned on α-SiC:H thin film deposited on silicon substrate; (bottom left) reference sample: 1D nickel nano-grating on top of silicon substrate. For all three cases, labels L, P, h and T represent grating width, period, height, and thin film thickness, respectively. Size in the picture is not to scale. Right sides shows the SEM images of samples on left.

a coherent 30nm EUV pulse detects the surface modulation. Fig. 4.2 shows the pump-and-probe geometry on the sample, which generate SAWs and LAWs simultaneously. Since the grating height is 10nm for nano-patterned thin film sample with film 100nm thick, the frequency of longitudinal waves is relatively high. To capture these fast dynamics, the setup is slightly modified to have a better time resolution. We took out one of the retro-reflection mirror in the translation stage, and scan the time step of translation stage at 0.1ps when necessary. Also since all of the samples are using silicon substrate, front-side illumination geometry is used in this experiment.

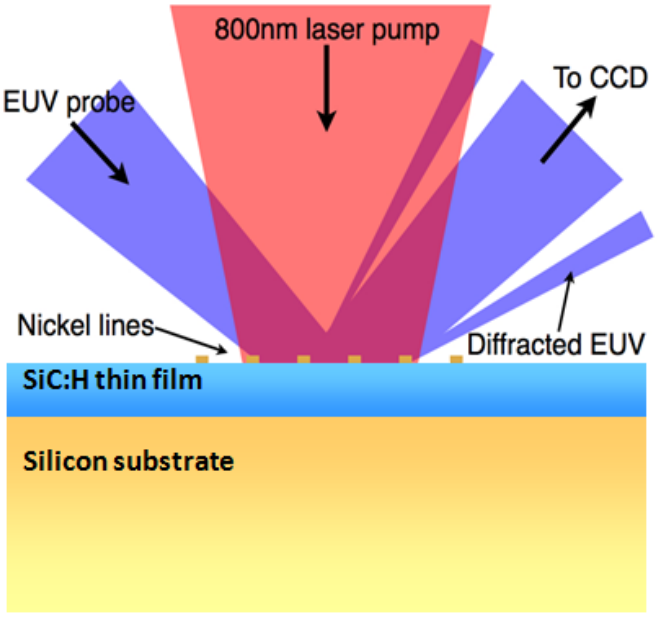

Figure 4.2: Experimental setup for photoacoustic metrology on nano-patterned thin film sample. Front-side illumination is applied due to silicon substrate's opacity.

4.3.3 Time-resolved Signal

In this pump and probe experiment, the pump laser pulse causes a sudden thermal expansion of the metallic nanostructures, which induces a stress at the nanostructure/substrate interface and launches transverse and longitudinal acoustic waves. Longitudinal waves travel into the thin film's depth while transverse waves, surface waves in this particular case, travel along the surface.

Fig. 4.3 shows the transient change of EUV diffraction signal as a function of pump-and-probe

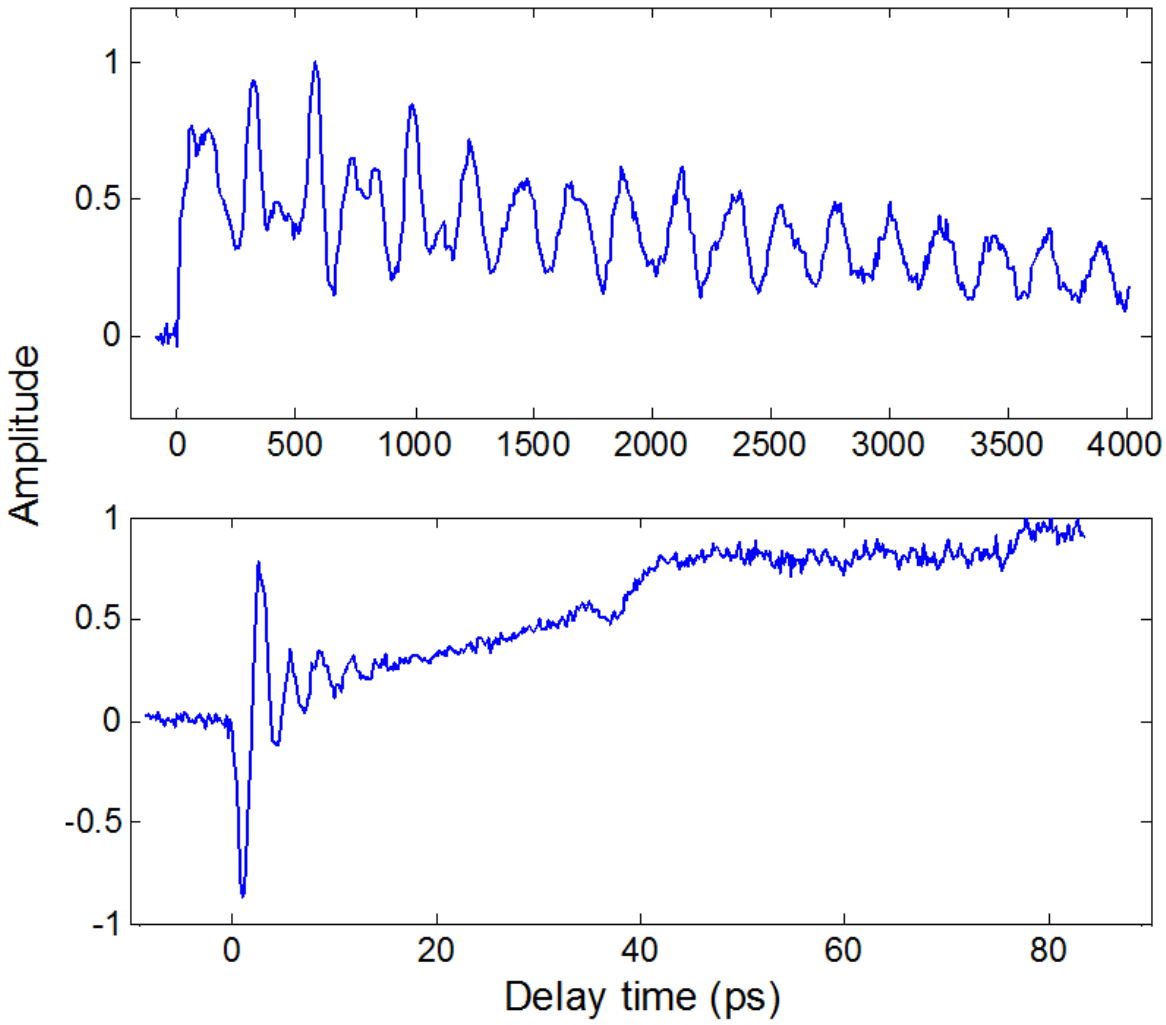

Figure 4.3: Time-resolved EUV signal as a function of pump-probe time delay, in the case of a 100nm thick film with a 1050nm period overlaid nickel grating. The long time scale curve (top) shows surface acoustic waves, while the short time scale result (bottom) reveals both the longitudinal acoustic oscillation inside the 10nm thick nano-grating and the longitudinal wave echo from the underlying 100nm film.

delay time on the 100nm-thick film sample with a 1050nm period overlaid nickel grating. The top figure shows the dynamics in time scale up to 4ns while the bottom curve is signal around zero delay time with finer time resolution. Different dynamic behaviors in the signal outline different photoacoustic modes: at the short time scale, a fast oscillation around zero delay time results from longitudinal acoustic wave traveling within the 10nm nanostructures; shortly after that, an echo signal around 38ps delay time is due to the longitudinal wave propagating in the film and being reflected at the film/substrate interface, thus returning on the surface; finally, the slower oscillations in the longer time scale corresponds to surface acoustic waves whose acoustic wavelength is set by the grating period, and whose penetration depth is only a fraction of this wavelength. Besides these, the rapid rising part around time zero is from thermal expansion of the sample, and the subsequent slow decay is due to thermal dissipation from the nanostructure through thin film to the bulk substrate, which is discussed in Chap. 5.

4.4 Analysis of Data

4.4.1 Measurement of Longitudinal Acoustic Waves

Surface and longitudinal acoustic waves are isolated in both travel directions and time scales, which enable us to analyze them independently. So here we discuss the short delay time signal first.

Fig. 4.4 shows dynamic signal at short time scales for different grating periods on nanopatterned thin film sample (I). It's clear that there are similar fast oscillations within the first 20ps and an echo signal around 38ps for all nanopatterned thin film samples. The fast oscillation corresponds to the nickel stripe height while the echo represents LAW traveling in the 100nm film.

Here we take short time scan on $P = 1050$nm sample as an example to show how we analyze these data. Re-plot the second curve of Fig. 4.4, and we can remove the rising signal by performing a curve fitting using simplified single exponential function; then for the oscillation part, we use a sinusoidal wave with exponential damping to fit the curve:

$$f(x) = -A \cdot \sin\left[2\pi f_{LAW} \cdot (x - x_0)\right] \cdot \exp\left(-\frac{x - x_0}{\tau}\right) + C \tag{4.12}$$

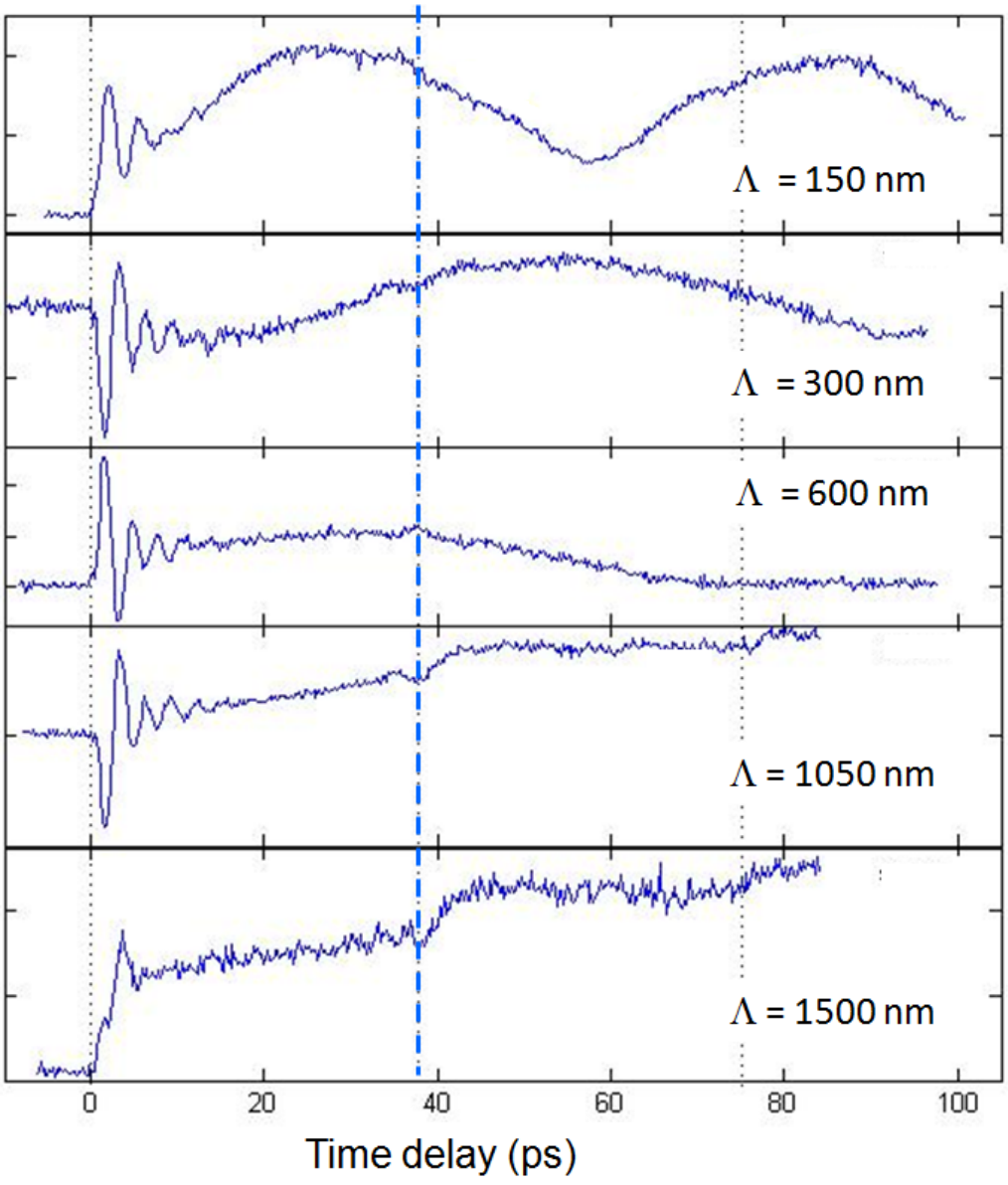

Figure 4.4: Time-resolved dynamics in the first 100ps delay time for five different grating sizes on the nano-patterned thin film sample (I). Fast oscillation corresponds to longitudinal acoustics wave within nanostructures, and the echo signal around 38ps and 75ps is due to the partial reflection of LAW at the film/substrate interface.

where the fitting parameter f_{LAW} is the frequency for the fast longitudinal oscillation, and τ is the damping time. Fig. 4.5 shows the steps we take to analyze short time scans: solid blue line represents the original scan, green curve is acoustic-only signal after removing the thermal expansion (red dotted line for the thermal fitting), and dashed red lines demonstrate the fast damped oscillations. The parameter from oscillation curve fitting results in a frequency of 330 ± 6GHz, and a damping time of 3ps. Also the echo signal is easier to see from the acoustic-only signal (green curve in Fig. 4.5), and the delay time is around 38ps.

Knowledge of the height of nickel stripes (10nm) and the thickness of the thin film (100nm) allows us to determine the LAW speed for both nickel nanostructure and film as:

$$v_{LAW-Ni} = 2h \cdot f_{LAW} = 2 \times 10nm \times 330GHz = 6596m/s, \tag{4.13}$$

$$v_{LAW-film} = 2 \times 100nm/38ps = 5263m/s. \tag{4.14}$$

These measured values have relatively large uncertainty because fast damping dynamics limits the total oscillation time scale, and therefore limits the frequency resolution. This measured LAW velocity in nickel is consistent with values from other references. Velocity of LAWs in thin film depends on the mechanical property and density of the thin film.

In theory, the same calculation for velocity can be applied for the other two samples. However for the second nano-patterned thin film sample, no echo was measured after many attempts. It can be explained by a thin film having a mechanical modulus very close to the substrate that the acoustic impedance is very small at the interface, and this will be discussed later in this chapter. And for the reference nickel-on-silicon sample, the short time scan also shows a weak and fast damping oscillation within 20ps for all different grating size, but no echo signal afterward since there is no thin film underneath nano-gratings, as shown in Fig. 4.6. The damping oscillation fitting function is applied and the frequency obtained is around 150GHz with about 20% uncertainty.

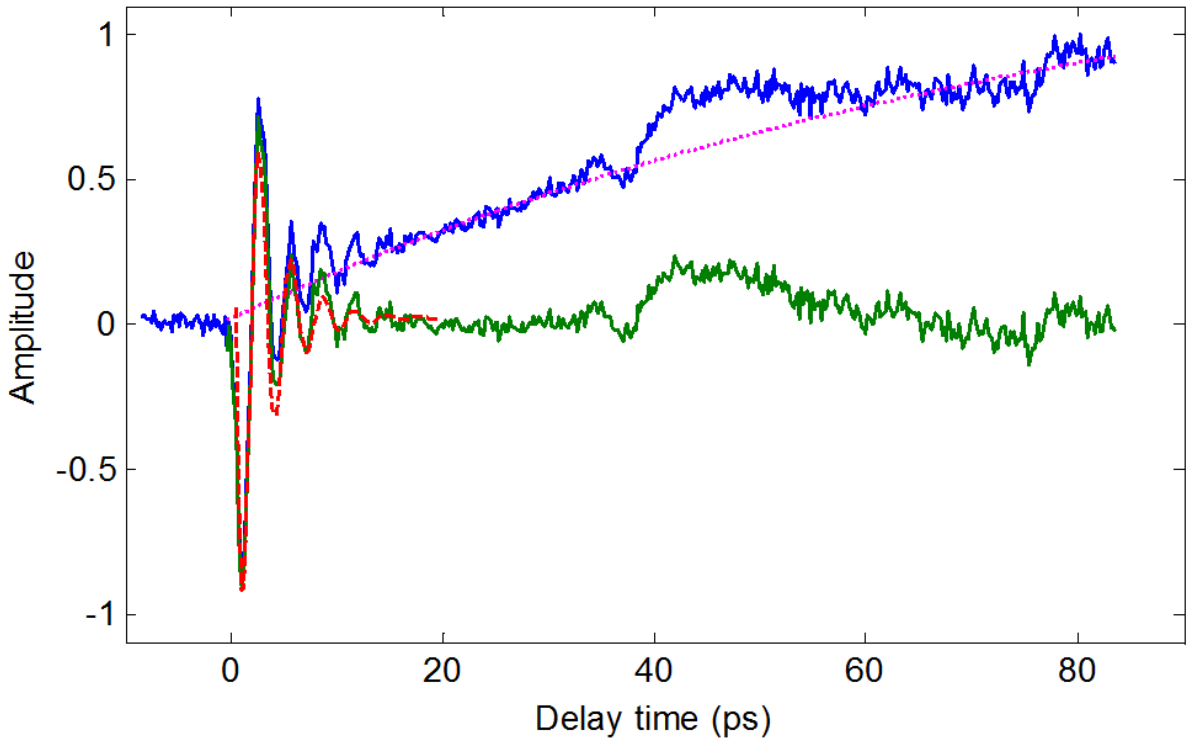

Figure 4.5: Precise characterization of the longitudinal frequency at short delay-time signal, on the example of $L = 350$nm nano-patterned thin-film sample (I). The rising part is subtracted from original time-resolved scan signal (blue curve) using an exponential curve fitting (pink dotted curve) and shown as green. Then a damping oscillation is fitted (red dashed curve) for the first $20ps$ dynamics.

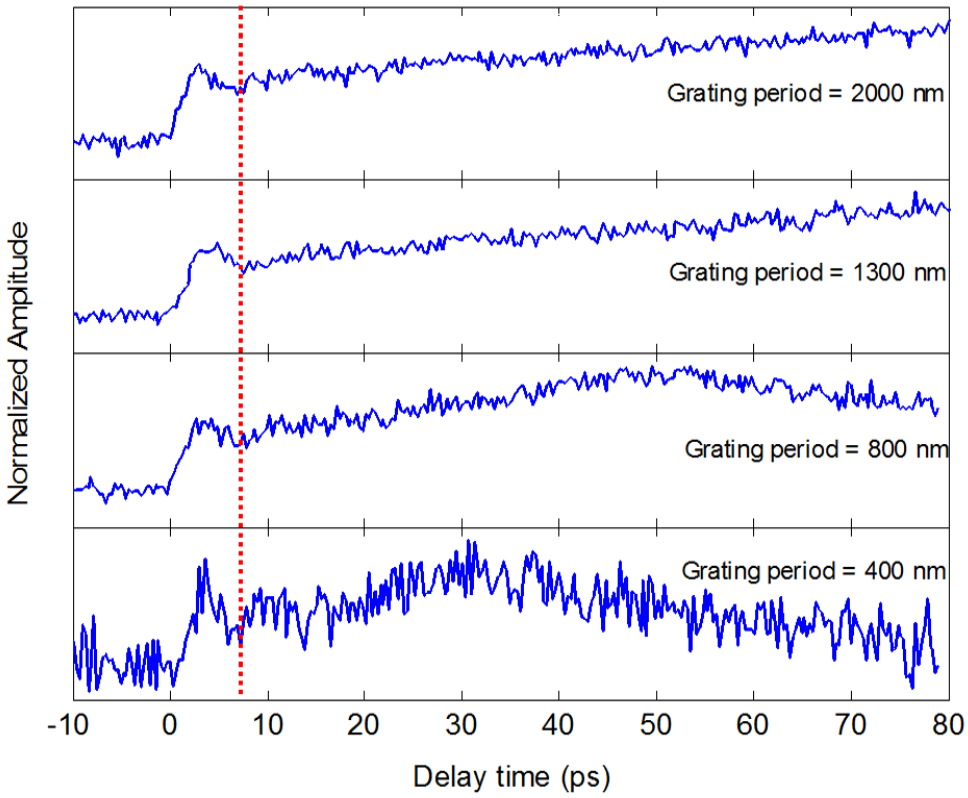

Figure 4.6: Similar fast damping oscillations from different grating periods on reference Ni/Si samples demonstrate the longitudinal acoustic waves propagate within nickel nanostructures.

4.4.2 Result from Surface Acoustic Waves

Different from longitudinal modes, surface acoustic waves are transverse modes which propagate along a surface or interface. As pointed out in the last chapter, we analyze dynamics at the longer delay-time scales to study surface acoustics.

Fig. 4.7 shows long-time signal from grating periods of 1050nm and 300nm from the same nano-patterned thin film sample (sample I). Following the same method, we remove the thermal decay part (pink curve in Fig. 4.7) and apply Fourier transform to obtain the spectrum (right side in Fig. 4.7).

In our experiment, SAWs are surface stress induced by the excited nanograting; therefore the SAW frequency is determined by two factors: (1) the wavelength of SAWs Λ, which is set by the nano-grating period P; (2) SAW phase velocity, which depends on the elastic property and the density of the materials. When the SAW is concentrated near an interface of two or more different material, the effective phase velocity depends on elastic properties and density of materials at both sides of the interface.

To study the material dependence, a more direct comparison is made between different samples with the same (or similar) grating periods. Fig. 4.8 shows the time-resolved signal and frequency spectrum for different samples: the nano-patterned thin-film sample I and II with grating period $P = 1050$nm, and the reference nickel-on-silicon sample with $P = 1000$nm. The spectrum from left to right shows the 1^{st} order frequency peaks at 4.6, 4.8 and 5.1GHz for thin film I, II and Ni/Si samples, respectively, followed by their 2^{nd} order peaks The ratio between frequencies on thin film sample I and the reference Ni/Si sample is different from their wavelength ratio as $4.6/5.1 \sim 90\%$ comparing with $1000/1050 \sim 95\%$. This indicates the influence of the 100nm thin film on the effective phase velocity of SAWs.

This difference indicates that SAW is sensitive to the interface materials where it propagates. This region size corresponds to the penetration depth of SAWs (ζ), which is a fraction of its wavelength (Λ). Our nano-SAW experiment in Chap. 3 showed grating-size dependence on SAW

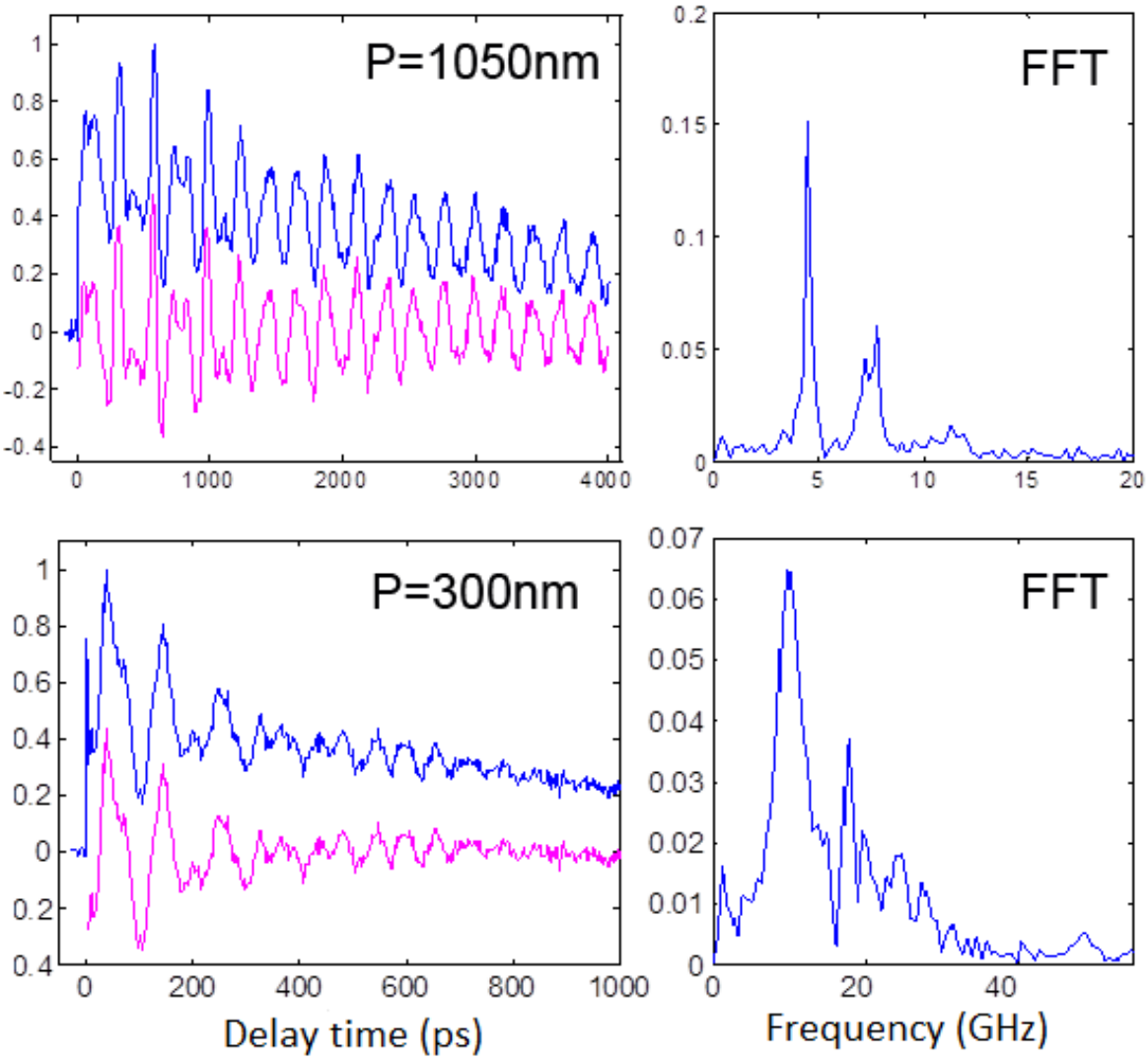

Figure 4.7: (Left) Dynamics of surface acoustic wave oscillations on longer delay-time scans with (blue) and without (pink) thermal decay background for 1050nm and 300nm grating periods from nano-patterned thin film sample (I). (Right) Fourier transform spectra from SAW-only signal.

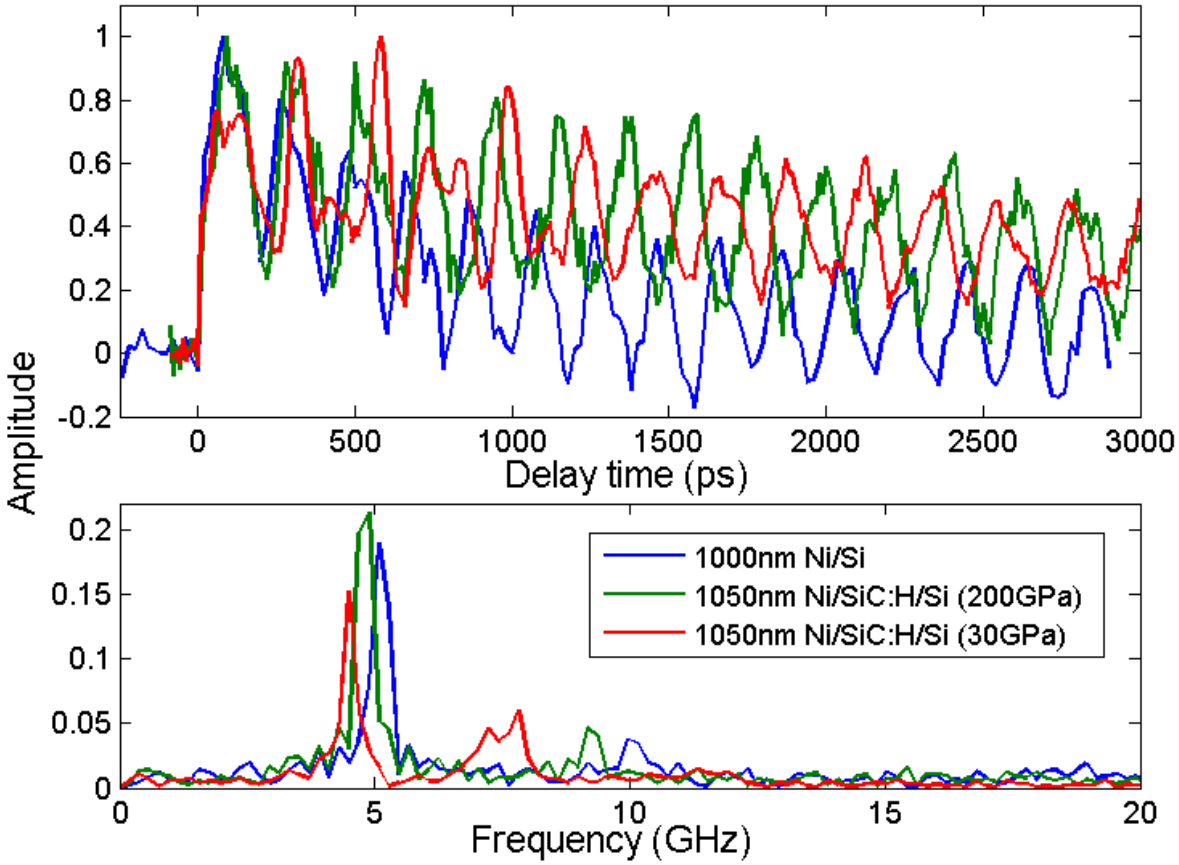

Figure 4.8: Time-resolved signal and frequency spectra on P=1050 nm grating from nano-patterned thin film sample I (red curve), P=1050 nm grating nano-patterned thin film sample II (green curve), and P=1000 nm grating reference nickel-on-silicon sample (blue curve). The frequency peaks for these samples are different for both fundamental and second order SAWs, indicating the thin film influence.

frequencies and velocities due to the nanostructure. Here with the presence of α-SiC:H thin film, three regimes are introduced according to the ratio between SAW penetration depth ($\zeta \sim \Lambda/\pi$) and film thickness (T): (1) the penetration depth is much larger than the thin film ($\zeta \gg T$), SAWs propagate mostly in the silicon substrate and the frequency is determined by Young's modulus and density of silicon substrate; (2) SAWs are confined around the boundary of the thin film and substrate ($\zeta \sim T$), the elastic properties of both α-SiC:H thin film and silicon substrate play important role in the SAW velocity; (3) SAWs are confined mainly within the thin film ($\zeta \ll T$), so that the SAW frequency reflects the mechanical property of the thin film. Note that SAW wavelength at fundamental frequency is equal to the period P of nano-grating, but higher-order wavelength can be a fraction of P, so the penetration depths for different orders are different. In some circumstances, the fundamental SAW oscillation reaches down to the silicon substrate while the second-order SAWs are confined within the thin film.

Taking the film thickness into account, we designed our nano-patterned thin film sample to cover all of these three regimes. At large grating period, $P = 1500$nm, SAWs propagate mainly in the silicon substrate; for intermediate grating period P from 1050nm down to 300nm, first order SAWs covers both thin film and substrate while the second order SAW is confined more in the thin film; for small gratings, $P = 150$nm, SAWs are mainly limited within the thickness of the thin film.

The mismatch of frequencies in Fig. 4.8 demonstrates the dependence of penetration depth for thin film characterization and also that different SAW excitation orders can provide additional information in the measurement. The difference of the 1^{st} order frequency on thin film sample I and II indicates that our measurements are very sensitive to the elastic properties and density of the 100nm thin film, although penetration depth of SAWs at wavelength of 1050nm is about 330nm, bigger than the thin film thickness. Also, the second order signal of thin film sample (I) and reference Ni/Si sample are peaked at 7.8GHz and 10.5GHz respectively. The ratio between them is bigger compared with that from the first order because the wavelength from second order SAWs is shorter and therefore more affected by thin film.

From Chap. 3 we learn that SAW velocity is mainly determined by the substrate. When the

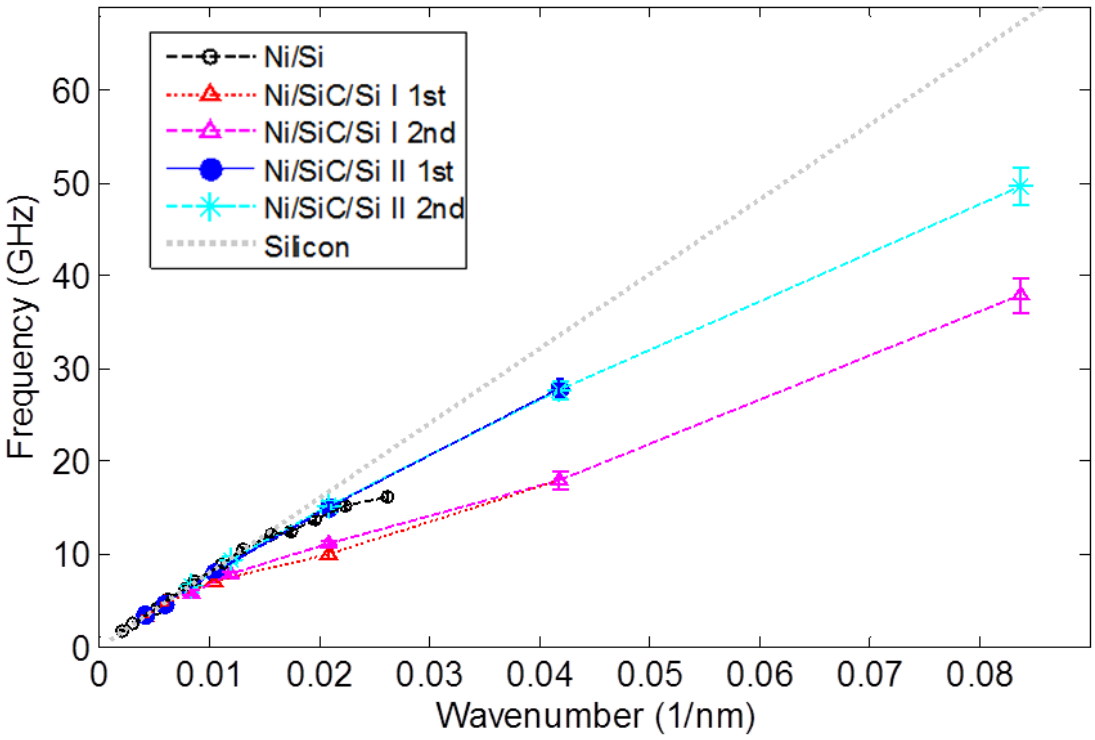

Figure 4.9: SAW frequency as a function of wavenumber ($k = 2\pi/P$) on three different samples comparing with silicon dispersion (gray dotted line): first order SAW dispersion measurement from reference nickel-on-silicon sample (black dot), first (red) and second (pink) SAW orders measurement from thin film sample (I), as well as first (blue) and second (cyan) SAW orders from thin film sample (II).

SAW wavelength shrinks, and thus the penetration depth decrease, the nanostructure will start to play a role, and moderately change the SAW velocity. However, with the presence of thin film, SAW is more localized within thin film as the SAW wavelength decreases. In this case, SAW velocity is determined mostly by the thin film property rather than the substrate as the wavenumber increases.

Fig. 4.9 plots the SAW frequency as a function of wavenumbers ($k = 2\pi/P$) for three samples at two different acoustic orders. The result of reference nickel-on-silicon sample is shown in black, the thin film sample I is shown in cold color (blue for 1^{st} and cyan for 2^{nd} order), and thin film sample II is shown in warm color (red for 1^{st} and pink for 2^{nd} order).

SAW velocity is given by $v_{SAW} = \Lambda_{SAW} \cdot f_{SAW}$, so we can calculate velocity for each wavenumber k at different orders. At small wavenumbers (big grating period), all of the first order curves overlap with each other and result in approximately the same velocity around $4800 m/s$. This number matches SAW speed in silicon which is consistent with our prediction that the SAW is propagating mainly in silicon substrate for 1500nm grating period. A gray dotted straight line is plotted according to this value to represent Rayleigh velocity of SAWs in silicon. An alternative way to interpret the dispersion is to plot the velocity as a function of wavenumber k, as shown in Fig. 4.10, with colors corresponding to Fig. 4.9(gray dotted line for Rayleigh velocity of silicon, black for reference Ni/Si sample measurement, warm color for thin film sample (I) and cold color for thin film sample (II)).

From both $\omega - k$ and $v - k$ dispersion curves (Fig. 4.9 and Fig. 4.10), it is easy to see the deviation of effective SAW velocity from constant SAW velocity in silicon. Note that the effective SAW velocity slowing down at large k is because that nanostructure plays a more important role at small SAW wavelengths, as discussed in previous chapter. It is also clear in Fig. 4.10 that the dispersion behaviors of thin film samples are different from the nickel-on-silicon result and also between each other. This indicates the SAW velocity depends on mechanical property and density of the different α-SiC:H films.

At an intermediate grating period, e.g. $P = 600nm$, the frequency and velocity are smaller than that from silicon value according to Fig. 4.9 and Fig. 4.10, although SAW wavelength is still

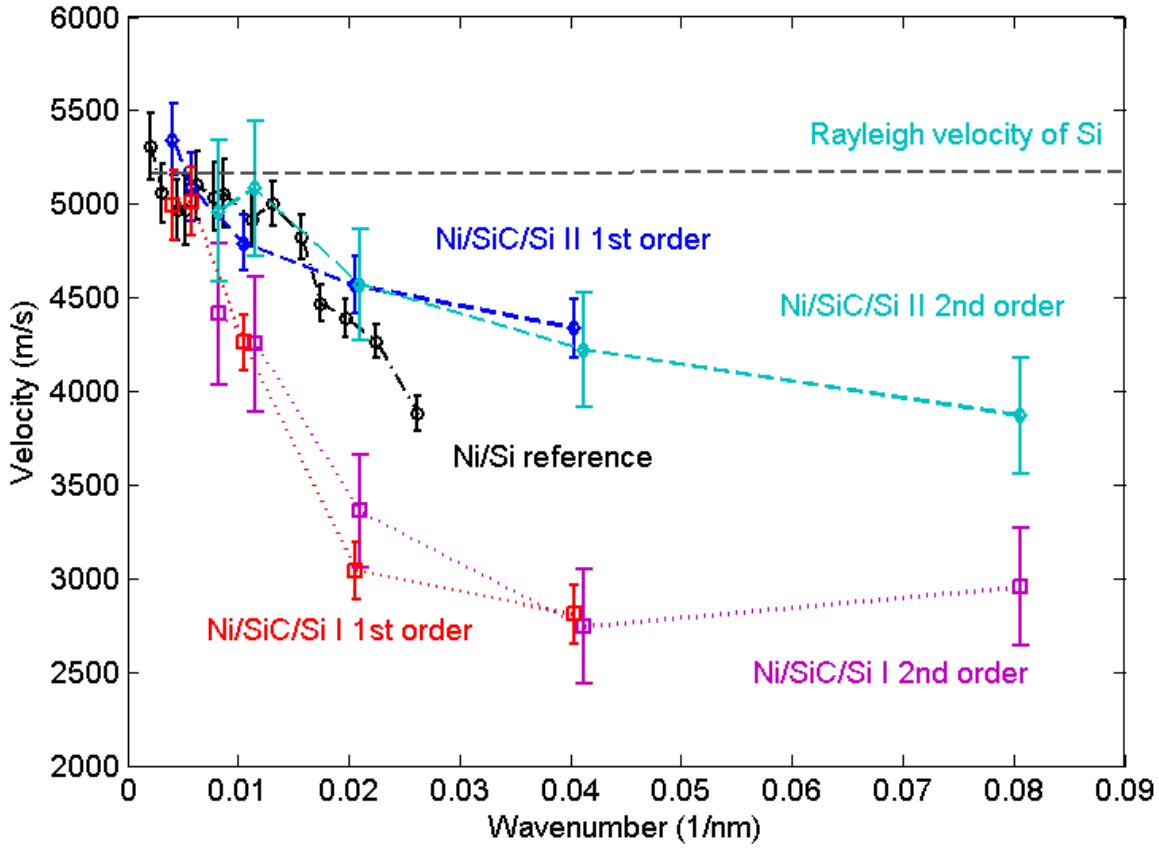

Figure 4.10: Effective SAW velocity as a function of wavenumber ($k = 2\pi/P$) for three different samples comparing with constant Rayleigh velocity from silicon substrate (gray dotted line). Colors match Fig. 4.9: red and pink colors are measured data points for thin film sample (I) 1^{st} and 2^{nd} order respectively, blue and cyan are for thin film sample (II) 1^{st} and 2^{nd} order respectively, and black for reference nickel-on-silicon sample.

a lot bigger than the thin film thickness. This can be explained by both the effect that mass loading from both film and nanostructure, as well as the fact that the SAWs are localized with an exponential decay function direct into the substrate, even when the penetration depth is relatively larger than the film thickness, there is a significant portion of the SAW affected by the film's presence.

Also from both $\omega - k$ and $v - k$ dispersion-relation curves of second order SAWs for nano-patterned thin film samples follows the first order result for most wavenumbers, indicating the consistency of two different SAW orders. This shows the reliability to use higher order SAWs to study ultra thin films. One point at $k = 0.021$, which corresponds to the first-order SAWs from 300nm and the second-order SAWs from 600nm grating period, on both thin film samples shows a small deviation between first order and second order in Fig. 4.10, corresponding to 300nm SAW wavelength. At this particular wavelength, the penetration depth is close to the 100nm film thickness. In another word, the first order SAW generated from 600nm grating period propagate in both thin film and silicon substrate, but the second order is confined within the thin film, the same as the 1^{st} order SAW excited by 300nm grating period. However in the latter two cases, the nanostructures affect the velocity in different amount, which explains the gap at $k = 0.021$ point for both thin film samples.

The dispersion curves from the nano-patterned thin film sample deviate from the horizontal silicon velocity sharply at small wavenumbers, then this trend slows down and the slope becomes smaller at larger k values. This "bending" behavior at the largest k (smallest grating period) indicates the SAWs are completely confined within the thin films, where the velocity, which is expected to be much smaller, depends on the thin film and nanostructures.

The measured velocity values on the two nano-patterned thin film samples are listed in Table 4.1. For thin film sample I, the SAWs propagate mostly in the silicon substrate at large 1500nm gratings with velocities of $4900m/s$, consistent with typical values for silicon. For 150nm gratings when SAWs are localized within nanostructure and thin films, it yields a much smaller velocity at $2800m/s$, which is consistent with a softer material, i.e. thin film with lower Young's

SAW wavelength (nm)	v_{SAW}(m/s) on sample I first order	v_{SAW}(m/s) on sample I second order	v_{SAW}(m/s) on sample II first order	v_{SAW}(m/s) on sample II second order
1500	4900 ± 190	4410 ± 380	5345 ± 190	4963 ± 380
1050	4900 ± 180	4520 ± 360	5101 ± 180	5084± 380
600	4250 ± 150	3360 ± 300	5076 ± 150	4569 ± 300
300	3060 ± 153	2740 ± 306	4526 ± 153	4224 ± 306
150	2800 ± 156	2900 ± 312	4335 ± 156	3870 ± 312

Table 4.1: Measured SAW velocities for nano-patterned thin film sample I and II on five different grating period; both fundamental and second acoustic orders are included here. Higher SAW velocities are measured when SAW wavelength is large so that it propagates in silicon substrate, while smaller velocities are obtained when SAWs are confined within a "softer" thin films

.

modulus.

Similarly, for thin film sample II, SAW velocity in large grating period is $5345m/s$, and in small grating is $4335m/s$. Taking the higher Young's modulus into account, this higher SAW velocity at short wavelengths are consistent with a stiffer film material compared to thin film sample I.

4.4.3 Modulus Calculation

From the measurements of the velocities of SAW and LAW, we can derive Young's modulus and Poisson's ratio.

First we need to extract the SAW velocity in thin film samples. Great efforts have been made to analyze high frequency dispersion of SAWs using different models in our group [10], and we can also use finite element simulations to extract the SAW velocity in thin film.

For the first thin film sample, the SAWs are confined only in the nanostructure and thin film. In the smallest grating case, we measure $v_{LAW} = 5263 \pm 140m/s$, and $v_{SAW} = 2800 \pm 156m/s$. Various mass-loading models can be used to analyze 1D gratings[10], or we can apply a finite element simulation to analyze this situation, as shown in Fig. 4.11. The thin film parameters are varied to fit the measured v_{SAW}, which in turn provide the SAW velocity in the thin film only

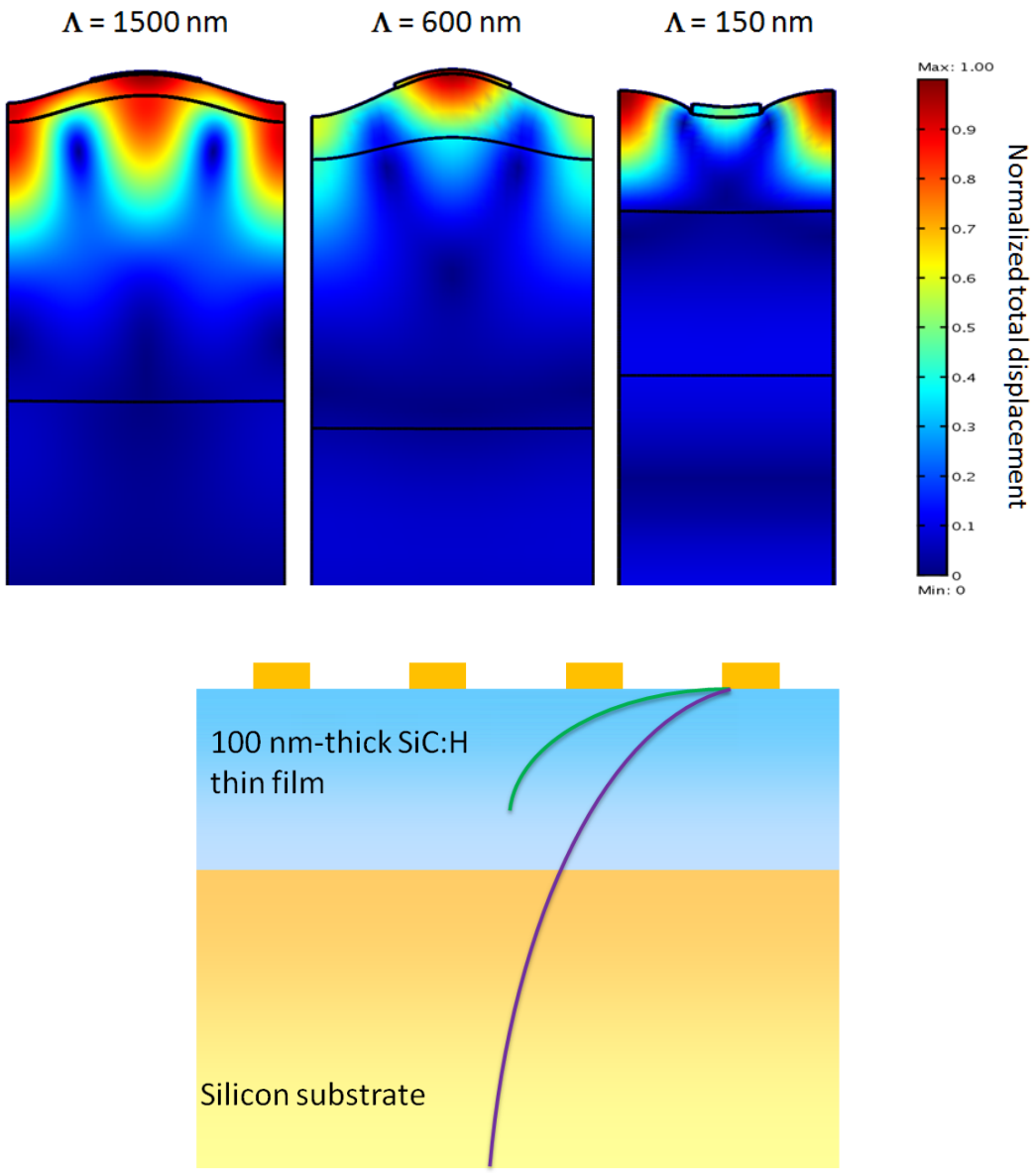

Figure 4.11: (Top) Finite element simulation based on first principles is applied to all five grating sizes in this experiment in order to extract the SAW velocity of thin film out of the measured SAW frequency. Color map demonstrates lattice displacement in the 1st order modes corresponding to SAW. From left to right are SAWs generated in $P = 1500$nm, $P = 600$nm and $P = 150$nm gratings, which clearly shows the transition of SAWs confined from silicon substrate to thin film. (Bottom) Schematic illustration of confinement of SAWs: longer penetration depth means SAWs reach down to the silicon substrate (purple curve), while shorter penetration depth corresponds to SAWs localized in thin film. Sizes not to scale.

without metal grating as $v_{SAW} = 2997m/s$.

Assuming isotropic thin film sample, we can calculate the elastic tensor from Eq. 4.8 and 4.9. Taking the density as $1.55 \times 10^3 kg/m^3$, we can calculate the elastic tensor. From Eq. 4.10 and 4.11 we can derive the Young's modulus as $E = 36 \pm 3$GPa, which is consistent with the nominal value, and the Poisson's ratio as $\nu = 0.24 \pm 0.07$.

4.4.4 Future Directions

We measure both the surface and longitudinal acoustic waves on the first nano-patterned thin film sample, and derive the Young's modulus and Poisson's ratio from it. However, for the second thin film sample, we are unable to detect the longitudinal echo signal from the thin film/substrate interface. For this sample, we can measure the surface acoustic velocity $v_{SAW} = 4335 \pm 156m/s$, which can be used to derive the shear modulus. It is smaller than the calculated transverse velocity from the nominal Young's modulus $E_{nominal} = 200$GPa as measured by our collaborators with a commercial apparatus.

In order to obtain the Young's modulus, an additional assumption is needed in place of v_L measurement for the Poisson's ratio. We use 0.24 ± 0.07 based on the lower limit of stiff pure SiC thin film (0.17) and upper limit from the softer Sample I (as high as 0.31). With this assumption, we can estimate the value of E from only the SAW velocity measurements as 130 ± 40GPa. This modulus, mass density as well as the assumed Poisson's ratio are all very close to that of the silicon substrate. In other words, the film and substrate have similar mechanical properties and are not distinguishable. This explains the absence of a longitudinal wave feature in the signal since very weak reflection of LAWs could happen at the thin film/substrate interface. We thus demonstrate that $E_{nomimal}$ is incorrect and the high sensitivity of our technique enables the measurement of this large discrepancy.

This photoacoustic metrology technique is suitable when the elastic property of the thin film differs from that of the substrate. By carefully choosing the substrate and nano-structured materials, this technique can be applied to dielectric or metal thin films. Also, we demonstrated a

generation of 35nm wavelength SAWs in the previous chapter, and our colleagues recently successfully generated longitudinal acoustic waves in 5nm thin films, these reports ensure the application of this technique to sub-10nm thin films.

Another direction to improve the photoacoustic metrology is to extend this measurement to the non-contact, non-destructive transient grating technique. A shorter grating period can be generated by interfering two EUV pump beams. Recent development of high-energy HHG in our group [13, 2] makes it possible to generate EUV at short wavelength and high flux, which enables the generation of SAWs with even shorter wavelength than achieved here.

4.5 Conclusions

In summary, we develop a new photoacoustic technique to characterize the mechanical properties of ultrathin films. By focusing an ultrafast laser onto a nano-patterned thin film sample, SAWs and LAWs are launched simultaneously, and measured by coherent EUV pulses. Both the frequencies and velocities of the SAWs and LAWs of the thin film are extracted. As a result, the elastic properties, Young's modulus and Poisson's ratio of 100nm thin films are obtained. This approach can easily be extended to measurements of sub-10 nm films.

Chapter 5

Observation of Quasi-ballistic Thermal Transport

5.1 Introduction

As discussed briefly in Chap. 1, thermal dissipation and management is a big challenge as the nanoelectronics keep shrinking in size. The Fourier law describes diffusive thermal conduction and is the fundamental theory for many heat conduction experiments. However, the Fourier law is based on local thermal equilibrium and thus requires sufficient scattering between heat carriers. When a system has a characteristic size that is smaller than the heat-carrier mean free path, this law will break down. In the case of dielectric or semiconductor materials, heat is carried by phonons, whose mean free path can be a few hundred nanometers. It implies that systems with structures < 100nm are very likely in the ballistic regime.

A number of experiments have reported the breakdown of Fourier law and ballistic thermal transport in nano-systems, including superlattices[49], carbon nanotubes [11], and silicon nanowires [12]. Fig. 5.1 shows two examples of ballistic effect in thermal transport. The left curve is from reference [7] measuring thermal conductivity of silicon films at different film thicknesses. The points are experimental results and lines are predictions based on the Boltzmann transport equation. The measured thermal conductivity decreases as the film thickness shrinks. The right curve is from [9], which measured the cross-plane thermal conductivity of Si/Ge multilayer material at varied film thicknesses. This measurement reports a lower conductivity than bulk value (top solid curve) which also decreasing as the thickness decreases.

But for the nano-to-bulk system, i.e. a nanoscale heating source and its surroundings, despite

its direct relevance to the practical issue of thermal management of nanoelectronics [50], nano-enabled energy systems [51, 52], and nanomedicine [15], this "nanoscale heat sink" issue has not been experimentally explored before our experiments. So I focus on this geometry, and pattern a nanostructure on a bulk substrate to mimic the nanoscale heating source.

5.2 Thermal Transport at Nanoscale Interfaces

Basic theoretical calculation of thermal conduction is discussed in Chapter 2. In this chapter, since our goal is to study the heat transfer from a nanoscale hot spot to its surroundings, we focus only on the thermal transport at this interface.

According to the Fourier law $q = -k\nabla T$. When heat flows from one material to another without any additional loss at the boundary, the temperature distribution exhibits a deviation from the straight line because of the different thermal conductivity k's. If there is an additional loss at the boundary, thermal boundary resistance r_{TBR} is defined to take this into account as $r_{TBR} = \Delta T/q$, ΔT being the temperature difference across the boundary. As shown in Fig. 5.2, when there is no thermal resistance, the temperature is continuous at the boundary, while a temperature drop exists at the boundary with a thermal boundary resistance.

We can also use the Fourier law to describe the thermal transport across a nanoscale interface even with ballistic effects - just add its contribution to the effective interface resistivity ($r_{Effective}$). Thus with the boundary condition, the thermal transport across the interface of the nanostructure and bulk surroundings can be described as

$$\rho_{nano} h_{nano} C_{nano} \frac{dT_{nano}(x,t)}{dt} = -\frac{(T_{nano}(x,t) - T_s(x, y=0, t))}{r_{Effective}}. \tag{5.1}$$

where ρ is density, C is heat capacity, h is nanostructure height.

Combined with the heat diffusion equation,

$$\frac{\partial T_s(x,y,t)}{\partial t} = \frac{k_s}{C_s}\nabla^2 T_s(x,y,t), \tag{5.2}$$

we can solve the thermal distribution on both sides of the interface.

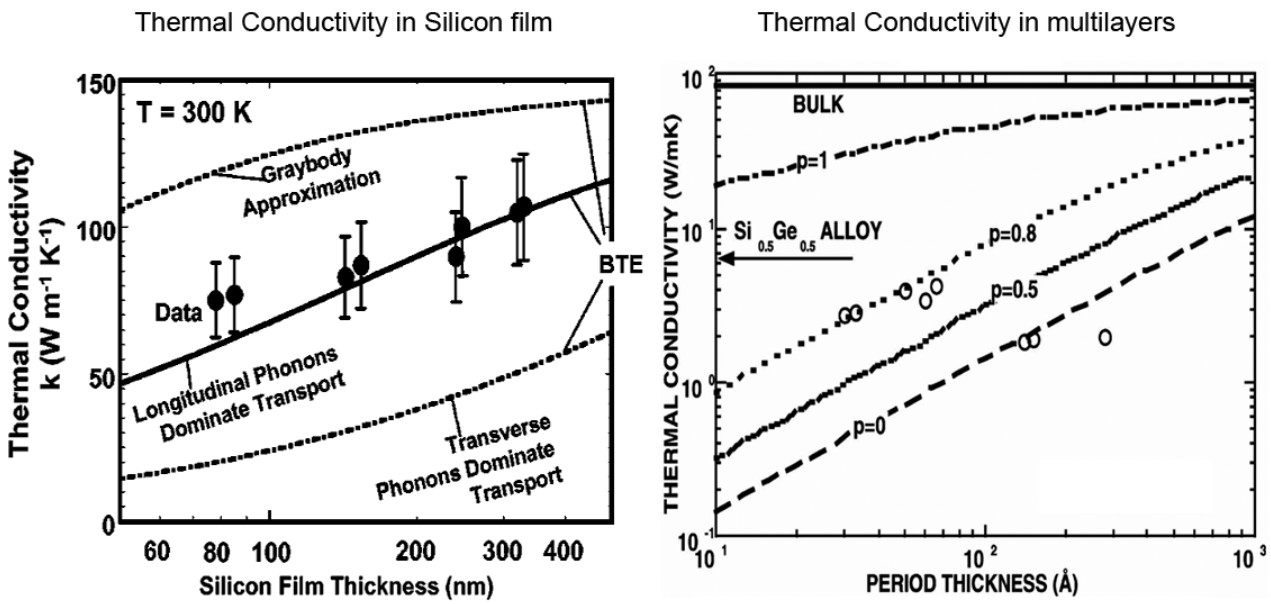

Figure 5.1: Experimental data shows varying thermal conductivity in nano-systems. Left figure is from [7], data from [8] with dots as experimental measurement and curves are prediction from Boltzmann transport equation (BTE). This figure reports the effective room-temperature thermal conductivity decreases as thickness of silicon film shrinks. Right figure is from [9], which measures the cross-plane thermal conductivity change as a function of layer thickness on a Si/Ge multilayer sample and ballistic effect in multilaers.

.

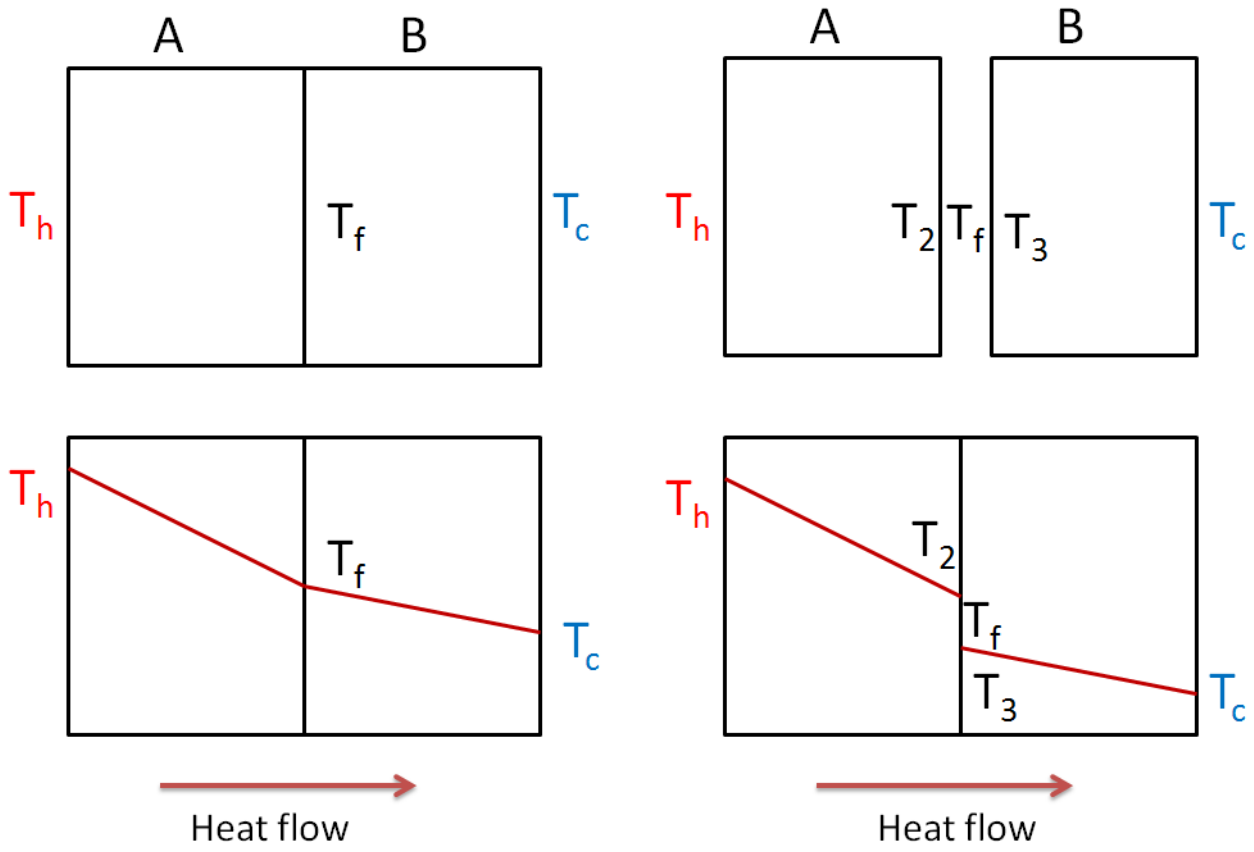

Figure 5.2: Temperature distribution at interfaces of two different material, with top figures showing the physical geometry of the system, and bottom the temperature gradient. If there is no thermal boundary resistance (left), different slopes of lines correspond to different thermal conductivity of A and B systems; with a thermal boundary resistance r_{TBR} (right), there is a temperature drop at the boundary besides the different slope temperature gradient, which defines the $r_{TBR} = -\Delta T/q$.

5.3 Observation of Quasi-ballistic Effect

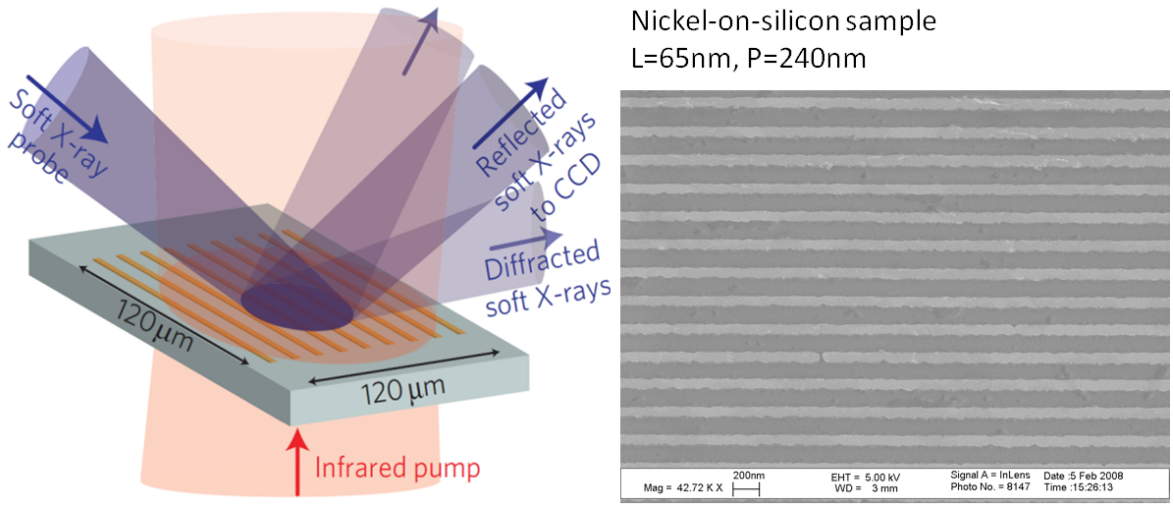

Figure 5.3: Illustration of pump-and-probe geometry on 1D nanogratings. IR pump beam is focused from backside of the sample to create an impulsive heat source while the EUV probe beam from HHG is used to detect time-resolved diffraction signal.

We first try to study the heat transfer in nano-to-bulk systems on a 1D nanograting sample. Similar to photoacoustic research, we use the infrared-pump and EUV-probe experimental setup. We split the output of the 1.8mJ, 30fs, 2kHz 800nm Ti:sapphire amplifier system into two parts $(80-20\%)$. The majority part is focused into a argon-filled hollow waveguide to generate the 30nm HHG probe beam, and the other part is focused on the sample with a fluence of $3mJ/cm^2$, and works as an impulsive heating source.

Two sets of samples are examined in the first experiment; both are nanoscale nickel lines patterned on transparent substrates, fabricated using electron beam lithography and a lift-off process, with the first set patterned on sapphire substrate and the second on fused silica. The crystal structure of sapphire has a relatively long phonon mean free path at room temperature at around $100-150$nm, while fused silica is a glass which has very short mean free path at about 2nm. Periodic nickel lines are patterned on a area of $120\mu m \times 120\mu m$ spot, with height $h = 20$nm, length of $120\mu m$ and line width L varying from 2μm down to 65nm, and a fixed duty cycle of 25%. The illustration of sample geometry with IR back-side pump and EUV probe is shown in Fig. 5.3.

When heated by the infrared laser pulse, only the nickel lines absorb the laser light, and the electrons are rapidly heated up. Then the energy transfers from electrons to lattice through electron-phonon coupling, causing a fast thermal expansion and slow relaxation as heat dissipate down to the substrate, which results in a secondary thermal expansion of the substrate. The EUV beams monitor this full dynamics by detecting the phase change due to structural modulation as a function of the pump-probe delay time. The time-resolved signals are shown in Fig. 5.4 for different linewidth L's of nickel/sapphire samples. The fast oscillation in the signal is due to surface acoustic wave which has been discussed in detail in Chap. 3. The longer time decay part is due to the thermal decay and is the focus of this chapter. Thermal equilibrium inside the nickel lines is rapidly achieved in less than 10ps, and the nano-second scale thermal decay dynamics depend on both thermal transport across the nickel-to-substrate boundary and decay rate in the substrate.

The physical process involves several steps: heating the nano-structure, energy is absorbed by electrons and quickly achieved thermal equilibrium in nickel lines, fast phonon-electron interaction release the energy to phonon and dissipates down into the substrate. During this thermal process, a mechanical thermal expansion of this nanostructure is taking place, which induces additional phase in the EUV propagation, resulting in a transient diffraction change of EUV beams.

To connect the thermal dissipation to our EUV measurement, we use an analysis similar to that used for transient thermoreflectance (TTR) measurements. Three physics models are used and connected to describe the whole process, including thermal transport at the interface; thermal mechanics of nanostructure and the substrate as $\Delta h/h = \alpha \Delta T$, where α the coefficient of thermal expansion (CTE) of the material; and finally Fresnel optical propagation with the additional phase in EUV propagation as $e^{-i(k(x+\Delta h)-wt)}$ [38]. Based on these models, we are able to fit our measurement with an effective thermal interface resistivity, as shown in red and blue curves in Fig. 5.4.

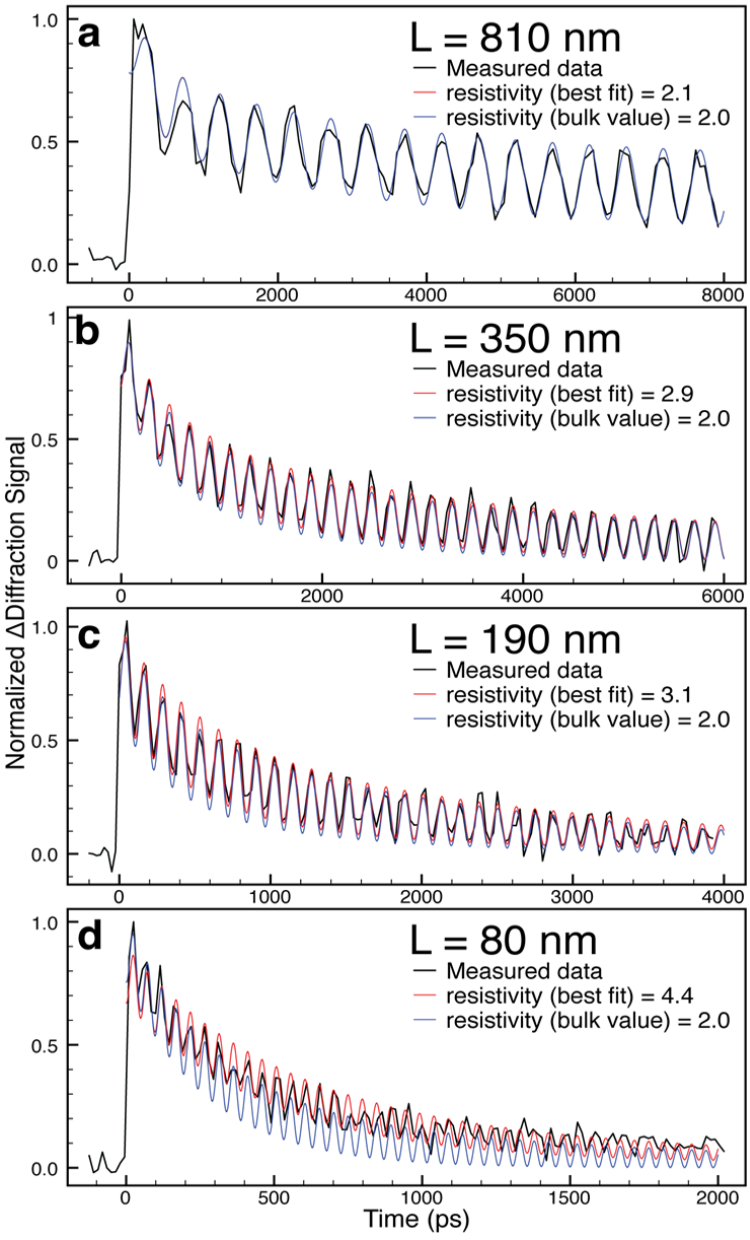

Figure 5.4: Time-resolved dynamic EUV diffraction signal for Ni line widths of a. 810 nm, b. 350 nm, c. 190 nm, and d. 80 nm on sapphire substrate. The signal in each case consists of a sharp rise due to impulsive laser heating, a thermal decay due to interfacial thermal transport, and an oscillation due to surface acoustic wave propagation. The best fit for the interface effective resistivity including interface and ballistic correction components (units of $10^{-9} Km^2/W$) for each line width is shown as a red line, while the blue line shows the fit obtained by neglecting ballistic effects and simply using the bulk value. The deviation between the two fits increases with decreasing line width and indicates the increasing importance of the ballistic effect at small interfaces.

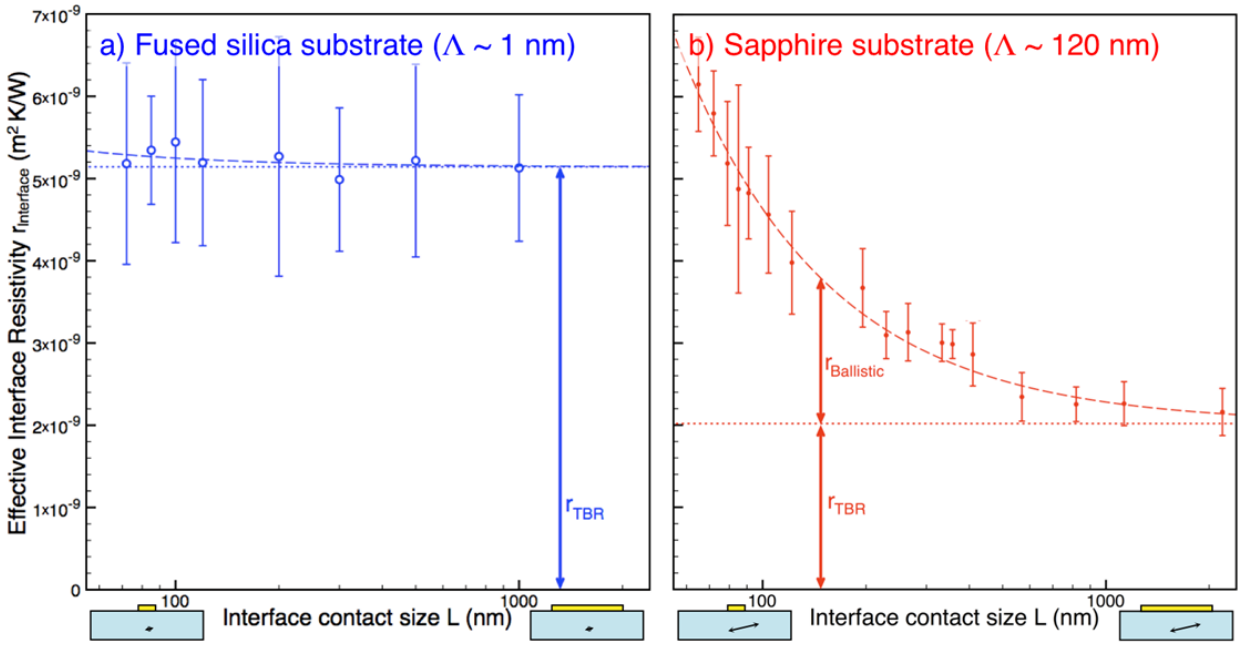

Figure 5.5: Measured effective thermal resistivity for nickel nanostructures of width L deposited on a) fused-silica and b) sapphire substrates. The schematics below each figure indicate the change in linewidth on the scale of phonon mean free path Λ in the sample (indicated by the arrows). The blue and red dotted horizontal lines show the large-scale (bulk) resistivity r_{TBR} for data from the fused silica and sapphire substrates, while the dashed curves indicate $r_{Ballistic}$, the ballistic correction that must be included for linewidths $L \leq \Lambda$. The error bars indicate the standard deviation in the fits to the data.

5.4 First Observation of Quasi-ballistic Effect

Fig. 5.5 shows the effective thermal interface resistivity as a function of grating width L of both samples with fused silica substrate (left) and sapphire substrate (right). It is clear to see the deviation from the constant thermal boundary resistivity predicted by the Fourier law on the sapphire sample while no deviation is observed in the fused silica sample. The total interface resistivity demonstrates an increase proportional to the Knudsen number Λ/L. When the size of the interface (L) is much larger than the phonon mean free path (Λ), our measurement yields the bulk thermal boundary resistivity, as measured in a typical TTR experiment. However, at the smallest line width ($L = 65$nm), the interface dimension is much smaller than the phonon mean free path in the sapphire substrate ($L < \Lambda_{Sa} \sim 120nm$ at room temperature) and we measure an interfacial resistivity that is as much as three times higher than the bulk value. In contrast, measurements of heat flow in nanostructures deposited on fused silica (with shorter mean free path $\Lambda_{FS} \sim 2nm$) yield no deviation from the bulk thermal resistivity, within the error.

5.4.1 Troubleshooting

As easily noticed, this nano-grating sample enables us to measure the quasi-ballistic effect at the nano-to-bulk interface but the oscillating signal makes the data a little difficult to interpret. Using IR-pump and EUV-probe on a single nanowire may generate clean thermal signal and prevent any possibility of thermal accumulation. Actually this experiment was started with a nanowire design - we fabricated single nickel lines, pumped with IR laser and probed with EUV beams.

However it turned out that no signal could be observed. This is mainly because of the energy loss of our focusing optics. EUV is absorbed by many materials, and normal optical lenses do not work for focusing. We use a grazing-incidence toroidal mirror on a manually controlled mount, and focus the EUV beams to a $\sim 100\mu m$ round spot, which is much bigger than the width of the nano line. Big loss of the beam off nano line makes the diffraction signal-to-noise ratio very low. A better mechanical design for the control of the focusing mirror will help to minimize the spot size

and increase the signal-to-noise ratio. Also using a tight focusing curved mirror and focusing the beam into an elongated spot is helpful to detect the dynamics of single nickel lines. In addition, recent updates of our laser amplifier system (now improved to 3kHz, 30fs, 2.1mJ) will be helpful in increasing diffraction signal.

5.5 Conclusions

In this thermal experiment, we observe the first quasi-ballistic effect on nano-to-bulk thermal transport dynamics with 1D nano-grating samples. We observe the breakdown of conventional Fourier heat conduction when the hot spot size is close to the phonon mean free path of the substrate, and observe a size-dependent effective resistance proportional to the Knudsen number Λ/L. This opens new perspective in nanoscale thermal transport, and in order to test the material, polarization, dimension and temperature dependence of the ballistic effect, follow-up works have been performed and will be discussed in next chapter.

Chapter 6

Extended Works on Nano-interface Thermal Transport

6.1 Introduction

Chap. 5 reports our first observation of quasi-ballistic thermal transport with coherent EUV beams on samples of 1D nickel nano-grating patterns. It demonstrates the thermal transport behaviors at the same interface size in materials are different: for large mean free path (sapphire) it's quasi-ballistic while for small mean free path (fused silica) it's diffusive thermal transport. This proposes the significance of thermal management in nano-to-bulk systems where ballistic effect occurs, such as in silicon-based nanoelectronics since silicon has mean free path $\sim$ 200nm. This chapter discusses a few follow-up research works. We first perform a similar experiment with a silicon-substrate sample, which directly connects to the semiconductor industry and also has higher mean free path. By comparing data from silicon results to sapphire in the previous chapter, we are able to check the material dependence.

We then scrutinize the thermal transport of a 2D patterned sample, which is more similar to the practical industrial devices. By comparing data with that from 1D patterned samples, we are able to estimate the ballistic effect on more complex devices. In addition, instead of investigating nano-interface samples with different sizes, we study the thermal transport rate as a function of the temperature of heat sink, where phonon mean free path changes accordingly. In this experiment, there are several challenges on the temperature control and model building, so further discussion and trouble shooting is also included in this chapter. Finally we made the first attempt of dynamical thermal imaging via pattern matching imaging.

6.2 Material and Polarization Dependence: Ballistic Effect in Silicon Substrate

The first experiment to extend our nanoscale thermal transport observation is to replace the sapphire substrate with silicon because silicon has an even longer mean free path than sapphire, which in turn may result in an observation of the ballistic effect with larger nano-structure sizes. In addition, silicon slightly absorbs IR light, thus it is possible to explore polarization dependence of the thermal dynamics of the silicon substrate sample which is not applicable in the transparent sapphire case. Last but not least, silicon is essential to the semiconductor industry and characterizing the thermal transport behavior of silicon samples is of great interest for the industry companies, which helps us to build a collaboration with them.

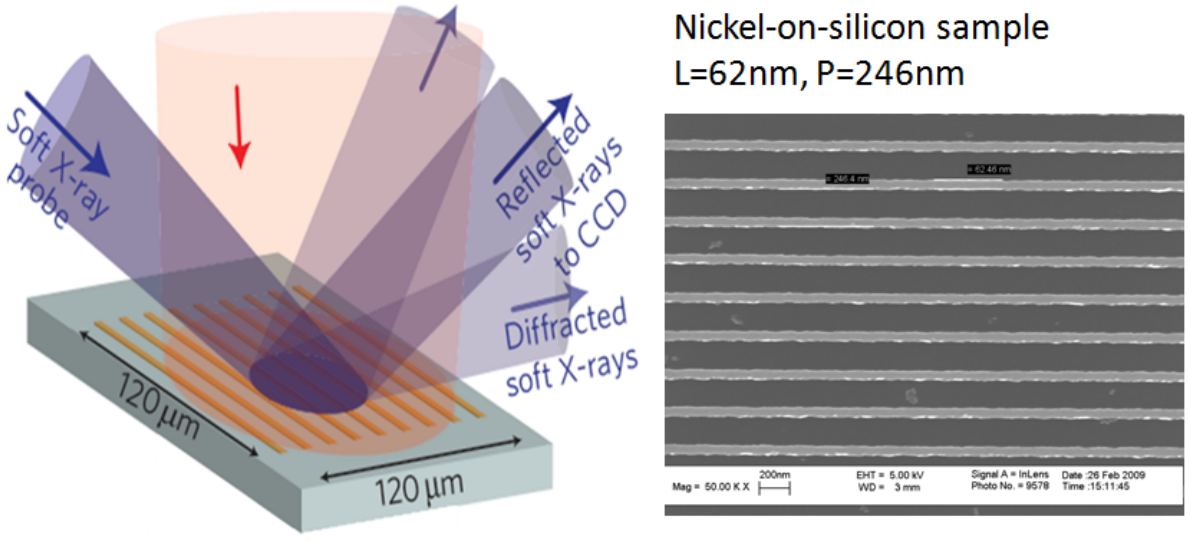

Figure 6.1: 800nm pump pulse illuminates the front side of the 1D nickel-on-silicon sample, and the EUV probe beam is incident on the sample with a slightly different angle to obtain time-resolved diffraction signal. Right figure shows the SEM picture of the smallest Ni-Si sample.

Silicon is opaque to 800 nm pump pulse. Therefore instead of back-side illumination like the sapphire case, we modified the setup to front-side illumination, as shown in Fig. 6.1. The absorption depth of silicon is on the order of a few microns, much bigger than the thermal transport range

we are interested in, so the amount of heat absorbed by silicon substrate is small and only causes a constant offset of the surface modulation and thus is negligible in analyzing EUV diffraction signal. The sample size is designed according to the nickel-on-sapphire case, with grating linewidth L varying from $62nm$ to $1\mu m$ and duty cycle fixed at 25%.

Dynamical signal measured by EUV diffraction as a function of pump-and-probe delay time is shown in Fig. 6.2 (a) and (b) with the grating size of $L = 500nm$ and $L = 180nm$, respectively. In order to make an intuitive comparison of the thermal decay in this Ni/Silicon sample to previous Ni/Sapphire sample, scans on the same size of gratings are plotted together as shown in Fig. 6.2 (c). The obvious difference of thermal decay rate at longer delay time is because the thermal conductivity in silicon ($k = 149W/(m \cdot K)$) is higher comparing with sapphire ($k = 35W/(m \cdot K)$).

Polarization dependence is also examined on all the nickel-on-silicon samples of different sizes using a half waveplate and a polarizer. Signals on s- and p-polarized pumps on $L = 350$nm and 750nm gratings are shown in Fig. 6.3. From a direct comparison on both gratings, we can claim that there is no significant difference observed for different polarization.

Similar to the last chapter, data analysis using simulation model that connects the thermal transport to mechanical expansion and finally to EUV diffraction signal has been performed to extract the effective interface resistance. In Fig. 6.3 (c), blue curve shows the simulation fit of effective interface resistance while the black curve is blue curve plus the SAW component. This approach is applied for both polarization pumps, and the effective interface resistivity for p-polarized light $r_{eff} = 6.5 \pm 0.7 \times 10^{-9} m^2 K/W$, and for s-polarized light is $r_{eff} = 6.6 \pm 0.7 \times 10^{-9} m^2 K/W$. This indicates the ballistic effect does not depends on the polarization of the incident pump beam light, and is the intrinsic property of materials themselves.

6.3 Thermal Transport in 2D Nanostructure

We also tried a 2D nanostructure, which relates more closely to practical nano-devices, in order to test the dependence on dimensionality. This experiment is driven by a direct industrial collaboration with a data-storage company. They use “bit-patterned media” (nanopatterned struc-

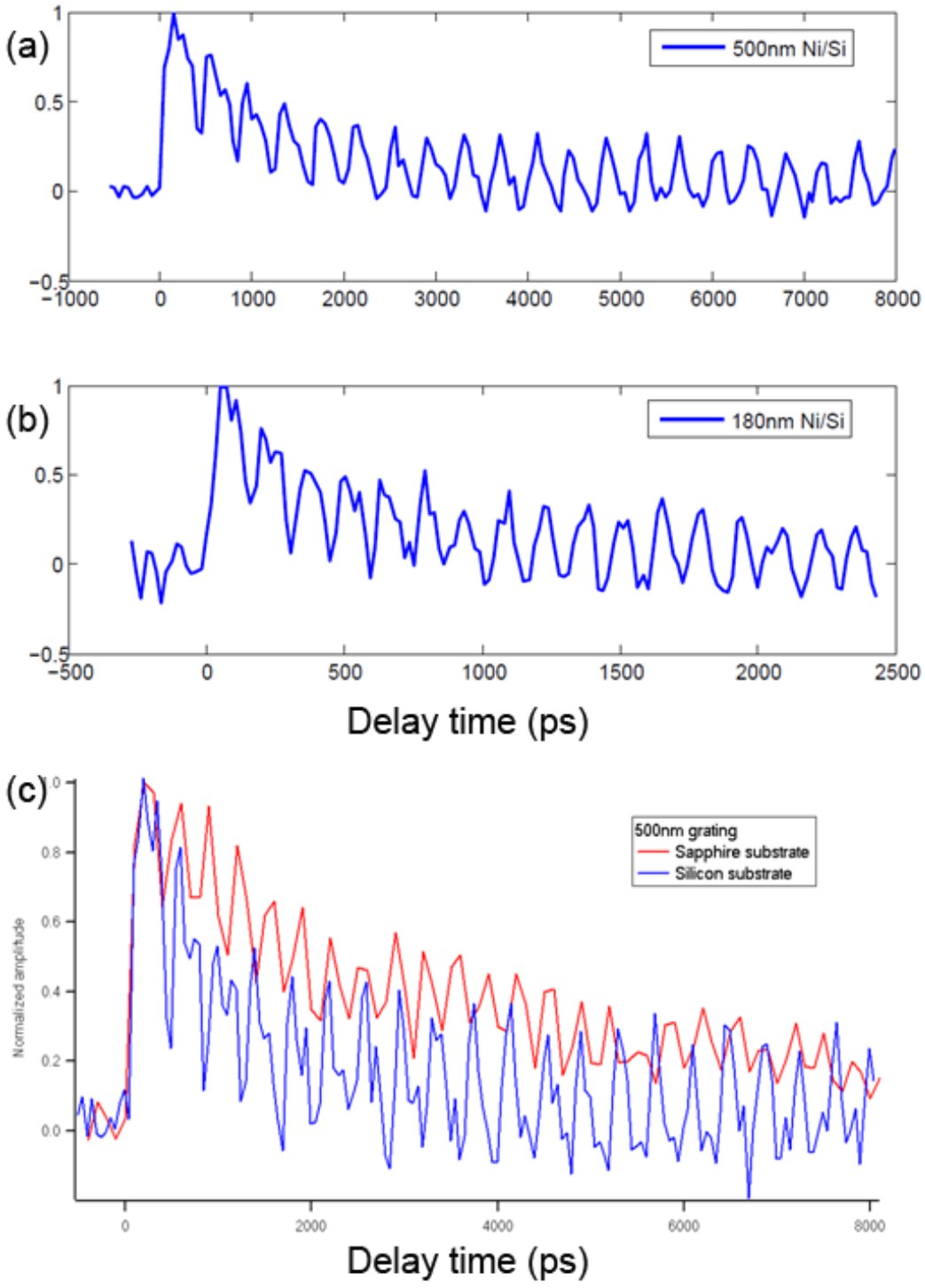

Figure 6.2: Time-resolved signal on nickel on silicon sample at (a) $L = 500$nm and (b) $L = 180$nm samples. (c) shows a direct comparison between signal on silicon substrate to that from sapphire substrate, which was used in last chapter. The dramatic difference of thermal decay rate mainly come from the different thermal conductivity of both substrates.

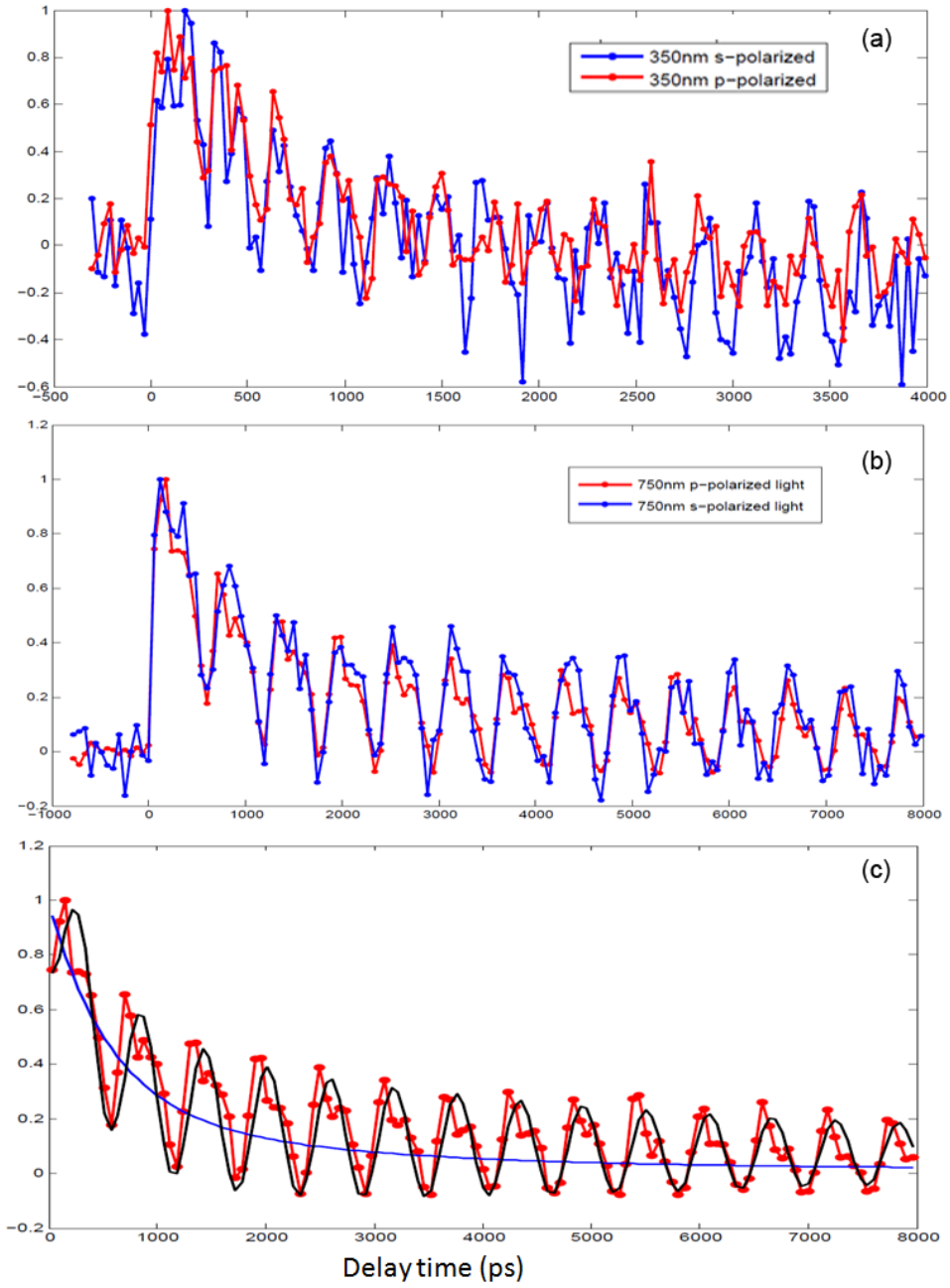

Figure 6.3: Time-resolved EUV diffraction signal with p-polarized (blue) and s-polarized (red) pump light on 350nm (a) and 750 nm (b) gratings. Applying similar simulation model that connect the thermal transport to EUV diffraction, we can fit our data with an effective interface resistance (c) to show the thermal decay rate (blue curve) or represent EUV signal (black curve after adding SAW component to blue curve). From both direct comparison, and effective interface resistance from fitting, we found there is no polarization-dependence in ballistic effect.

ture) to extend the limit of data storage density to higher value[40, 41].

The sample from our collaborator consist of 2D nano-arrays of cobalt/paladium multilayer pillars on top of silicon substrate, with the pillar widths L ranging from 25nm to 1μm. The time-resolved scan is shown in Fig. 3.9, where thermal transport signal is washed out from the big oscillation surface acoustic signal. Also if there is any ballistic effect in this sample, it may be from the nano-interface, and/or from the multilayer structures[9]. To study the dimensionality effect of the ballistic transport and make a direct comparison with the previous 1D result, we designed a reference sample consisting of a 2D array of simple nickel pillars on top of a sapphire substrate, with feature size L varying from 62nm to 1μm. We also use these two sets of sample to study ultrashort-wavelength surface acoustic waves doscissed om Chap. 3. The sample with pump and probe geometry is shown in Fig. 6.4, and the detailed sample geometry and SEM and AFM images can be found in Fig. 3.7. The EUV diffraction signal of a 2D nanostructure gives 2D diffraction pattern with precise reflection symmetry, as shown on the right side of Fig. 6.4. Therefore in our experiment, we bin the vertical signal to obtain the total EUV diffraction dynamics as a function of the pump-and-probe delay time.

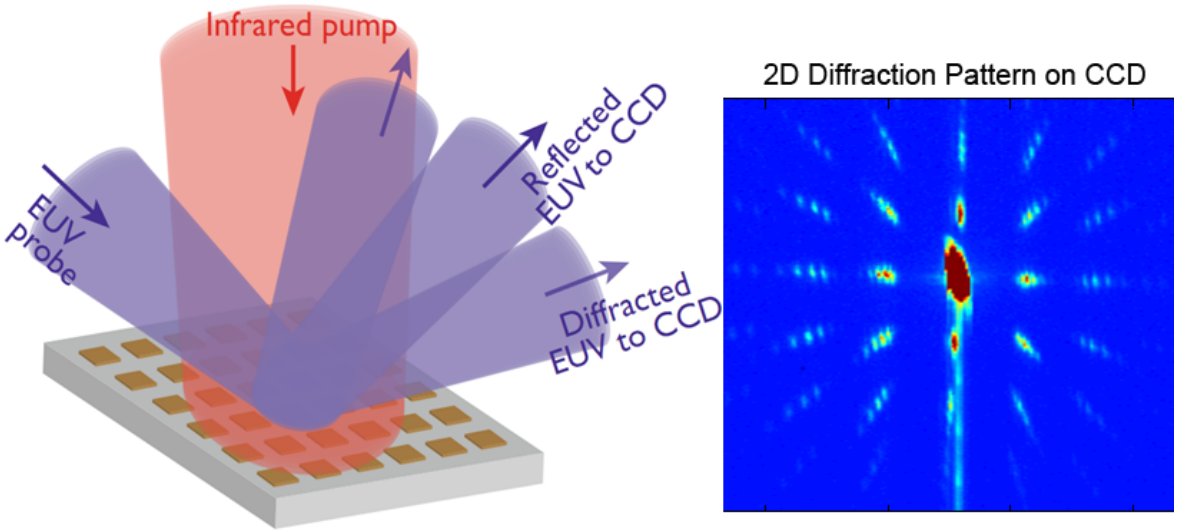

Figure 6.4: (Left) Pump and probe setup geometry on 2D nano-array gratings, and (right) diffraction pattern recorded on the x-ray CCD camera.

The time-resolved diffraction signal of the whole dynamical process is plotted directly comparing with that from 1D in Fig. 6.5 for $L = 350$nm (top) and 80nm (bottom) grating samples. Since the phonon mean free path Λ of sapphire is $100 - 150$nm, these two grating sizes correspond to $L < \Lambda$ and $L > \Lambda$ regimes. For larger grating size, the signal of 1D and 2D nanostructure are close to each other. However, for smaller gratings, the thermal decay part of the 2D sample is slower at short time, then in consistent with the 1D in longer time scale. It is clear that 2D signal from larger grating matches that from 1D, while the smaller grating shows deviation at short time scales.

The short-time signal corresponds to the thermal transport dynamics at the nano-interface, which includes the thermal boundary resistance and ballistic effect. Thus this discrepancy on the 80nm grating intuitively demonstrates a stronger ballistic effect in 2D nanostructure than that in 1D with the same small grating size. For the thermal decay signal at longer time scale, result from 2D matches that from 1D because here the thermal dissipation is dominated by the sapphire substrate.

We are collaborating with Ronggui Yang's group in theoretical analysis and try to build a 3D thermal transport model to re-construct the diffraction to calculate the effective interface resistance, so that we can provide further support on this conclusion.

6.4 Temperature Dependence of the Ballistic Effect

In the first thermal transport experiment, we vary the grating size (L) to cover both regimes of ($L > \Lambda$) to $L < \Lambda$. This "scan" experiment enables us to observe the transition crossover from diffusive to quasi-ballistic thermal transport. Instead of varying the grating size L, an alternative method to observe the diffusive-to-ballistic transition is to vary the mean free path Λ while keeping the nano-interface size fixed.

One approach to change the mean free path is through varying sample temperature. Materials at lower temperature tend to have less phonon scattering and therefore results in a bigger mean free path. Fig.6.6 shows the thermal conductivity (k), heat capacity (C) and mean free path (Λ)

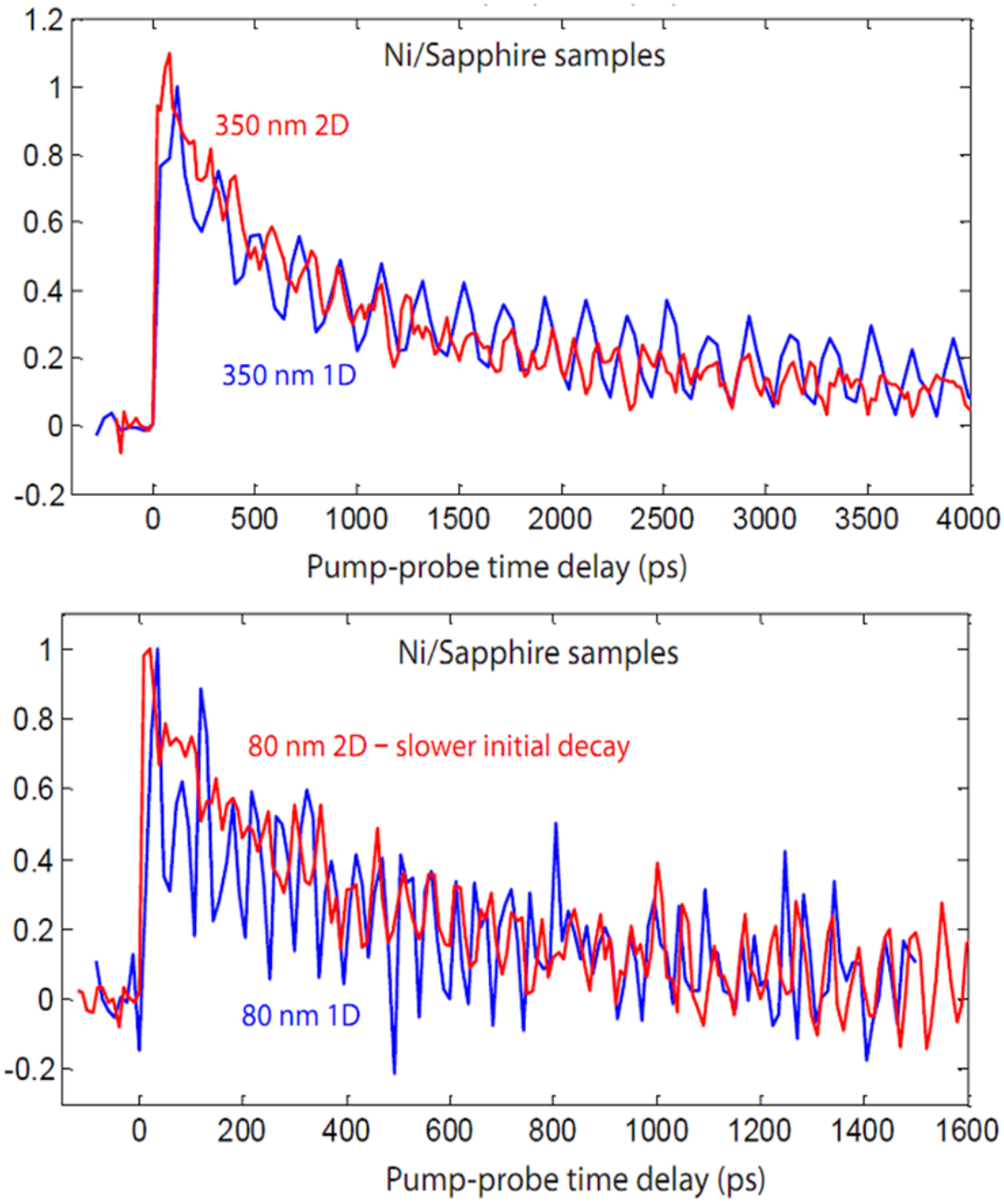

Figure 6.5: Time-resolved signal on $L = 350nm$ (top) and 80nm (bottom) 2D nanostructured nickel-on-sapphire gratings. Result is directly compared with that from 1D nano-gratings.

of sapphire as a function of temperature. In the range above 50K, the mean free path increases as the temperature decreases.

In order to change the temperature in our experiment, a vacuum-compatible temperature-controlled chamber is needed. We use a cryostat chamber from Janis Inc., which has heating wires and a cryogen transfer line connecting to an external liquid nitrogen dewar to control the temperature, and a thermocouple to measure the temperature of the sample. The available temperature ranges from $77K$ to $310K$ and the window material and geometry is suitable for optical pump.

We first tried the temperature-varying experiment with the nickel-on-sapphire sample, the same sample used in our first ballistic thermal experiment. However, when we cooled the sample down we found that the EUV signal drops rapidly to noise level and gives no signal at low temperature.

6.4.1 Troubleshooting

The sudden signal decrease makes this experiment impossible at the first glance. Then we made several efforts to troubleshoot this problem to measure temperature-dependence of thermal transport.

We first scrutinized the signal dropping as a function of temperature, and found the temperature stays well above 150K but drop quickly afterward, when we warmed up the sample, the signal recovered to normal value. Fig. 6.7 shows the counts at room temperature, 77K and then recover when it is warmed back up at 150K.

After confirming this repeatable process at 150K, we tried to blow additional argon gas to clean the surface of sample to avoid any contamination on the sample. It helped in bringing counts back a little at low temperature, but can't last long enough time. We use an ionization clean system (XEI evactron anti-contaminator), which is good at cleaning carbon-related contamination, but found it only helps within a very limited time. We also set up a cold finger next to the chamber, and cooled by liquid nitrogen, but it didn't help. These examinations confirmed that the signal drop was due to the contamination of the chamber, mainly from gas.

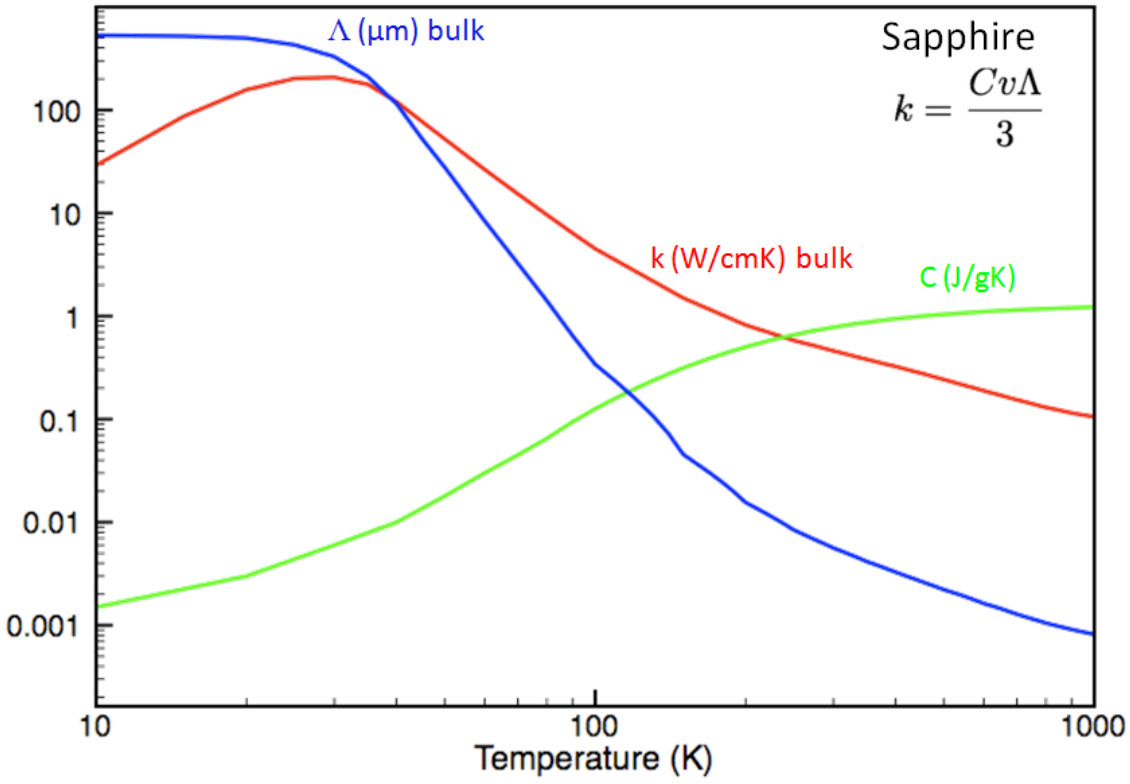

Figure 6.6: The temperature dependence of thermal conductivity k, specific heat C and phonon mean free path Λ of sapphire, related by $k = Cv\Lambda/3$ in traditional microscopic view. Picture from ref [10]

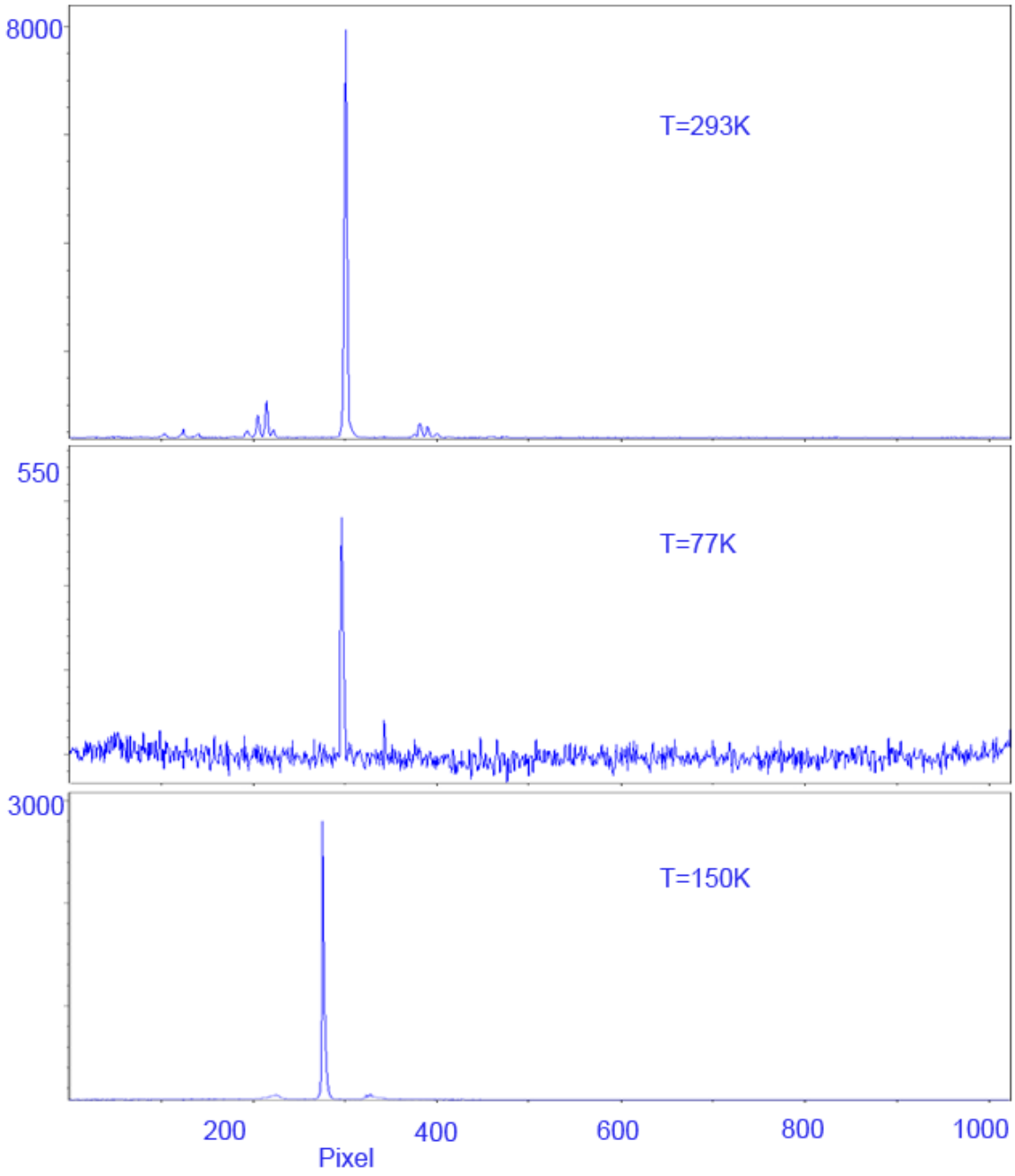

Figure 6.7: Observation of counts drop on CCD camera when lower the temperature from room temperature to liquid nitrogen temperature (78K), and the counts are partially recovered after the chamber/sample is warmed back up to $150K$.

To gain further information, we use a residual gas analyzer (RGA) system, which is a mass spectrometer and usually used to detect contamination in vacuum, to check the residual gases inside of the chamber. Fig. 6.8 demonstrates the result of RGA with residual gases peak at atomic mass unit of 2, 17, 18, 28 and 44 corresponding to gas of H_2, NH_3, H_2O, CO, and CO_2. After checking reference books of boiling temperature at vacuum level of 10^{-6} torr, we found that H_2O has a boiling point around $150K$.

These steps help us to identify that it is the condensation of water vapor inside the chamber that caused the signal drop. One possible method to solve this problem is to heat up the chamber to increase the vacuum level. However, current setup of high vacuum chamber use viton or silicone o-rings which is not compatible for temperature over 200 °C. Another option is to upgrade the chamber to ultrahigh vacuum level, which however requires a big improvement and investigation of the system. Thus we leave this for future research.

6.4.2 Thermal Transport at Varied Temperature

Instead of upgrading the whole system to achieve the full range of temperature control, our setup still enables us to obtain temperatures from about 160K to 310K. Fig. 6.9 shows the signal at low and high temperatures of the $L = 500nm$ nickel-on-sapphire grating sample. Signal of these two temperature shows some deviation, but is mostly because the thermal conductivity of sapphire substrate changes as a function of temperature, as can be noticed by the deviation at long time scale. Therefore it is difficult to examine the ballistic thermal transport at this point on the nickel-on-sapphire sample.

However, inspired by an article reporting a dramatic thermal effect changing between $150K$ and room temperature on silicon [53], we switched to nickel patterned silicon sample and finally obtained different thermal decay behavior at different temperatures. Fig. 6.10 shows the time-resolved EUV diffraction signal at room temperature and $160K$, top curves are the results from the $L = 500$nm sample, and bottom is from the $L = 200$nm sample. The signal of larger (500nm) grating shows no major difference at these two temperatures while the smaller grating demonstrates

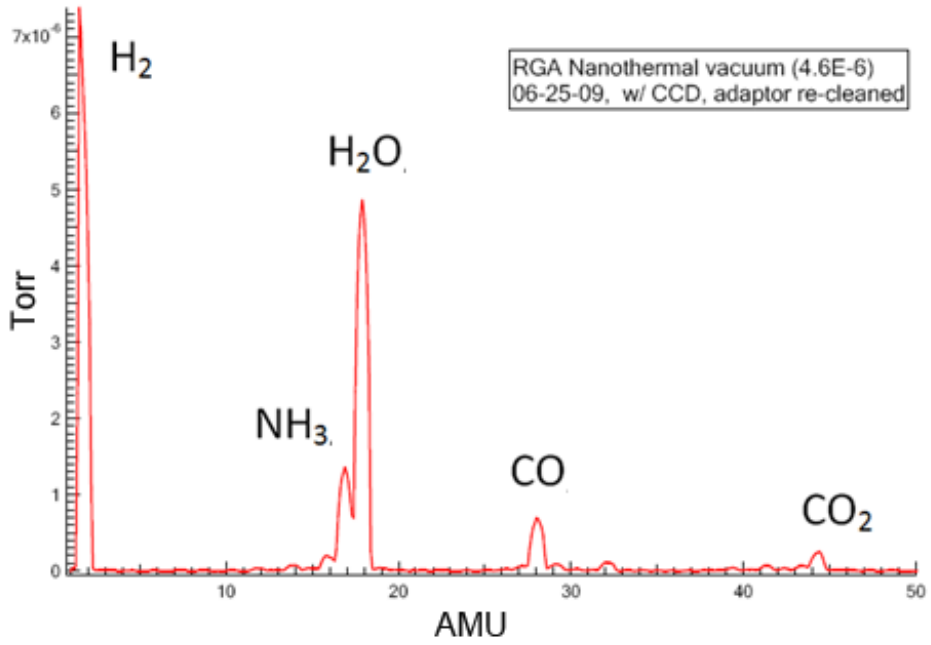

Figure 6.8: Residual gas analyzer result in our high vacuum chamber as a function of Atomic mass unit (AMU). Peaks at 2, 17, 18, 28 and 44 correspond to H_2, NH_3, H_2O, CO, and CO_2, respectively

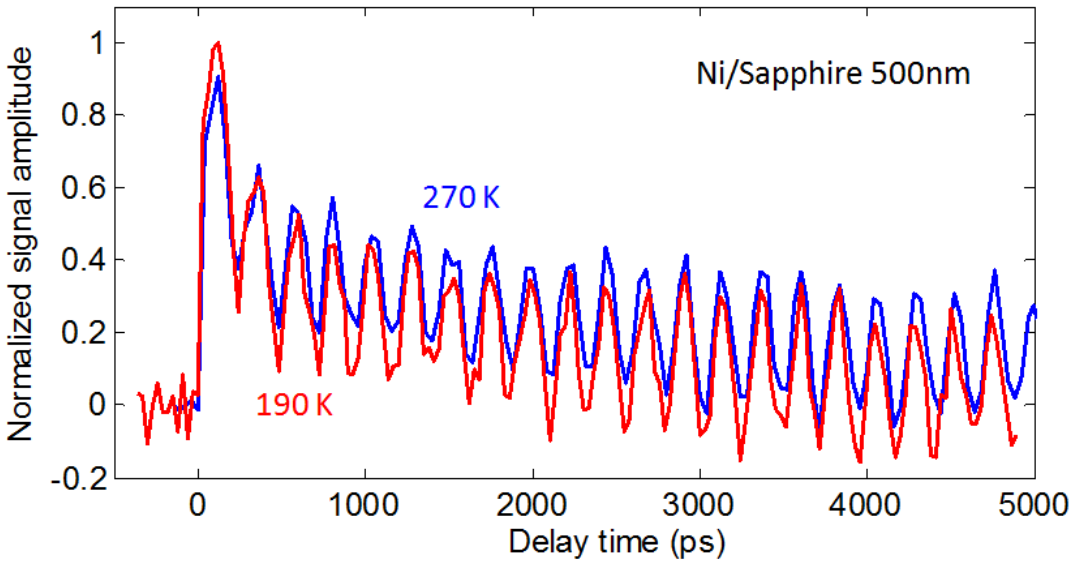

Figure 6.9: Time-resolved EUV signal of the 1D nickel-on-sapphire $L = 500nm$ sample at 190K (red) and 270K (blue) using a temperature-controlled cryostat chamber. The deviation of the two data curves at longer time scale indicates the thermal conductivity change at different temperature.

deviation between signals at these two temperatures. Combining the fact that the phonon mean free path Λ of silicon is around 200nm at room temperature, the $L = 200$nm grating experience the transition of $L \geq \Lambda$ to $L \ll \Lambda$ as the temperature is varied, while the $L = 500$nm does not cover this whole range.

From these result, we can make an intuitive conclusion that we are able to obtain a size-dependent effect in thermal transport. We control the temperature so that the varied mean free path covers the range of $\Lambda_{highT} < L$ to $\Lambda_{lowT} > L$, and therefore we can observe a transition from diffusive to ballistic thermal transport as the temperature decreases. Further analysis is taking place, relying on building a precise temperature-dependent parameter (thermal conductivity, coefficient of thermal expansion, etc.) in the simulation.

6.5 First Attempt of Dynamical Thermal Imaging

All of the samples in our nanothermal experiment are periodic nanostructures. But in order to generalize this measurement, a technique that can examine the thermal transport on any arbitrary sample is needed. The best solution is to develop a dynamical thermal transport imaging technique, which is the ultimate goal of this thermal project. Taking the same requirement for both temporal and spatial resolution, an imaging system with short wavelength and ultrafast pulse is needed. One possibility is to combine our pump-and-probe with coherent lensless imaging technique at short-wavelength regime.

Coherent lensless imaging is also known as coherent diffraction imaging. Our group has been developed a lensless imaging project using coherent EUV beams from HHG[54]. In this experiment, the EUV beams illuminates an object, and the scattered diffraction pattern from the object is collected by a CCD camera. The field intensity is measured directly, but the phase information is achieved by oversampling the diffraction pattern [55], then the image can finally be reconstructed using iterative algorithms that retrieve both the information of amplitude and phase.

For now, challenges lie in the difficulty of reflection-mode of coherent diffraction imaging. An alternative for dynamic imaging is to use the 2D diffraction image from periodic sample instead

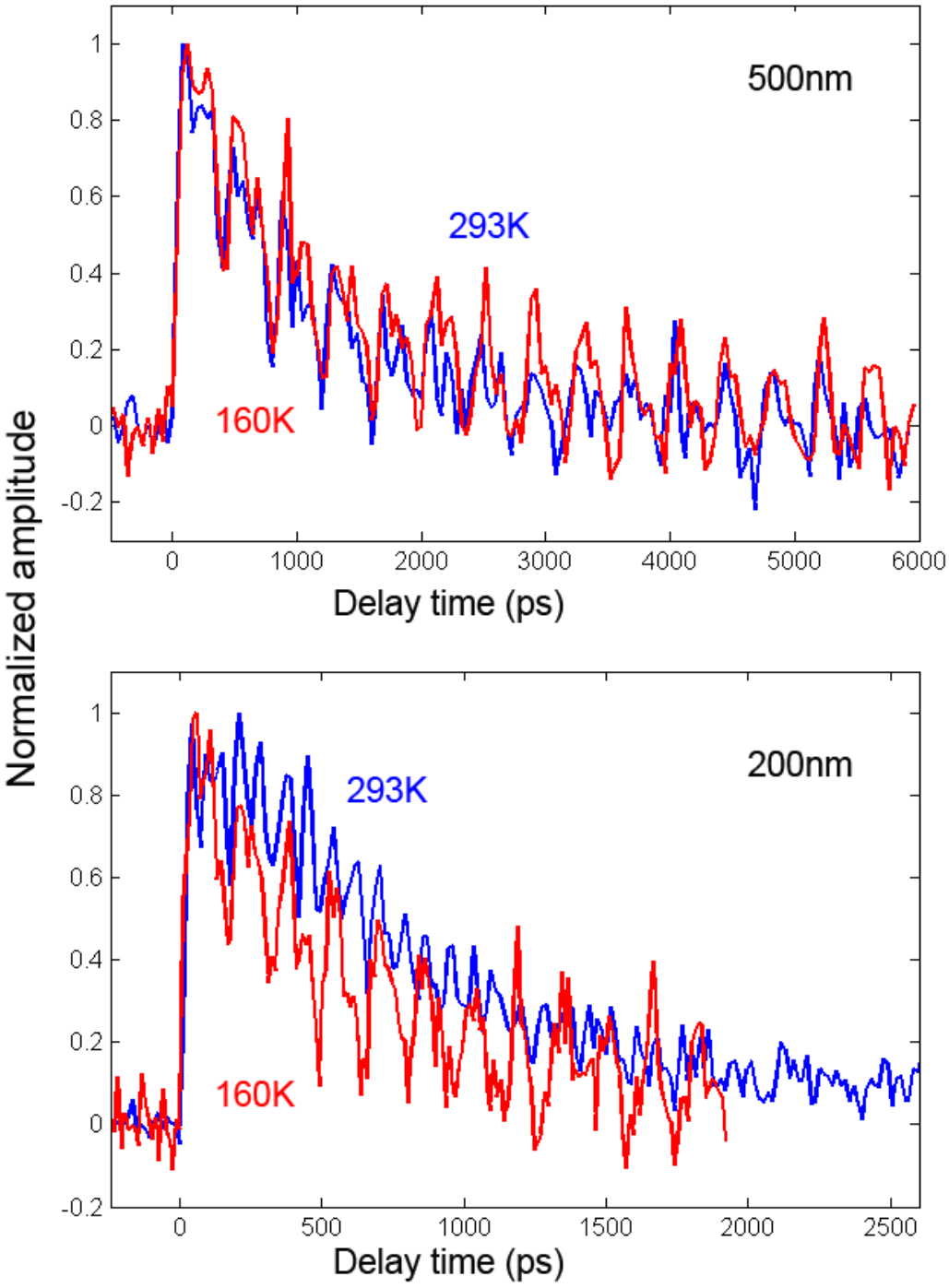

Figure 6.10: Time-resolved diffraction signal of the 1D nickel-on-silicon sample at room temperature (293K) and 160K. For $L = 500nm$ grating (top), signal at two different temperatures are consistent with each other, while for the $L = 200$nm gratings (bottom) the deviation of signal at two temperatures indicates a transition of diffusive to ballistic thermal transport.

of 1D vertical binned signal - take diffraction images at different delay times, and put together a dynamic thermal "movie" from it. Here we conduct a first try on a pattern matching imaging. In this case, instead of collecting oversampled image of the diffraction pattern and doing a full reconstruction (normal lensless imaging), we collect the simple 2D diffraction pattern, and use the periodic information of the sample to try to get the phase information.

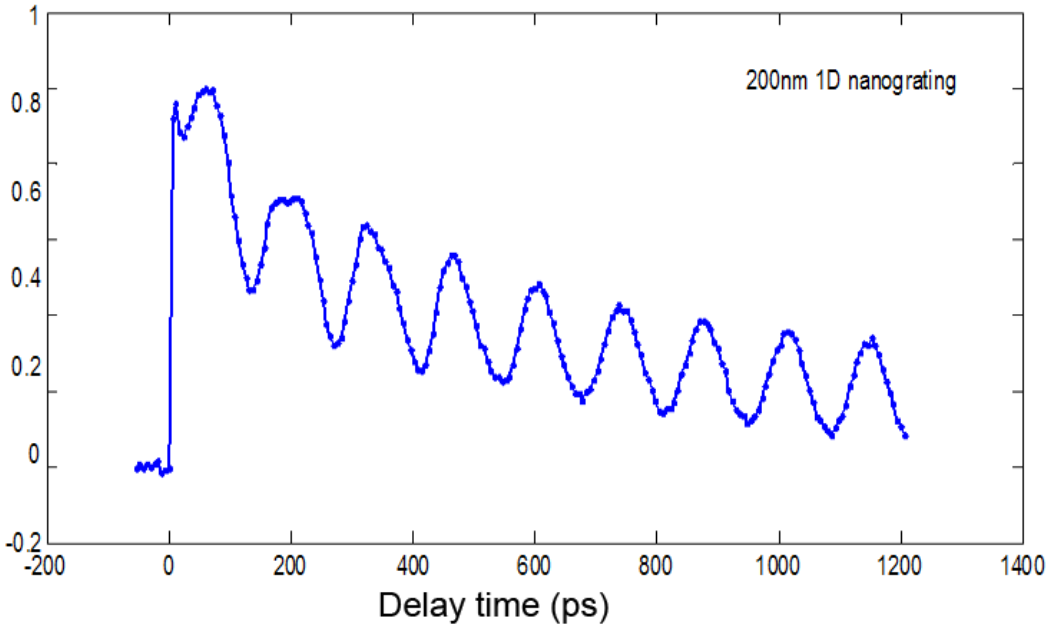

Figure 6.11: Pump-and-probe thermal dynamic scans after applying vertical binning of the diffraction signal of $L = 200nm$ nickel-on-sapphire grating. This result is similar to Fig. 3.3 or Fig. 5.4.

The thermal expansion of nanostructure changes after it is pumped by a laser pulse, and the diffraction pattern can be obtained. When the height changes as a function of pump-probe delay time, we are able to see the difference of diffraction image as a function of time - a dynamic imaging.

Fig. 6.11 shows typical dynamic thermal scan on a 1D nickel-on-sapphire nano-grating (similar to scans in last chapter), where the thermal signal amplitude changes as a function of time delay. In this scan, diffraction signal is binned vertically on the CCD camera. In this way we collect data at different diffraction orders at each delay time, resulting in a 2D (surface profile from thermal expansion and relaxation plus time) signal. Fig. 6.12 shows the diffraction image on a 1D

nickel-on-sapphire nano-grating and the counts distribution after binning vertically. This shows the diffraction signal on each pixel is relatively weak, which make it difficult to achieve a reasonable signal-to-noise ratio in imaging.

Fig. 6.13 shows the pump-on and pump-off diffraction patterns of the $L = 200nm$ grating, which are not obviously different at the first glance, just as in the vertically-binned case (see Fig. 3.3). Therefore we used the same trick to look at the thermal dynamics: (pure signal) = (pump-on signal) - (pump-off signal), and we can see clearly the signal is different before and after time zero.

We took the "pure signal" images at a sequence of delay times, comparing the dynamic imaging signal with the binned result on this $200nm$ grating, as shown in Fig. 6.14. We can also make a movie for the whole dynamics.

The experimental results are very positive and promising. We can even resolve the signal of the surface acoustics, as seen in Fig. 6.14 at delay time of 462ps vs. 540ps. We can get high temporal resolution dynamic imaging by shrinking the time steps, which is limited only by the resolution of the translation stage.

Note that, Fig. 6.14 shows that we have a good signal-to-noise ratio to observe the signal before and after zero delay time, but also can resolve the oscillation signal from the surface acoustic wave if comparing the signal at delay time of 462ps and 540ps. This implies that we can use similar technique to obtain dynamic acoustic imaging.

For now, we are working with our imaging group on revising the algorithm to reconstruct an image from the condition of periodicity. We also tried on a 2D nanostructure sample as discussed in section 2.3, but the signal-to-noise ratio is very low to detect any dynamical signal.

6.6 Summary

In summary, we work on a few works to extend our study of the nanoscale thermal transport in this chapter. We first switch to a silicon-substrate sample and verify that this ballistic effect does not depend on the polarization of the pump beams. We further extend the work to 2D nano-arrays

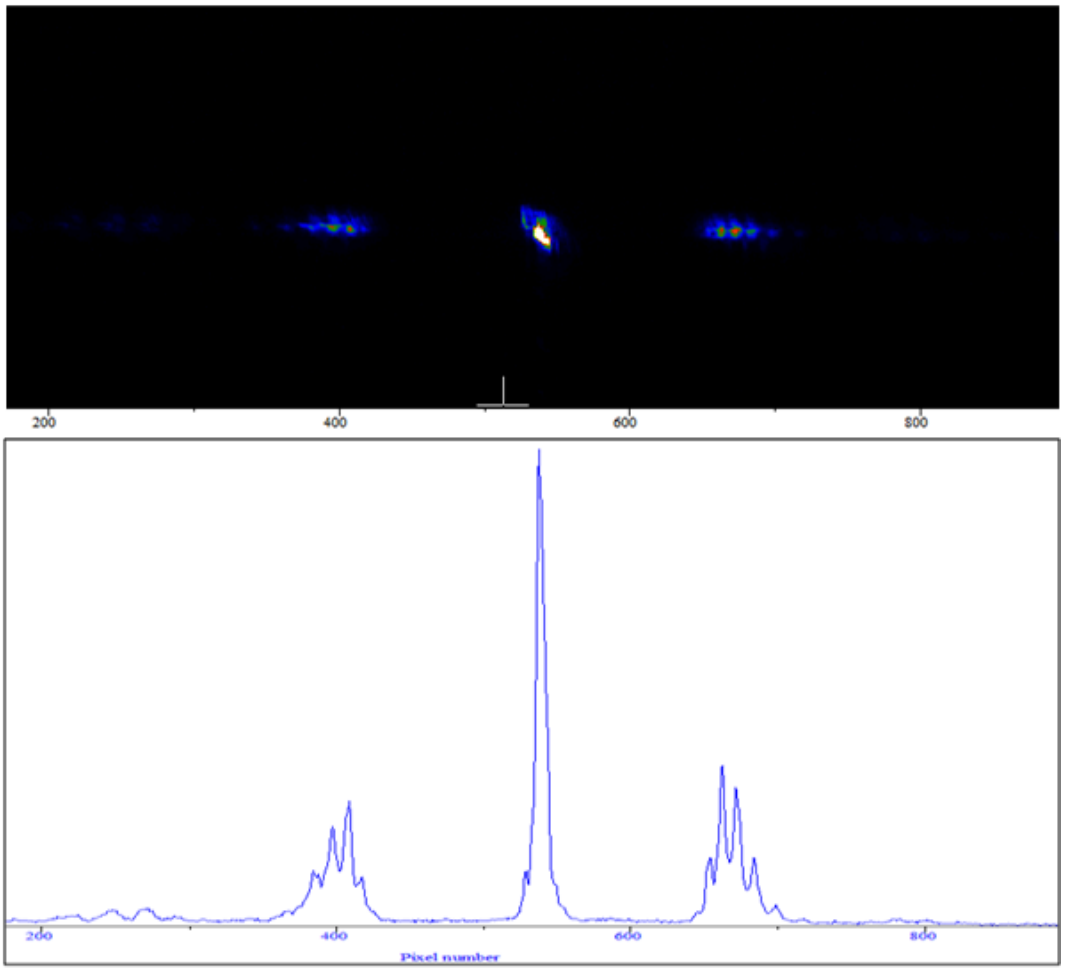

Figure 6.12: EUV diffraction of a 1D nickel-on-sapphire nano-grating. The diffraction is collected by an Andor X-ray CCD, and shows as a 2D image signal (top). We can also bin the counts vertically and obtain 1D total counts (bottom), which improves the signal-to-noise ratio while keeping the signal from different diffraction order due to the horizontal reflection symmetry. We use binned signal for all of the earlier thermal and photoacosutic scans.

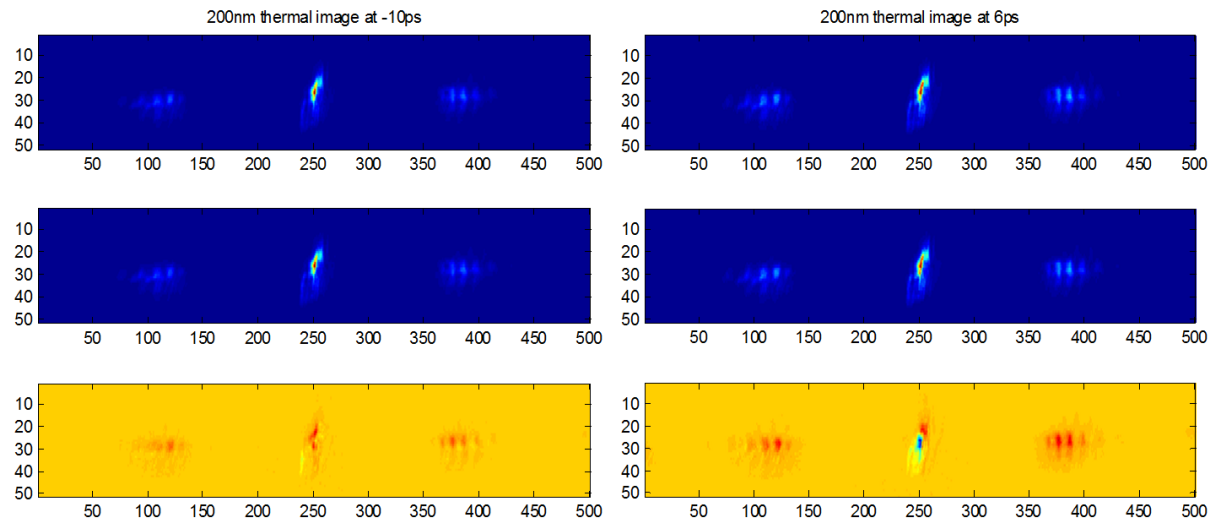

Figure 6.13: 200nm thermal dynamic images at delay time of -10ps (left set) and 6ps (right set). Top figures are at pump on, middle figures are at pump off, and the bottom figures are the difference after subtraction. Clearly from the bottom figures we see signal jumps before and after time zero.

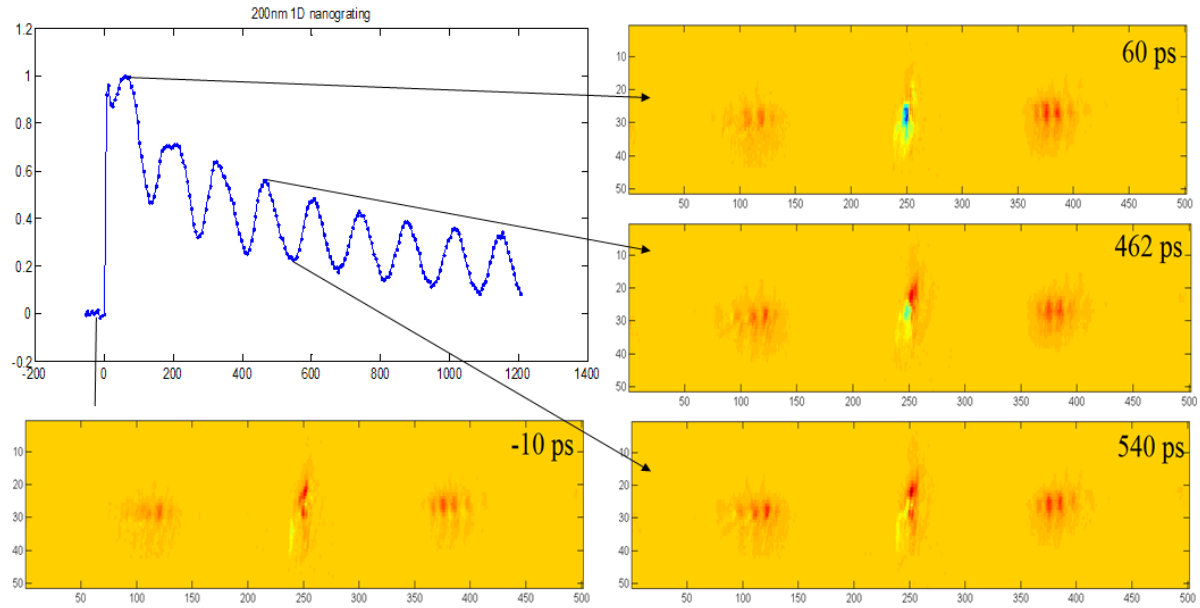

Figure 6.14: Dynamical thermal pattern matching imaging after subtracting pump-off from pump-on, at several different delay times: before zero delay time (-10ps, left bottom) there is only noise, and shortly after zero delay time(60ps, right top) a strong diffraction change shows up. Signal at delay time of 462ps (left middle) and 540ps (left bottom) indicate that we have high enough resolution to resolve the oscillation signal from surface acoustic waves. Imaging data are compared with the 1D scan data (left top).

and find that the ballistic effect is stronger on a 2D nanostructure compared with that on the 1D grating at the same feature size. This is important to be aware of in thermal management and design.

Temperature dependence of the ballistic effect is also scrutinized. By using a cryostat chamber we are able to vary the temperature of the substrate from room temperature to 150K (limited by vacuum level of our chamber), and we observe transition of diffusive thermal transport to ballistic effect on the nickel-on-silicon sample. We also make attempts on dynamic thermal imaging by pattern matching. This is the first step toward our long term goal of dynamical thermal transport imaging at x-ray wavelength for the nanothermal project.

Chapter 7

Conclusions and Future Directions

In summary, I demonstrate that EUV beams generated by high harmonic generation can be a powerful tool to measure ultrafast dynamics in nanoscale systems. In this thesis, I focus on two topics, photoacoustic propagation and thermal transport, both related to phonon dynamics at the nanoscales. Phonons originate from lattice vibrations. Their generation and propagation depends on the atomic interaction, electron-phonon coupling, and phonon-phonon interaction in microscopic view, and relates to the mechanical and thermal property of materials in macroscopic view. This in turn provides a method to explore these interactions as we measure the phonon dynamics. Also it enables us to characterize nano-systems which are difficult to measure with other approaches.

In this thesis, I first work on generating and detecting photoacoustic dynamics, in particular, ultrashort-wavelength surface acoustic waves. SAWs are induced from shear strain and stress, and propagate only in a shallow layer. This feature makes them ideal for the characterization of thin films and interface. We use sub-optical grating patterned structure to generate SAWs whose wavelength is beyond the diffraction limit of pump beams, and EUV beams are used to probe the nanoscale dynamics. This enables us to generate SAWs with wavelength as short as 35nm, corresponding to a 10nm penetration depth. We also show the ability to control the generation of short-wavelength SAWs using two-pulse sequences. By controlling the relative time delay between two pump pulses, we can selectively enhance either the fundamental or second order SAWs. This allowed us to generate even shorter-wavelength SAWs in an existing nano-patterned phononic crystal sample.

Based on these techniques, we have demonstrated a new photoacoustic metrology technique to precisely characterize mechanical properties of very thin films. By generating nanoscale longitudinal and surface acoustic waves simultaneously, we can measure the frequency and velocity of both acoustic waves, and thus derive the Young's modulus and Poisson's ratio. This method can be used even for sub-10nm thin films.

In this approach, nanopatterns are necessary for generating SAWs. However, to take the advantage of non-contact and non-destructive feature of photoacoustic waves, it is important to generate short-wavelength SAWs with no physical contact. Fast development in HHG may make it possible to apply transient grating experiment in EUV or x-ray wavelength in the future. Then the nanoscale photoacoustic measurement would not be restricted to the research labs, but extended to practical applications.

The second part of the thesis focuses on thermal transport in nano-to-bulk systems, which has great importance in the applications of thermal design and thermal management in nanoelectronics. We report the first observation of quasi-ballistic thermal transport on 1D nanopatterned sapphire sample by varying the nanoscale heat source size across the size of phonon mean free path of the sapphire substrate to smaller than it. We have also built a model to connect the thermal transport to thermal expansion and finally to our dynamic EUV diffraction signal. We extend this work in silicon-substrate materials, and verify that the thermal transport does not depend on the polarization of pump beams. We also test thermal transport dynamics on 2D nanostructures. By comparing the thermal decay rate of both 1D and 2D nanostructures with the same size, we observe stronger ballistic effect in 2D samples. Temperature dependence of ballistic transport is also examined. We use a cryostat chamber to continuously control the temperature of sample from room temperature to 150K. No significant result is observed with the nickel-on-sapphire sample, but the nickel-on-silicon sample exhibits clear differences in the thermal transport rate at high and low temperatures. Further simulation work is needed to confirm this result.

A long term goal of the thermal transport project is to extend monitoring dynamical thermal transport to arbitrary samples. One possible approach is to combine pump-and-probe technique

with lensless imaging at EUV wavelength for a dynamic thermal imaging. There are lot of technical challenges before we can observe such 4D dynamics. And we make the first step on this direction by implementing a pattern matching imaging technique, which allows us to observe thermal diffraction images at different pump-and-probe delay times. More efforts are needed to improve the signal-to-noise ratio, and furthermore, to achieve the dynamical imaging goal.

Bibliography

[1] Randy A. Bartels, Ariel Paul, Hans Green, Henry C. Kapteyn, Margaret M. Murnane, Sterling Backus, Ivan P. Christov, Yanwei Liu, David Attwood, and Chris Jacobsen. Generation of spatially coherent light at extreme ultraviolet wavelengths. Science, 297:376, 2002.

[2] Tenio Popmintchev, Ming-Chang Chen, Paul Arpin, Margaret M. Murnane, and Henry Kapteyn. The attosecond nonlinear optics of bright coherent x-ray generation. Nature Photonics, 4:822, 2010.

[3] David Attwood. Soft X-Rays and Extreme Ultraviolet Radiation: Principles and Applications. Cambridge University Press, 2007.

[4] IAEA. Symposium on Inelastic Scattering Neutrons in Solids and Liquids, volume 2, 1963.

[5] Riccardo Tubino, Luigi Piseri, and Giuseppe Zerbi. Lattice dynamics and spectroscopic properties by a valence force potential of diamondlike crystals: C, si, ge, and sn. Journal of Chemical Physics, 56, 1972.

[6] Data source from www.cxro.lbl.gov/.

[7] David G. Cahill, Wayne K. Ford, Kenneth E. Goodson, Gerald D. Mahan, Arun Majumdar, Humphrey J. Maris, Roberto Merlin, and Simon R. Phillpot. Nanoscale thermal transport. Journal of Applied Physics, 93(793), 2003.

[8] Y. S. Ju and K. E. Goodson. Phonon scattering in silicon films with thickness of order 100 nm. Appllied Physics Letter, 74, 1999.

[9] Gang Chen. Thermal conductivity and ballistic-phonon transport in the cross-plane direction of superlattices. Physical Review B, 57, 1998.

[10] Mark Siemens. Nanoscale thermal, acoustic, and magnetic dynamics probed with soft x-ray light. PhD thesis, University of Colorado at Boulder, 2009.

[11] C. W. Chang, D. Okawa, H. Garcia, A. Majumdar, and A. Zettl. Breakdown of fourierś law in nanotube thermal conductors. Physical Review Letters, 101, 2008.

[12] Renkun Chen, Allon I. Hochbaum, Padraig Murphy, Joel Moore, Peidong Yang, and Arun Majumdar. Thermal conductance of thin silicon nanowires. Physical Review Letters, 101, 2008.

[13] M.C. Chen, P. Arpin, T. Popmintchev, M. Gerrity, B. Zhang, M. Seaberg, D. Popmintchev, M.M. Murnane, and H.C. Kapteyn. Bright, coherent, ultrafast soft x-ray harmonics spanning the water window from a tabletop source. Physical Review Letters, 105:173901, 2010.

[14] M. S. Kushwaha, P. Halevi, G. Martinez, L. Dobrzynski, and B. Djafari-Rouhani. Theory of acoustic band structure of periodic elastic composites. Physical Review B, 49, 1994.

[15] Gang Chen. Nonlocal and nonequilibrium heat conduction in the vicinity of nanoparticles. Journal of Heat Transfer, 118, 1996.

[16] P.G. Sverdrup, S. Sinha, Asheghi M., S. Uma, and K.E. Goodson. Measurement of ballistic phonon conduction near hotspots in silicon. Appllied Physical Letter, 78, 2001.

[17] Charles Kittel. Introduction to Solid State Physics. Wiley, 7 edition, 1995.

[18] Neil W. Ashcroft and N. David Mermin. Solid State Physics. Brooks Cole, 1 edition, 1976.

[19] Gang Chen. Nanoscale energy transport and conversion. Oxford University Press, 2005.

[20] P. A. Franken, A. E. Hill, C. W. Peters, and G. Weinreich. Generation of optical harmonics. Physical Review Letter, 7, 1961.

[21] T. Popmintchev. Tunable coherent ultrafast light in the soft and hard X-ray regions of the spectrum. PhD thesis, University of Colorado at Boulder, 2009.

[22] P. B. Corkum. Plasma perspective on strong field multiphoton ionization. Physical Review Letters, 71(13):1994, 1993.

[23] M. Lewenstein, P. Balcou, M. Y. Ivanov, A. LHuillier, and P. B. Corkum. Theory of high-harmonic generation by low-frequency laser fields. Physical Review A, 49:2117–2132, 1994.

[24] C. G. Durfee, A. R. Rundquist, S. Backus, C. Herne, M. M. Murnane, and H. C. Kapteyn. Phase matching of high-order harmonics in hollow waveguides. Physical Review Letter, 83:2187, 1999.

[25] Tenio Popmintchev, Ming-Chang Chen, Oren Cohen, Michael E. Grisham, Jorge J. Rocca, Margaret M. Murnane, and Henry C. Kapteyn. Extended phase matching of high harmonics driven by mid-infrared light. Optics Letter, 33, 2008.

[26] Tenio Popmintchev, Ming-Chang Chen, Alon Bahabad, Michael Gerrity, Pavel Sidorenko, Oren Cohen, Ivan P. Christovc, Margaret M. Murnane, and Henry C. Kapteyn. Phase matching of high harmonic generation in the soft and hard x-ray regions of the spectrum. Proceeding of National Academic Science of USA, 106, 2009.

[27] B. Auld. Acoustic Fields and Waves in Solids, volume I. Wiley, New York, 1973.

[28] Thomas M. Reeder et al. Surface acoustic wave transducer, 02 1974. Patent number: US 3978731.

[29] H. Okano, N. Tanaka, Y. Takahashi, T. Tanaka, K. Shibata, and S. Nakano. Preparation of aluminum nitride thin films by reactive sputtering and their applications to GHz-band surface acoustic wave devices. Applied Physics Letter, 64:166, 1994.

[30] D. Schneider, Th. Witke, Th. Schwarz, B. Schoneich, and B. Schultrich. Testing ultra-thin films by laser acoustics. Surface and Coatings Technology, 126:136, 2000.

[31] J. A. Rogers, L. Dhar, and K. A. Nelson. Noncontact determination of transverse isotropic elastic moduli in polyimide thin films using a laser based ultrasonic method. Appllied Physics Letter, 65:312, 1994.

[32] R. I. Tobey, M. E. Siemens, M. M. Murnane, H. C. Kapteyn, D. H. Torchinsky, and K. A. Nelson. Transient grating measurement of surface acoustic waves in thin metal films with extreme ultraviolet radiation. Appllied Physics Letter, 89:091108, 2006.

[33] B. Bonello, A. Ajinou, V. Richard, P. Djemia, and S. M. Cherif. Surface acoustic waves in the ghz range generated by periodically patterned metallic stripes illuminated by an ultrashort laser pulse. Journal of Acoustic Society of America, 110:1943, 2001.

[34] D. H. Hurley and K. L. Telschow. Picosecond surface acoustic waves using a suboptical wavelength absorption grating. Physical Review B, 66:153301, 2002.

[35] G. A. Antonelli, P. Zannitto, and H. J. Maris. New method for the generation of surface acoustic waves of high frequency. Physica B-Condensed Matter, 316:377, 2002.

[36] M. Siemens, Q. Li, M. Murnane, H. Kapteyn, R. Yang, and E. Anderson K. Nelson. High-frequency surface acoustic wave propagation in nanostructures characterized by coherent extreme ultraviolet beams. Applied Physics Letters, 94:093103, 2009.

[37] D. Hurley and O. Wright. Detection of ultrafast phenomena by use of a modified sagnac interferometer. Opt. Lett., 24:1305, 1999.

[38] Mark E. Siemens, Qing Li, Ronggui Yang, Keith A. Nelson, Erik H. Anderson, Margaret M. Murnane, and Henry C. Kapteyn. Quasi-ballistic thermal transport from nanoscale interfaces observed using ultrafast coherent soft x-ray beams. Nature Materials, 9:26, 2010.

[39] S. Datta and B. J. Hunsinger. First-order reflection coefficient of surface acoustic waves from thin-strip overlays. Journal of Applied Physics, 50:5661, 1979.

[40] O. Hellwig, T. Hauet, T. Thomson, E. Dobisz, J. D. Risner-Jamtgaard, D. Yaney, B. D. Terris, and E. E. Fullerton. Coercivity tuning in co/pd multilayer based bit patterned media. Appllied Physics Letter, 95, 2009.

[41] M. Grobis, E. Dobisz, O. Hellwig, M. Schabes, T. Hauet, G. Zeltzer, , and T. Albrecht. Measurements of the write error rate in bit patterned magnetic recording at 100-320 Gb/in^2. Appllied Physics Letter, 96, 2010.

[42] D. Nardi, F. Banfi, C. Giannetti, B. Revaz, G. Ferrini, and F. Parmigiani. Pseudosurface acoustic waves in hypersonic surface phononic crystals. Physical Review B, 80, 2009.

[43] Damiano Nardi, Marco Travagliati, Mark E. Siemens, Qing Li, Margaret M.Murnane, Henry C. Kapteyn, Gabriele Ferrini, Fulvio Parmigiani, and Francesco Ban. Probing thermomechanics at the nanoscale: Impulsively excited pseudosurface acoustic waves in hypersonic phononic crystals. Nano Letter, 11, 2011.

[44] D. H. Hurley, R. Lewis, O. B. Wright, and O. Matsuda. Coherent control of gigahertz surface acoustic and bulk phonons using ultrafast optical pulses. Applied Physics Letters, 93:113101, 2008.

[45] Thomsen C, Grahn HT, Maris JH, and Tauc J. Picosecond interferometric technique for study of phonons in the brillouin frequency range. Optics Communication, 6(55), 1986.

[46] A. Link, R. Sooryakumar, R. S. Bandhu, and G. A. Antonelli. Brillouin light scattering studies of the mechanical properties of ultrathin low-k dielectric films. Journal of Appllied Physics, 100, 2006.

[47] Holger T. Grahn, Humphrey J. Maris, and Jan Tauc. Picosecond ultrasonics. IEEE Journal of Quantum Electronics, 25(12), 1989.

[48] G. Greaves, A. Greer, R.Lakes, and T. Rouxel. Poisson's ratio and modern materials. Nature Materials, 10(823), 2011.

[49] W. S. Capinski, H. J. Maris, T. Ruf, M. Cardona, K. Ploog, and D. S. Katzer. Thermal-conductivity measurements of gaas/alas superlattices using a picosecond optical pump-and-probe technique. Physical Review B, 59, 1999.

[50] E. Pop, S. Sinha, and K. E. Goodson. Heat generation and transport in nanometer-scale transistors. Proc. IEEE, 94, 2006.

[51] Jungchul Lee, T. Beechem, T. L. Wright, B. A. Nelson, S. Graham, and W. P. King. Electrical, thermal, and mechanical characterization of silicon microcantilever heaters. Journal of Microelectromechanical System, 15, 2006.

[52] Kimberly Hamad-Schifferli, John J. Schwartz, Aaron T. Santos, Shuguang Zhang, and Joseph M. Jacobson. Remote electronic control of dna hybridization through inductive coupling to an attached metal nanocrystal antenna. Nature, 415, 2002.

[53] A. J. Minnich, J. A. Johnson, A. J. Schmidt, K. Esfarjani, M. S. Dresselhaus, K. A. Nelson, , and G. Chen. Thermal conductivity spectroscopy technique to measure phonon mean free paths. Physical Review Letters, 107, 2011.

[54] Richard L. Sandberg, Ariel Paul, Daisy A. Raymondson, Steffen Hadrich, David M. Gaudiosi, Jim Holtsnider, Ra'anan I. Tobey, Oren Cohen, Margaret M. Murnane, and Henry C. Kaptey. Lensless diffractive imaging using tabletop coherent high-harmonic soft-x-ray beams. Physical Review Letters, 99, 2007.

[55] J. Miao, D. Sayre, and H. N. Chapman. Phase retrieval from the magnitude of the fourier transforms of nonperiodic objects. Journal of the Optical Society of America A, 15, 1998.

[56] R. I. Tobey, M. E. Siemens, O. Cohen, M. M. Murnane, H. C. Kapteyn, and K. A. Nelson. Ultrafast extreme ultraviolet holography: dynamic monitoring of surface deformation. Opt. Lett., 32:286, 2007.

[57] C. Giannetti, B. Revaz, F. Banfi, M. Montagnese, G. Ferrini, F. Cilento, S. Maccalli, P. Vavassori, G. Oliviero, E. Bontempi, L. E. Depero, V. Metlushko, and F. Parmigiani. Thermomechanical behavior of surface acoustic waves in ordered arrays of nanodisks studied by near-infrared pump-probe diffraction experiments. Physical Review B, 76:125413, 2007.

[58] David G. Cahill, Wayne K. Ford, Kenneth E. Goodson, Gerald D. Mahan, Arun Majumdar, Humphrey J. Maris, Roberto Merlin, and Simon R. Phillpot. Nanoscale thermal transport. Journal of Applied Physics, 93(793), 2003.

[59] Thomsen C, Grahn HT, Maris JH, and Tauc J. Nanoscale thermal transport. Physical Review B, 34(4129), 1986.

[60] P. Hess. Laser diagnostics of mechanical and elastic properties of silicon and carbon films. Applied Surface Science, 106(429), 1996.

[61] G. Andrew Antonelli, Bernard Perrin, Brian C. Daly, and David G. Cahill. Characterization of mechanical and thermal properties using ultrafast optical metrology. MRS Bulletin, 2006.

[62] Gheorghe Stan, Sean W. King, and Robert F. Cook. Elastic modulus of low-k dielectric thin films measured by load-dependent contact-resonance atomic force microscopy. Journal of Material Research, 24, 2009.

[63] K. Nelson, R. Miller, D. Lutz, and M. Fayer. Optical generation of tunable ultrasonic waves. Journal of Applied Physics, 53, 1982.

[64] J. Robillard, A. Devos, and I. Roch-Jcune. Time-resolved vibrations of two-dimensional hypersonic phononic crystals. Physical Review B, 76, 2007.